

Human skin detection using correlation rules on dynamic color clustering

Rodrigo Augusto Dias Faria

THESIS SUBMITTED
TO THE
INSTITUTE OF MATHEMATICS AND STATISTICS
OF THE
UNIVERSITY OF SÃO PAULO
TO
OBTAIN THE TITLE
OF
MASTER IN SCIENCE

Program: Computer Science

Advisor: Prof. Dr. Roberto Hirata Jr

São Paulo, July 2018

Human skin detection using correlation rules on dynamic color clustering

This is the original version of the thesis prepared by the
candidate Rodrigo Augusto Dias Faria, such as
submitted to the Examining Committee.

To my beloved wife and daughter.

Acknowledgements

I would like to express my sincere gratitude to my advisor, Prof. Dr. Roberto Hirata Jr, who has believed in my potential since the beginning of my research. His motivation, patience, and enthusiasm in teaching me were essential during the accomplishment of all this work. More than that, this work would not have been done without his flexibility in admitting me as a part-time student to continue to work in the industry. We all know how difficult it is to reconcile these activities, but his comprehension is something that will be marked forever in my life. Thank you so much!

No matter how tired, discouraged, hopeless she was, but my wife Tamires gave me unconditional support. She accompanied me at absolutely every moment. She is the most incredible woman I have ever met. And, to my happiness, she gave me the greatest gift of my life: my daughter Júlia. I love you unconditionally.

I would also like to thank all my family, for the example they have always given me, for their care and dedication. In particular, I thank my mother for showing me the importance of education in my entire life. I have no doubt that your choices have always been thought the best for me and my siblings.

I can not forget two great friends I made during these years, among others who were part of this journey, Ana Lucia, and Luiz Medina, for having spent so much time together and for providing discussions of the highest level, of the most varied subjects. They were also able to teach me the beauty of the proof by induction. I will always remember those days!

I should also remember the Professors who were members of my Examining Committee, Prof. Dr. Roberto Marcondes Cesar Junior, and Prof. Dr. Peter Sussner, for kindly giving up their limited time to grant me valuable suggestions and corrections that have brought me to this result. In particular, to Prof. Dr. Roberto Marcondes for having indicated to me the reading of the paper that served as the basis for all this project.

I also thank the University of São Paulo for giving me the opportunity and for providing structure and excellence in teaching for the entire community. I may say many thanks also to everyone in the university who support us including, but not limited to, Professors, secretaries, co-workers, and colleagues.

And, last but not least, I would like to be grateful to Inatel and Qualcomm, the companies I have worked for during the years of the realization of this work. They were extremely supportive of me in all the difficult moments I faced during the course of this project.

You were all key players in this achievement!

Resumo

FARIA, R. A. D. **Detecção de pele humana usando regras de correlação baseadas em agrupamento dinâmico de cores.** Dissertação (Mestrado) - Instituto de Matemática e Estatística, Universidade de São Paulo, São Paulo, 2018.

A pele humana é constituída de uma série de camadas distintas, cada uma das quais reflete uma porção de luz incidente, depois de absorver uma certa quantidade dela pelos pigmentos que se encontram na camada. Os principais pigmentos responsáveis pela origem da cor da pele são a melanina e a hemoglobina. Há evidências de que a pigmentação da pele humana é uma adaptação para regular a penetração da radiação ultravioleta (UV) na epiderme. Como as populações se mudaram para partes do mundo com diferentes níveis de radiação UV, elas sofreram mudanças genéticas que alteraram a pigmentação da pele. Assim, tons mais escuros de pele estão, em geral, próximos à linha do Equador e dos trópicos. Todos esses fatos nos dão uma ideia de quão complexo pode ser um sistema para detectar pele humana em imagens. A detecção de pele desempenha um papel importante em uma ampla gama de aplicações em processamento de imagens e visão computacional. Em suma, existem três abordagens principais para detecção de pele: baseadas em regras, aprendizado de máquina e híbridos. Elas diferem em termos de precisão e eficiência computacional. Geralmente, as abordagens com aprendizado de máquina e as híbridas superam os métodos baseados em regras, mas exigem um conjunto de dados de treinamento grande e representativo, bem como um tempo de classificação custoso, que pode ser um fator decisivo para aplicações em tempo real. Neste trabalho, propomos uma melhoria, em três versões distintas, de um novo método de detecção de pele baseado em regras que funciona no espaço de cores YCbCr. Nossa motivação baseia-se na hipótese de que: (1) a regra original pode ser revertida e, (2) pixels de pele humana não aparecem isolados, ou seja, as operações de vizinhança são levadas em consideração. O método é uma combinação de algumas regras de correlação baseadas nessas hipóteses. Essas regras avaliam as combinações de valores de crominância Cb, Cr para identificar os pixels de pele, dependendo da forma e tamanho dos agrupamentos de cores de pele gerados dinamicamente. O método é muito eficiente em termos de esforço computacional, bem como robusto em cenas de imagens muito complexas.

Palavras-chave: detecção de pele, segmentação de pele humana, modelo de cores YCbCr, regras de correlação, agrupamento dinâmico de cores.

Abstract

FARIA, R. A. D. **Human skin detection using correlation rules on dynamic color clustering.** Thesis (Masters Degree) - Institute of Mathematics and Statistics, University of São Paulo, São Paulo, 2018.

Human skin is made of a stack of different layers, each of which reflects a portion of impinging light, after absorbing a certain amount of it by the pigments which lie in the layer. The main pigments responsible for skin color origins are melanin and hemoglobin. There is evidence that human skin pigmentation is an adaption to regulate the penetration of Ultra Violet (UV) radiation into the epidermis. As populations moved to parts of the world with different UV radiation levels, they underwent genetic changes that modified their skin pigmentation. So, darker shades of skin are, in general, near the Equator and tropics. All of these facts give us an idea of how complex can be a system to automatically detect human skin in images. Skin detection plays an important role in a wide range of image processing and computer vision applications. In short, there are three major approaches for skin detection: rule-based, machine learning and hybrid. They differ in terms of accuracy and computational efficiency. Generally, machine learning and hybrid approaches outperform the rule-based methods but require a large and representative training dataset as well as costly classification time, which can be a deal breaker for real-time applications. In this work, we propose an improvement, in three distinct versions, of a novel method for rule-based skin detection that works in the YCbCr color space. Our motivation is based on the hypothesis that: (1) the original rule can be reversed and, (2) human skin pixels do not appear isolated, i.e. neighborhood operations are taken into consideration. The method is a combination of some correlation rules based on these hypotheses. Such rules evaluate the combinations of chrominance Cb, Cr values to identify the skin pixels depending on the shape and size of dynamically generated skin color clusters. The method is very efficient in terms of computational effort as well as robust in very complex image scenes.

Keywords: skin detection, human skin segmentation, YCbCr color model, correlation rules, dynamic color clustering.

Contents

List of Acronyms	xi
List of Symbols	xiii
List of Figures	xvii
List of Tables	xix
1 Introduction	1
1.1 Motivation	4
1.2 Objectives	4
1.3 Contributions	5
1.4 Organization	5
2 Related Work	7
3 Theoretical Background	13
3.1 Digital image	13
3.2 Basic relationship between pixels	14
3.2.1 Neighborhood	14
3.2.2 Connectivity	15
3.2.3 Arithmetic and logic operations	15
3.2.4 Image boundaries	16
3.3 Image histogram	17
3.4 Image segmentation	18
3.4.1 Thresholding	19
3.5 Color models	20
3.5.1 Munsell color model	21
3.5.2 CIE color model	21
3.5.3 RGB color model	24
3.5.4 CMY color model	25
3.5.5 Color models of the YUV family	26
3.5.6 Color models of the HSI family	26

4 Correlation rules and proposed extension	31
4.1 Correlation rules on YCrYCb colormap	31
4.2 Extended method	34
4.3 Neighborhood extended method	35
4.4 Supplementary neighborhood operations	36
4.5 Parameters tuning via a grid search strategy	39
5 Evaluation	41
5.1 Datasets	41
5.1.1 UCI	41
5.1.2 SFA	42
5.1.3 Pratheepan	44
5.1.4 HGR	45
5.1.5 Compaq	46
5.2 Evaluation measures	47
5.3 Rule-based experiments	48
5.4 Supplementary neighborhood operations experiments	54
5.5 Grid search parameters experiments	55
6 Conclusions	67
6.1 Final considerations	67
6.2 Future work	68
A Trapezoids Parameters Tuning Results	69
Bibliography	85

List of Acronyms

AR	Aleix and Robert Face Database
CIE	Commission Internationale de l'Eclairage
CMY	Cyan, Magenta and Yellow
FERET	Face Recognition Technology database
GIS	Geographic Information System
HGR	Hand Gesture Recognition database
HSI	Hue, Saturation, Intensity
HSL	Hue, Saturation, Lightness
HSV	Hue, Saturation, Value
ID3	Iterative Dichotomiser 3
IHLS	Improved, Hue, Luminance and Saturation
LUT	Look-UP Table
NTSC	National Television System Committee
PAL	Phase Alternating Line
RBF	Radial Basis Function
RGB	Red, Green and Blue
SECAM	Sequential Color with Memory
SFA	Skin of FERET and AR Database
UCS	Uniform Chromaticity Scale
UCI	University of California in Irvine skin/non skin dataset
UV	Ultra Violet
VISAPP	International Joint Conference on Computer Vision, Imaging and Computer Graphics Theory and Applications
YIQ	Luma, Hue and Saturation
YUV	Luma and Chrominance

List of Symbols

$f(x, y)$	Intensity function of an image
W	Number of horizontal samples (lines) of an image
H	Number of vertical samples (columns) of an image
L	Number of gray-levels
L_{min}	The minimum gray-level of a range
L_{max}	The maximum gray-level of a range
L_n	The n -th vector channel of a pixel
L_i	The i -th vector value of a channel of a pixel
$N_4(p)$	Four neighbors of a pixel p
$N_D(p)$	Diagonal neighbors of a pixel p
$N_8(p)$	Eight neighbors of a pixel p
AND	AND logic operator
OR	OR logic operator
XOR	XOR logic operator
NOT	NOT logic operator
T	Threshold value in image histogram split
T_n	Multi-threshold values in image histogram split
L^*	Luminance
a^*	Green/red axis on $L^*a^*b^*$ color model
b^*	Blue/yellow axis on $L^*a^*b^*$ color model
u^*	Green/red axis on $L^*u^*v^*$ color model
v^*	Blue/yellow axis on $L^*u^*v^*$ color model
θ	Hue angle on HSI color model
\max	Max operator
\min	Min operator
argmax	Arguments of maxima operator
\mathbb{R}	Set of real numbers
P	A point (pixel) in an image
P_Y	Y component of a pixel P in $YCbCr$ model
Y_{Cb}	Subspace of Cb points in function of Y
Y_{Cr}	Subspace of Cr points in function of Y

T_{YC_b}	Trapezoid of the Y_{C_b} subspace
T_{YC_r}	Trapezoid of the Y_{C_r} subspace
$A_{T_{YC_b}}$	Area of Y_{C_b} trapezoid
$A_{T_{YC_r}}$	Area of Y_{C_r} trapezoid
Y_{min}	Minimum value of Y luminance distribution
Y_{max}	Maximum value of Y luminance distribution
Y_0	Top-left coordinate of T_{YC_r} trapezoid
Y_1	Top-right coordinate of T_{YC_r} trapezoid
Y_2	Top-right coordinate of T_{YC_b} trapezoid
Y_3	Top-right coordinate of T_{YC_b} trapezoid
Y_{min}	Minimum value of Y component
Y_{max}	Maximum value of Y component
Cr_{min}	Minimum Cr value used to compute T_{YC_r} trapezoid
Cr_{max}	Maximum Cr value used to compute T_{YC_r} trapezoid
Cb_{min}	Minimum Cb value used to compute T_{YC_b} trapezoid
Cb_{max}	Maximum Cb value used to compute T_{YC_b} trapezoid
h_{Cr}	Height of T_{YC_r} trapezoid
h_{Cb}	Height of T_{YC_b} trapezoid
$H_{Cr}(P_Y)$	Height of other T_{YC_r} coordinates
$H_{Cb}(P_Y)$	Height of other T_{YC_b} coordinates
$\Delta_{Cr}(P_Y)$	Distance between $(P_Y, H_{Cr}(P_Y))$ and the base of T_{YC_r}
$\Delta_{Cb}(P_Y)$	Distance between $(P_Y, H_{Cb}(P_Y))$ and the base of T_{YC_b}
$\Delta'_{Cr}(P_Y)$	Normalized distance with respect to the difference in size of the T_{YC_r} trapezoid
$\Delta'_{Cb}(P_Y)$	Normalized distance with respect to the difference in size of the T_{YC_b} trapezoid
α	Rate between $\Delta'_{Cr}(P_Y)$ and $\Delta'_{Cb}(P_Y)$ normalized distances
s_f	Rate between the longer and shorter upper side of T_{YC_r} and T_{YC_b}
P_{Cr}	Cr component of a pixel P
P_{Cb}	Cb component of a pixel P
P_{Cr_s}	Estimated value of P_{Cr} point
P_{Cb_s}	Estimated value of P_{Cb} point
dP_{Cr_s}	Estimated distance value of P_{Cr} point
dP_{Cb_s}	Estimated distance value of P_{Cb} point
dP_{Cr}	Distance between P_{Cr} point and Cr_{min}
dP_{Cb}	Distance between P_{Cb} point and Cb_{max}
I_P	Minimum difference between P_{Cr} and P_{Cb} with respect to P_{Cb_s}
J_P	Maximum distance between the points (P_Y, P_{Cb}) and (P_Y, P_{Cb_s})
I'_P	Minimum difference between P_{Cr} and P_{Cb} with respect to P_{Cr_s}
J'_P	Maximum distance between the points (P_Y, P_{Cr}) and (P_Y, P_{Cr_s})

- P_{min} Minimum percentile of the histogram of Y luminance component used to compute trapezoid coordinates
- P_{max} Maximum percentile of the histogram of Y luminance component used to compute trapezoid coordinates

List of Figures

1.1	The layers of human skin	1
1.2	Map of skin color reflectance	2
3.1	Representation of the raster order of an image	14
3.2	The <i>4-neighbors</i> representation of a pixel p	14
3.3	The <i>8-neighbors</i> representation of a pixel p	15
3.4	Representation of a <i>4-neighbors</i> window mask going beyond image borders .	17
3.5	Grayscale image with its respective histogram	18
3.6	Gray level histograms that can be partitioned by (a) a single threshold, and (b) multiple thresholds	19
3.7	Munsell color model.	21
3.8	CIE 1931 chromaticity diagram	23
3.9	Unit cube representing the colors of the RGB model	24
3.10	CMY subtractive color model	25
3.11	Graphical representation of the HSI model	27
4.1	Graphical representation of the trapezoids as well as its parameters	31
4.2	Computation of Cr_{max} based on Cr values histogram of a 724×526 image .	32
4.3	Neighbors evaluation with respect to a pixel P	35
4.4	Flowchart of our proposed neighbors' method	36
4.5	Image samples with the diagonal effect after the neighbors method segmentation	38
5.1	3-dimensional view of the RGB channels of the UCI dataset	42
5.2	Structure of the windows that form the SFA patch samples	43
5.3	Examples of SFA face image database	44
5.4	Examples of Pratheepon skin dataset	45
5.5	Examples of HGR skin dataset	46
5.6	Examples of Compaq skin/non-skin dataset	47
5.7	Image samples with the results of each method in SFA dataset	51
5.8	Image samples with the results of each method in Pratheepon dataset	52
5.9	Image samples with the results of each method in HGR dataset	52
5.10	Image samples with the results of each method in Compaq dataset	53

5.11 The output template table with result metrics of the grid search algorithm	56
5.12 Scatter plot with the quality measures for grid search parameters in Compaq dataset.	59
5.12 Scatter plot with the quality measures for grid search parameters in Compaq dataset (cont.).	60
5.13 Scatter plot with the quality measures for grid search parameters in Pratheepan dataset.	61
5.13 Scatter plot with the quality measures for grid search parameters in Pratheepan dataset (cont.).	62
5.14 Scatter plot with the quality measures for grid search parameters in HGR dataset.	63
5.14 Scatter plot with the quality measures for grid search parameters in HGR dataset (cont.).	64
5.15 Scatter plot with the quality measures for grid search parameters in SFA dataset.	65
5.15 Scatter plot with the quality measures for grid search parameters in SFA dataset (cont.).	66

List of Tables

3.1	Definition of addition, subtraction, multiplication and division arithmetic operations in two f_1 and f_2 images	16
3.2	Definition of AND, OR, XOR and NOT logic operations in two f_1 and f_2 images	17
5.1	Excerpt with samples from the UCI dataset	42
5.2	Confusion matrix table used during experiments	48
5.3	Quantitative result metrics of the proposed enhancements and original method	49
5.4	Specificity of the proposed enhancements and original method for non-skin images of Compaq dataset	50
5.5	Quantitative result metrics of the proposed supplementary neighborhood adaptation	54
5.6	Quantitative result metrics of the proposed grid search parameters tuning . .	57
A.1	Trapezoids parameters tuning results for Compaq dataset and combined rules	69
A.2	Trapezoids parameters tuning results for Pratheepan dataset and combined rules	73
A.3	Trapezoids parameters tuning results for HGR dataset and combined rules . .	76
A.4	Trapezoids parameters tuning results for SFA dataset and combined rules . .	80

Chapter 1

Introduction

The study and understanding of human skin color date from many years ago. Being some of the contributors of this field, [Edwards and Duntley \(1939\)](#) were one of those who tried to precisely analyze the color formation of this particular material. According to them ([Edwards and Duntley, 1939](#)), skin is made of a stack of different layers (see Fig. 1.1), each of which reflects a portion of impinging light, after absorbing a certain amount of it by the pigments which lie in the layer. The light which is neither reflected nor absorbed, however, is transmitted through each successive layer to the underlying one, where absorption, reflection, and transmission again take place. The absorption bands of the pigment in each layer are thus "imprinted" on both the reflected and transmitted light from each layer. The total reflected light, consequently, has the absorption characteristics of the pigments in all the layers. This phenomenon gives rise to what we call skin color.

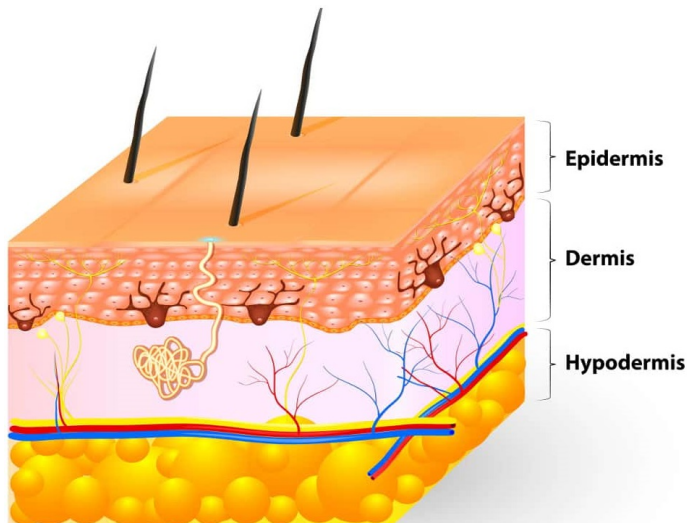


Figure 1.1: The layers of human skin. Source: [Wajnberg \(2018\)](#).

[Edwards and Duntley \(1939\)](#) observed yet that other pigments out of melanin and hemoglobin also play a role in the origin of skin color, along with an additional optical effect, designated as scattering. The pigments are melanoid – derivative of melanin –, oxyhemoglobin, and carotene. Furthermore, they stated that variations in the amount of melanin in the epidermis are responsible for the difference in human skin coloration.

Later, [Anderson and Parrish \(1981\)](#) provided an integrated review of the transfer of optical radiation into human skin. They ([Anderson and Parrish, 1981](#)) noticed that the absorption of Ultra Violet (UV) radiation as well as, to a lesser degree, optical scattering build an optical barrier in the epidermis.

In fact, there is evidence that human skin pigmentation is an adaption for the regulation of penetration of UV radiation into the epidermis. Skin pigmentation of populations has been changed genetically as they moved to parts of the world with different UV radiation levels, a necessary fine-tuning that made it possible for them to tan easily (Jablonski and Chaplin, 2000). Tanning is the ability to develop temporary melanin pigmentation in the skin in response to UV radiation and has evolved numerous times in people living under highly seasonal patterns of sunshine (Jablonski and Chaplin, 2010).

Therefore, a natural evolution of the skin coloration has been occurred to accommodate the physiological needs of humans as they have dispersed to regions of widely varying annual average UV radiation (Jablonski and Chaplin, 2010). On the basis of this observation, Chaplin (2004) built a model for the correlation between the skin reflectance and the seasonal UV radiation levels along with other environmental variables. Based on this model, they (Chaplin, 2004) could be able to determine the contribution of each variable to skin reflectance. Chaplin (2004) combined the data of environmental variables with the UV radiation data recorded by satellite and data on human skin reflectance in a Geographic Information System (GIS). A predicted map of skin color reflectance was produced as a result of the visual and statistical analysis of this system (see Fig. 1.2).

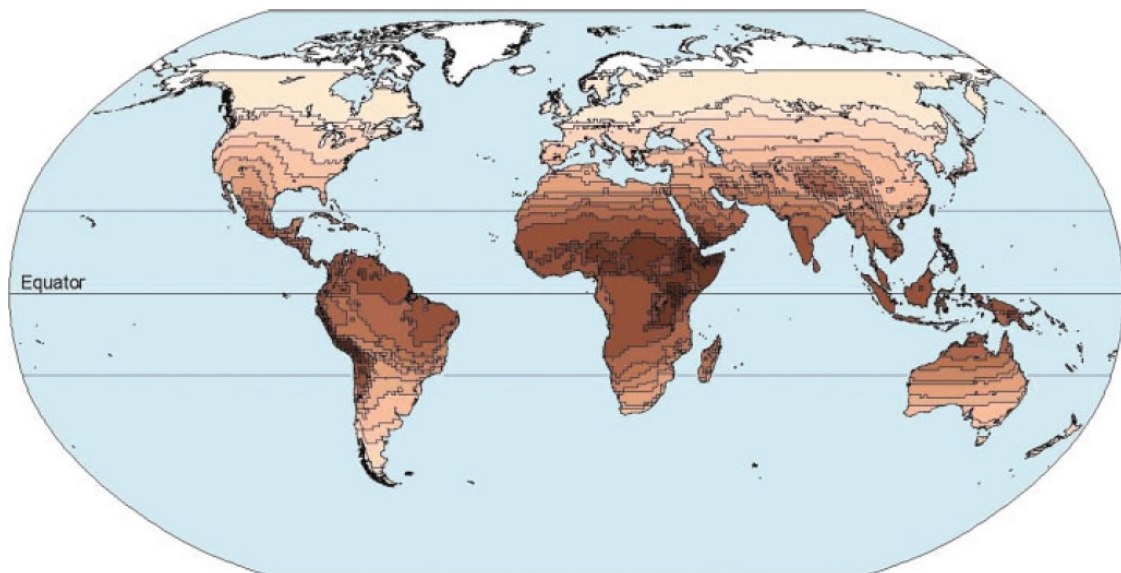


Figure 1.2: Map of skin color reflectance. The map is generalized to reduce the number of polygons. Source: Chaplin (2004).

We can clearly see darker shades of skin near the Equator and tropics due to exposition to high UV radiation. This is a very singular feature of human skin, once it acts as a sun shield to protect the body from solar UV radiation (Jablonski, 2004). The great number of shades of skin shown on the map gives us an idea of how complex can be a system to automatically detect human skin in images, based on color only.

Skin detection can be defined as the process of identifying skin-colored pixels in an image. It plays an important role in a wide range of image processing and computer vision applications such as face detection, pornographic image filtering, gesture analysis, face tracking, video surveillance systems, medical image analysis, and other human-related image processing applications (Kakumanu *et al.*, 2007).

The problem is complex because of the numerous similar materials with human skin tone and texture, and also because of illumination conditions, ethnicity, the large number of shades, sensor capturing singularities, geometric variations, etc. Because it is a primary

task in image processing, additional requirements such as real-time processing, robustness, and accuracy are also desirable.

It is worth mentioning that image processing is one of the most important tasks in a computer vision system. Its goal is to create a suitable description – typically based on shapes, textures, gray levels or color – with enough information to differentiate the objects in the scene. With this description, useful interpretation can be extracted from the image by means of an automatic computer system that facilitates human perception.

There is no general agreement among authors regarding where image processing stops and computer vision starts. The first, as the title says, processes the image by applying some transformations on it which will produce a more enhanced and readable image. In addition, the input and output of the process are always images. On the other hand, computer vision has the ultimate goal to use computers to emulate human vision, including learning and the ability to make inferences and take actions based on visual inputs. In other words, computer vision is intended to, based on images, obtain more abstract representations (Gonzalez and Woods, 2002). In general, computer vision systems benefit from image processing techniques as pre-processing steps to build better applications. Thus, we can see that they definitely are not different fields, but there is an overlapping between them.

This work is intended to explore new methods on human skin detection. We will use techniques from both image processing and computer vision fields. Color space transformation from image processing, for example, as well as human skin segmentation and understanding as part of computer vision. This is a tentative to imitate the human visual system and its capability to recognize others from the same species – of course, humans use other characteristics to identify other humans like shape, height, gender, and others, but the skin is also part of this recognition system.

One of the powerful features used in this task is definitely skin color, which is a strong attribute and it is used in most algorithms for skin detection. It is normally used along with other features such as shape, texture, and geometry, or even as a preliminary step to classify regions of interest in an image.

The human skin color pixels have a restricted range of hues and are not deeply saturated since the appearance of skin is formed by a combination of blood (red) and melanin (brown, yellow), which leads the human skin color to be clustered within a small area in the color space (Fleck *et al.*, 1996).

Color has the ability of functioning as a descriptor that often simplifies the identification and extraction of an object in a scene. Moreover, the ability of humans to discern thousands of tonalities and intensities compared to only a few dozen levels of gray put the color as a strong candidate feature in computer vision and image processing applications (Gonzalez and Woods, 2002).

In general, the colors are represented by their brightness, hue, and saturation, which are usually the features used to distinguish one color from another (Gonzalez and Woods, 2002).

The brightness gives the notion of chromatic intensity. Hue represents the dominant color perceived by an observer. Saturation refers to the relative purity or amount of white light applied to the hue. Combined, hue and saturation are known as chromaticity and, therefore, a color must be characterized by its brightness and chromaticity (Gonzalez and Woods, 2002).

Colors can be specified by mathematical models in tuples of numbers in a coordinate system and a subspace within that system where each color is represented by a single point. Such models are known as the color models (or color spaces) (Gonzalez and Woods, 2002).

The choice of a color space is also a key point of a feature-based method when using skin color as a detection cue. Due to sensitivity to illumination in the scene, the input image is, in general, first transformed into a color space whose luminance and chrominance components

can be separate to mitigate the problem (Vezhnevets *et al.*, 2003).

For the case of skin detection methods, there are, basically, three approaches: rule-based, machine learning based and hybrid. They differ in terms of classification accuracy and computational efficiency. Machine learning and hybrid methods require a training set, from which the decision rules are learned. Such approaches outperform the rule-based methods but require a large and representative training dataset as well as it takes a long classification time, which can be a deal breaker for real-time applications (Kakumamu *et al.*, 2007).

In this work, we propose an improvement of a novel method for rule-based skin detection that works in the YCbCr color space (Brancati *et al.*, 2017). Our motivation is based on the hypothesis that the original rule can be complemented by another rule that is a reversal interpretation of the one proposed originally. Besides that, we also take into consideration that a skin pixel does not appear isolated, so we propose another variation based on neighborhood operations. The set of rules evaluate the combinations of chrominance Cb, Cr values to identify the skin pixels depending on the shape and size of dynamically generated skin color clusters (Brancati *et al.*, 2017). The method is very efficient in terms of computational effort as well as robust in very complex image scenes.

1.1 Motivation

The subject of the research has been something that was attractive for us from the very beginning of the program. First, with a project on race classification in partnership with the industry. Then, with the intensification in the search for related works, with the problem of skin detection.

The latter led us to the brilliant work of Brancati *et al.* (2017): a new rule-based skin detection method that works in the YCbCr color space. Here, more specifically, our motivation was to propose improvements based on the hypothesis that: (1) the original rule can be reversed and, (2) human skin pixels do not appear isolated, i.e. neighborhood operations are taken in consideration.

1.2 Objectives

Skin detection is a very complex problem due to the numerous similar materials with human skin tone and texture, and also because of illumination conditions, ethnicity, sensor capturing singularities, geometric variations, etc. Because it is a primary task in image processing, additional requirements such as real-time processing, robustness, and accuracy are also desirable.

Although many advances have been observed in the literature, from what we have seen until the development of this research, it is possible to say that it is not yet a completely solved problem. Basically, there are three approaches for skin detection: rule-based, machine learning based and hybrid. They differ in terms of classification accuracy and computational efficiency. In general, rule-based methods do not require a training step and they can be very competitive in terms of computational cost.

Therefore, the main objective of this research is to create or improve new methods for skin detection, according to the rule-based approach. More specifically, our main objective is to achieve improvements in the method proposed by Brancati *et al.* (2017) in order to reduce the false positive rate. In addition, we have another secondary objective that is to publish articles with the results in renowned conference or journals in the area.

1.3 Contributions

In this work, we have done a comprehensive and detailed study of various methods of skin detection within those based on rules. On the basis of Brancati *et al.* (2017), seen by us as the state of the art in this field, we created variations that brought significant improvements. In addition, we analyzed the methods in turn in order to provide the researchers, practitioners, enthusiasts, and other readers with a detailed understanding of the nuances involved in those methods, such as parameter selection and optimization, through a series of quantitative experiments, as well as qualitative analysis based on our observations.

Thus, we can enumerate some of the contributions that came as a result of this research project:

1. Implementation of three variations of the skin detection method proposed by Brancati *et al.* (2017) on the basis of the inversely proportional behavior of the chrominance components (Cb and Cr) of the YCbCr color model. Furthermore, extensive quantitative and qualitative experiments performed in a wide range of image datasets well-known in this field;
2. Adapted version of the neighborhood method (8-neighbors window) presented in Section 4.3;
3. A grid search implementation to try different combinations of trapezoids parameters in order to optimize them (if possible) and understand those who have been used so far.

Part of our contributions was published earlier in 2018 in the *Proceedings of the 13th International Joint Conference on Computer Vision, Imaging and Computer Graphics Theory and Applications - VISAPP* (Faria and Jr., 2018).

1.4 Organization

In this chapter, we have presented the background of this work as well as the motivation, main contributions, and objectives behind it. Chapter 2 presents other relevant research works that also addresses the problem of skin detection in several distinct approaches. In Chapter 3 we provide an overview of the theoretical concepts that apply to this research. Next, in Chapter 4, we present a state of the art skin detection method recently developed by Brancati *et al.* (2017). We review the method and extend it adding more rules to enforce the constraints and seeking for a better accuracy in terms of false positive rate without hurting the performance of the original method. Then, in Chapter 5, we present the evaluation of the proposed extensions along with the original method in four widely known datasets: SFA, Pratheepan, HGR, and Compaq. In addition, a brief definition of the evaluation metrics used is shown for the sake of clarity. Finally, Chapter 6 winds up this thesis by discussing our observations along the research, focused on the experimental results, and directs the readers towards future works.

Chapter 2

Related Work

There are a large number of works of skin detection based on color information and there are a couple of them comparing different techniques and classifiers, mainly from the point of view of performance, color models, skin color modeling and different datasets (Kakumanu *et al.*, 2007; Mahmoodi and Sayedi, 2016; Vezhnevets *et al.*, 2003).

On different techniques, statistical models are those which estimate the probability that an observed pixel is associated with skin, based on a estimation dataset. One approach is the single histogram based Look-UP Table (LUT) that is capable to obtain the distribution of skin pixels in a particular color space, by using a set of training pixels (Mahmoodi and Sayedi, 2016). Considering the Red, Green, Blue (RGB) color model for instance, a histogram with 256 bins per channel - 256³ in total - can be constructed for further counting the probability (see Eq. 2) of each possible RGB value (Jones and Rehg, 2002).

$$P(rgb) = \frac{\#counts\ of\ rgb}{total\ counts}$$

In Jones and Rehg (2002), the authors applied this technique to figure out the decision boundary of skin pixels distribution by using a 3-dimensional histogram model constructed from approximately 2 billion pixels. Those pixels were collected from 18,696 images over the Internet to perform skin detection. First, visualization techniques were used to examine the shape of these distributions. Then, by examining the 3D histogram from several angles, Jones and Rehg (2002) realized that its overall shape could be inferred.

So, two different histograms for skin and non-skin in the RGB color space were calculated. Using those histograms along with training data, a surprisingly accurate pixel-wise classifier was derived. The best performance at an error rate of 88% was reached for histograms of size 32 (Jones and Rehg, 2002).

On the basis of the output of the skin detector, Jones and Rehg (2002) also trained a classifier to determine whether a naked person is present or not in the scene. The features used from the output to create the feature vector were (Jones and Rehg, 2002):

- Percentage of pixels detected as skin
- Average probability of the skin pixels
- Size in pixels of the largest connected component of skin
- Number of connected components of skin
- Percent of colors with no entries in the skin and nonskin histograms

- Height of the image
- Width of the image

In the last step, 10,679 images were manually classified in 5,453 naked and 5,226 non-naked image sets to train a neural network classifier. The neural network outputs a number between 0 and 1, with 1 indicating a naked person in the image. The detection rate achieved was of 88%, with a false alarm rate of 11.3% ([Jones and Rehg, 2002](#)).

Skin detection is sometimes used as a primary task for other applications. [Hsu et al. \(2002\)](#) have embedded skin segmentation with the purpose to build a face detector application. The algorithm first performs a lighting compensation on the R, G, and B components of the pixels of the image. Then, these color corrected components are transformed into YCbCr space. [Hsu et al. \(2002\)](#) observed that a skin tone cluster is formed in the YCb and YCr subspaces. Based on the premise that skin tone color is independent of the luminance component, they ([Hsu et al., 2002](#)) non-linearly transformed the YCbCr to turn the skin cluster luma-independent. Then, in this transformed YCbCr space, the skin pixels are detected using an elliptical skin model.

The experiments have shown good skin detection results, around 96% and 80% detection rate respectively on HH1 MPEG7 video and on Champion datasets, which contain images with frontal, near-frontal, half-profile and profile faces under varying illumination conditions and backgrounds. On the other hand, the results also showed a high false positive rate, that is reduced further with facial feature detection procedure based on the spatial arrangement of the detected skin patches ([Hsu et al., 2002](#)).

Another typical method is to define explicitly, through a number of rules, the boundaries that delimit the grouping of skin pixels in some color space ([Vezhnevets et al., 2003](#)). This approach has been adopted by [Kovac et al. \(2003\)](#) in the RGB color space, resulting in a true positive rate of 90.66%. Basically, to find out the skin cluster in the RGB color space, the skin color is determined with the following rules ([Kovac et al., 2003](#)):

Skin color at uniform daylight illumination

$$\begin{aligned} R &> 95, G > 40, B > 20 \\ \max(R, G, B) - \min(R, G, B) &> 15 \\ |R - G| &> 15 \\ R &> G \\ R &> B \end{aligned}$$

Skin color at light daylight illumination

$$\begin{aligned} R &> 220, G > 210, B > 170 \\ |R - G| &\leq 15 \\ R &> B \\ G &> B \end{aligned}$$

They ([Kovac et al., 2003](#)) also performed experiments in comparison with [Hsu et al. \(2002\)](#), where only the chromaticity channels Cb and Cr from the YCbCr color space are used. The results showed that the performance of the classifier is inferior in relation to the

approach using all the three channels. Hsu *et al.* (2002) method indeed diminished the influence of noise in dark images, but in images that are captured under standard daylight illumination, they label too many pixels as skin, decreasing the performance of the face detector by increasing the number of false positive pixels (Kovac *et al.*, 2003).

Chai and Ngan (1999) proposed a similar method in YCbCr color space, where a skin color map was designed using a histogram approach based on a given set of training images. Chai and Ngan (1999) observed that the Cb and Cr distributions of skin color fall in the ranges [77, 127] and [133, 173], respectively, regardless the skin color variation in different races.

However, after an exhaustive image histogram analysis, Basilio *et al.* (2011) found that the thresholds given by Chai and Ngan (1999) was robust only against images with Caucasian people. Once their (Basilio *et al.*, 2011) purpose was to find human skin from different people races, from any place of the world, a new threshold for each chromaticity (Cb, Cr) channel has been set up, regardless of skin color:

$$\begin{aligned} 80 \leq Cb \leq 120 \\ 133 \leq Cr \leq 173 \end{aligned}$$

The key advantage of this method is the simplicity of skin detection rules that lead to the construction of a very fast classifier. On the other hand, achieving high recognition rates with this method is difficult because it is necessary to find a good color space and empirically appropriate decision rules (Vezhnevets *et al.*, 2003).

Differently from Kovac *et al.* (2003), the authors of Yogarajah *et al.* (2011) developed a technique where the thresholds defined in the rules are dynamically adapted. The method consists of detecting the region of the eye and extracting an elliptical region to delimit the corresponding face. A Sobel filter is applied to detect the edges of the resulting region which is subjected to a dilation in order to get the optimal non-smooth regions, (i.e. eyes and mouth). The resulting image is subtracted from the elliptical image. As a result, there is a more uniform skin region where the thresholds are calculated.

Every single pixel in the colored image is classified as skin and non-skin, based on the calculated dynamic threshold values. When the algorithm detects multiple possible face regions in the image, a dynamic threshold is constructed for each of them and, subsequently, submitted to perform skin segmentation on the whole image. Finally, a logical OR operation is applied in all of the segmented regions obtained as of each dynamic threshold (Yogarajah *et al.*, 2011).

The technique was used as part of a preprocessing step in Tan *et al.* (2012) in a strategy combining a 2-dimensional density histogram and a Gaussian model for skin color detection. First, human eyes are located and, then, an elliptical mask model is used to generate the elliptical face region in the image. Due to computational simplicity, a Sobel filter is employed to remove non-smooth (i.e., eyes, eyebrows, mouth, etc.) regions. Then, the detected edge pixels are further submitted to a dilation operation to get the optimal non-smooth regions. Finally, a new image, that only consists of face regions, is obtained.

It is worth mentioning that the dynamic threshold with smoothed 2-D histogram is based on the assumption that the face and body of a person always share the same colors (Tan *et al.*, 2012).

Thereafter, a 2-D histogram with smoothed densities and a Gaussian model are used as features to represent the skin and non-skin distributions, respectively. They (Tan *et al.*, 2012) also applied a fusion technique that uses the product rule on the two features to obtain

better skin detection results.

Experiments were carried out using three public databases: Pratheepan, ETHZ PASCAL, and Stottinger. A comparison between different color spaces as well as proposed fusion and non-fusion approaches were also established. Quantitative results are only available for Stottinger dataset with $F - measure = 0.6490$, $Precision = 0.6403$ and $Recall = 0.6580$ measures (Tan *et al.*, 2012).

Naji *et al.* (2012) built an explicit classifier in the HSV color space for 4 different skin ethnic groups in parallel (standard skin, shadow/blackish skin, light skin and red concentrated skin and lips). Basically, the classifier applies a rule-based region growth algorithm, after primitive segmentation, in which the output of the first layer is used as a seed, and then, the final mask in subsequent layers is constructed iteratively by neighboring skin pixels. The problem of shadow regions has been also addressed by lightening them with a skin color correction approach. A number of 125 images were collected from two different datasets for experiments. The rate of true positive pixels reported was of 96.5% with a very low false positive rate of 0.76%.

The model proposed by Kawulok *et al.* (2013) is based on global and local image information from where a probability map is built and, next, used to generate the initial seed for spatial analysis of skin pixels. The spatial analysis result is improved once these seeds, extracted from a local model, are highly adapted to the image.

In their (Kawulok *et al.*, 2013) proposal, first, human faces are captured in the input image through a multi-level ellipse detector, from where a local skin color model is learned. The local model is used to perform skin detection in the input image. Next, the local skin probability map is used to apply a high-probability threshold and obtain the seeds. Finally, based on the seeds gathered on the previous step, the spatial analysis is carried out in the global probability map, created on the basis of the global skin color model.

In general, color can be considered one of the most decisive tools that affect the performance of skin detection algorithms, even though some of them do not use the color as a feature directly (Mahmoodi and Sayedi, 2016). Therefore, the choice of a color space is directly related to the outcome produced by a particular approach (Mahmoodi and Sayedi, 2016). However, Albiol *et al.* (2001) proved that the optimum performance of the skin classifiers is independent of the color space chosen.

RGB is the most commonly used color space for storing and representing digital images since the cameras are enabled to provide the images in such model as well as displays to show them. However, RGB suffers a high influence of the environment illumination. In order to reduce this influence, the RGB channels can be normalized and the third component can be removed since it does not provide significant information (Kakumanu *et al.*, 2007).

This particular characteristic led Bergasa *et al.* (2000) to build an adaptive and unsupervised Gaussian model to segment skin in the normalized RGB color space, using only the r and g channels (the normalized R and G channels), after the evaluation of other color spaces for the same application.

In Jayaram *et al.* (2004), a comparative study using a Gaussian and a histogram approaches in a dataset of 805 color images in 9 different color spaces has been performed. The results revealed that the absence of the luminance component, that means, using only two channels of the color space, significantly impacts the performance. The best results were obtained in the SCT, HSI, and CIELab color spaces with histogram approach.

In Chaves-González *et al.* (2010), the authors compared, under the same circumstances, the performance of 10 color spaces based on the k -means clustering algorithm on 15 images of the Aleix and Robert (AR) face image database (Martínez and Benavente, 1998). The ground truth images have been carefully generated by the authors. This means that parts of

the photo which do not include skin color, such as hair, beard, lips, eyes, and background, were completely removed.

Experiments have been executed with k -means clustering method over the test set images for each of the 10 different color spaces. For each color space, Chaves-González *et al.* (2010) have done several tests with each channel lonely, using two channels – with all possible combinations –, and with the three channels.

The tests have been carried out comparing, in a detailed quantitative manner, each color space with an accurate and objective criterion. In other words, the output image produced by the k -means was compared, in a pixel-wise fashion, to the ground truth images to get the quantitative measures. According to the results obtained, using two channels combined did not produce a good outcome. On the other hand, the results with each channel isolated were surprisingly good in comparison to the three channels fused. Lastly, among all the color spaces used for the skin detection experiments, the most appropriate were, in this order, HSV, YCgCr, and YDbDr (Chaves-González *et al.*, 2010).

A similar study on color spaces and different skin color modeling have been provided in Khan *et al.* (2012). A total of six color spaces (IHLS, HSI, RGB, normalized RGB, YCbCr and CIELab) and nine skin color modeling approaches (AdaBoost, Bayesian network, J48, Multilayer Perceptron, Naive Bayesian, Random Forest, RBF network, SVM and Histogram based) were evaluated on 8991 manually pixel-wise annotated images by means of F-measure. Khan *et al.* (2012) concluded that color space transformation, as well as the removal of the luminance channel, degrades the performance. In addition, classification results can be improved with the usage of lighting correction algorithms.

In Kaur and Kranthi (2012), an algorithm similar to that proposed by Kovac *et al.* (2003) have been implemented, where the boundaries that delimit the grouping of skin pixels are defined by explicit rules. After segmenting the image with the explicit rules, the algorithm also performs morphological and filtering operations to improve the accuracy of the method. The authors applied the algorithm in the YCbCr and CIELab color spaces, ignoring the Y and L luminance components, respectively. The results were more satisfactory when the algorithm was applied on CIELab. A similar technique was implemented in Shaik *et al.* (2015) and Kumar and Malhotra (2015) in the HSV and YCbCr color spaces, the latter providing the best results in both.

Finally, Brancati *et al.* (2017) proposed a novel rule-based skin detection method that works in the YCbCr color space. Basically, to classify skin pixels in the image, the algorithm evaluates the combinations of chrominance (Cb, Cr) components by way of correlation rules. These correlation rules are calculated relying upon the shape and size of dynamically generated skin color clusters. Geometrically, the clusters create trapezoidal polygons in the YCb and YCr subspaces whose apparent arrangement reflects an inversely proportional behavior observed in relation to chrominance components. They (Brancati *et al.*, 2017) compared the results, in terms of quantitative performance metrics, with six other well known rule-based methods in the literature, outperforming them in almost all of them.

Chapter 3

Theoretical Background

In this chapter, the theoretical concepts that apply to this research are stated. First, we define and explain the concept of a digital image in Section 3.1 as well as basic relationship between pixels in Section 3.2. In Section 3.3 we will see how image histograms are fundamental for the methods described in chapter 4 of the proposed solution. Also, the background of image segmentation, mainly for the thresholding technique is shown in Section 3.4. Thereafter, a brief introduction to color models is provided in Section 3.5 in order to give an overview of the main characteristics of some of the most used in the computer vision and image processing area, on which this research is based.

3.1 Digital image

By definition, an image is a two-dimensional function $f(x, y)$, where x and y are spatial coordinates, and the amplitude of f at any pair of coordinates (x, y) is called the *intensity* or *gray level* of the image at that point. The image is said digital when the function $f(x, y)$ is converted to a discrete form. This is made by a process called *digitalization*, which consists of two steps: *sampling* and *quantization* (Gonzalez and Woods, 2002).

Each element of the discrete function $f(x, y)$ is called *pixel* (picture element), where $0 \leq x \leq W - 1$ and $0 \leq y \leq H - 1$. This means that the image can be represented in a matrix form (see Eq. 3.1), where W is the number of lines and H the number of columns of the matrix. Therefore, W and H defines the size or resolution of the image (Pedrini and Schwartz, 2008).

$$f(x, y) = \begin{bmatrix} f(0, 0) & f(0, 1) & \cdots & f(0, H - 1) \\ f(1, 0) & f(1, 1) & \cdots & f(1, H - 1) \\ \vdots & \vdots & \ddots & \vdots \\ f(W - 1, 0) & f(W - 1, 1) & \cdots & f(W - 1, H - 1) \end{bmatrix}$$

Usually, pixels are stored, and therefore read, in this matrix in an order known as *raster* (see Fig. 3.1). This information is important so that capture and display devices may be able to establish a common interface, and make necessary transformations in the coordinates, when needed.

In a monochromatic digital image, the value of a pixel is a scalar in the range $[L_{min}, L_{max}]$, where L is the (integer) number of gray levels (Pedrini and Schwartz, 2008).

In a multispectral image, each pixel has a vector value such that $f(x, y) = (L_1, L_2, \dots, L_n)$ where $L_{min} \leq L_i \leq L_{max}$ and $i = 1, 2, 3, \dots, n$. In general, L_i can represent different measures for each of (x, y) coordinate as well as different intervals (Pedrini and Schwartz, 2008).

A colored image is a multispectral image, where the color in each (x, y) point is given by

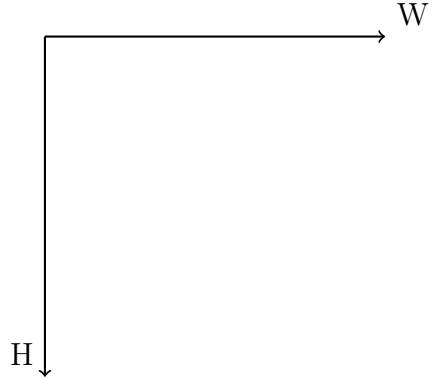


Figure 3.1: Representation of the raster order of an image. The origin coordinates $(0, 0)$ starts in the top left corner, where both axes rise. Source: proposed by the author.

three variables: brightness, hue and saturation (Pedrini and Schwartz, 2008). The brightness gives the notion of chromatic intensity. Hue represents the dominant color perceived by an observer. Saturation refers to the relative purity or amount of white light applied to the hue. Combined, hue and saturation are known as chromaticity and, therefore, a color must be characterized by its brightness and chromaticity (Gonzalez and Woods, 2002).

3.2 Basic relationship between pixels

There is a number of applications in image processing and computer vision that uses information of relationship among pixels to create knowledge. Some of these important relationships will be described in the following sections once we will apply it in chapter 4 further. It is worth mentioning that we defined an image as a function $f(x, y)$. In this section, when referring to a particular pixel, we will denote it in lowercase letters such as p .

3.2.1 Neighborhood

A pixel p with coordinates (x, y) can have up to four¹ horizontal and vertical neighbors whose coordinates are given by:

$$(x + 1, y), (x - 1, y), (x, y + 1), (x, y - 1)$$

This set of pixels, called the *4-neighbors* of p , is denoted by $N_4(p)$ (Gonzalez and Woods, 2002). See Figure 3.2 for a reference on how this neighborhood looks like.

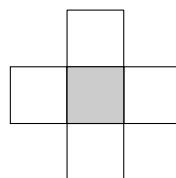


Figure 3.2: The 4-neighbors representation of a pixel p . The pixel p is centered on the grid with gray background. Source: adapted from Pedrini and Schwartz (2008).

Each pixel of the image is a unite distance from (x, y) . Some neighbors of p might lie outside of the image boundaries if (x, y) is on the border of the image (Gonzalez and Woods,

¹Respecting the image domain limits.

2002). Those who will use neighborhood operations in the image might take this in consideration to avoid index out of range in those regions.

The four coordinates of the diagonals of p , if they exist in the domain of the image, are given by:

$$(x + 1, y + 1), (x + 1, y - 1), (x - 1, y + 1), (x - 1, y - 1)$$

This set of pixels are denoted by $N_D(p)$. When combined, the *4-neighbors* and $N_D(p)$ will generate the *8-neighbors* of p , known as $N_8(p)$ (Gonzalez and Woods, 2002). Formally, we have:

$$N_8(p) = N_4(p) \cup N_D(p)$$

See Figure 3.3 for a reference on how the $N_8(p)$ neighborhood looks like.

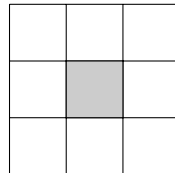


Figure 3.3: The 8-neighbors representation of a pixel p . The pixel p is centered on the grid with gray background. Source: adapted from Pedrini and Schwartz (2008).

Despite these are the most common neighbors used in applications, other different distances from p as well as connectivity can be applied. The idea of neighborhood can also be extended to 3-dimensional images where, instead of pixels, the voxels are the coordinates considered.

3.2.2 Connectivity

The connectivity between pixels is a very important concept used to establish the boundaries of objects and regions in an image. To figure out if two pixels are connected, it must be determined if they are neighbors and if their gray levels satisfy some similarity criteria, such as gray levels, color or texture equality. For instance, in a binary image, where the pixels values vary in the range $[0, 1]$, two pixels may be *4-neighbors*, but they are connected if and only if they have the same value (Gonzalez and Woods, 2002).

3.2.3 Arithmetic and logic operations

Image arithmetic applies one of the standard arithmetic operations or a logical operator to two or more images. The operators are applied in a pixel-wise manner. In other words, the value of a pixel in the output image depends only on the values of the corresponding pixels in the input images. Hence, the images – or the subsets, if it is the case – must be of the same size. Although image arithmetic is the most simple form of image processing, they are used extensively in a wide range of applications and its use can potentially produce very interesting practical results. A main advantage of arithmetic operators is that the process is very simple and, therefore, fast (Gonzalez and Woods, 2002).

The most common arithmetic operations between two pixels, say $f_1(x, y)$ and $f_2(x, y)$ of two different images f_1 and f_2 , are the addition, subtraction, multiplication and division as shown in Table 3.1 (Pedrini and Schwartz, 2008).

Addition is used often for image averaging to reduce noise. Subtraction is used frequently for static background removal. Multiplication as well as division is applied to correct gray level shading (Gonzalez and Woods, 2002).

Once the arithmetic operations can potentially produce images with values out of the gray levels given in the original images, additional effort is frequently needed to work around this situation. For instance, when adding two images, some pixels of the resulting image may be greater than 255. Similarly, when subtracting two images, some pixels may be with negative values. One way to solve this issue is, after the arithmetic operation, perform a transformation in the gray levels of the resulting image to keep them within a suitable range (Pedrini and Schwartz, 2008).

Logic operations are also useful in computer vision and image processing applications. They are applied only in binary images, while arithmetic operations can be used with higher gray levels. The terminology adopted among authors and application developers is that pixels with zero value (black color) belongs to the objects while one value (white color) corresponds to the background. Table 3.2 shows how the logic operations can be computed (Pedrini and Schwartz, 2008).

The AND operation outputs 1 in the resulting image when both pixels, at same coordinates in the input images, are equal 1. XOR operation outputs 1 when only one of the pixels – but not both – has value 1; 0 otherwise. The result of OR operation is 1 when at least one of the pixels has 1 value. The NOT operation reverse the value of the pixel in the image (Pedrini and Schwartz, 2008).

All the logic operators can be combined to create other more complex and robust operators. They can be used to combine information between images or to extract information of regions of interest from them (Pedrini and Schwartz, 2008).

In addition to the pixel-wise processing, logic and arithmetic operations can be used for neighborhood processing. Typically, this kind of processing uses masks, where terms such as windows and filters are often used as synonym of masks. The idea of the masks is to turn the value of the pixel a function of its own value and its neighbors. It is note mentioning that masks application are made under high computational cost. Therefore, they must be used carefully (Pedrini and Schwartz, 2008).

3.2.4 Image boundaries

When working with neighborhood operations, the mask being used, independently of its size, can fall beyond the image boundaries. In other words, this means that, for an image f , with size $W \times H$, some parts of the mask operator will be outside of the domain of the image (i.e. out of the range given by $W \times H$ matrix) (Pedrini and Schwartz, 2008). Figure 3.4 shows an example of this phenomenon in a 10×8 image being used as input for an 4-neighbors operator.

There are several ways to work around this problem. One simple mechanism is to simply

Name	Operation
Addition	$f_1(x, y) + f_2(x, y)$
Subtraction	$f_1(x, y) - f_2(x, y)$
Multiplication	$f_1(x, y) * f_2(x, y)$
Division	$f_1(x, y) / f_2(x, y)$

Table 3.1: Definition of addition, subtraction, multiplication and division arithmetic operations in two f_1 and f_2 images. Source: adapted from Pedrini and Schwartz (2008).

Name	Operation
AND	$f_1(x, y) \text{ AND } f_2(x, y)$
OR	$f_1(x, y) \text{ OR } f_2(x, y)$
XOR	$f_1(x, y) \text{ XOR } f_2(x, y)$
NOT	$\text{NOT}(f_1(x, y))$

Table 3.2: Definition of AND, OR, XOR and NOT logic operations in two f_1 and f_2 images. Source: adapted from Pedrini and Schwartz (2008).

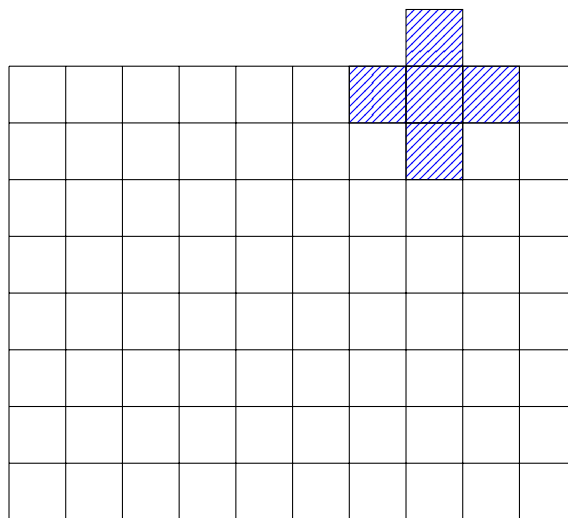


Figure 3.4: Representation of a 4-neighbors window mask going beyond image borders Pedrini and Schwartz (2008).

ignore the pixels on the border where the mask go beyond. Despite this will avoid index out of bound errors, border pixels of the image will not be looked at. Another approach is to copy the corresponding pixels from the input image. Once again, the resulting image will have some not processed pixels in the border. Another strategy is to apply a different mask for the borders, which may consider the difference in the corners as well, to perform the operation, which can turn the operation more complex and computational costly (Pedrini and Schwartz, 2008).

3.3 Image histogram

In particular for image processing, when we are referring to an image histogram, we are talking about to count the frequency of the pixels for each intensity levels in separate bins, in a multi-valued (intensity levels) sequence (Fisher *et al.*, 2003). The most common visual representation is a graph or plot, which gives an overall idea about the intensity distribution of an image. The foundation of a histogram can be seen as a set of bins, where each bin is representing a certain intensity value from a given range. A simple algorithm to compute a histogram of an image may examines all pixels in the image and assigns each to a bin depending on the pixel intensity. In the end, each bin will have the number of pixels of its own intensity value (Gonzalez and Woods, 2002).

For instance, in an 8-bit grayscale image there are 256 different possible intensities,

and so, the histogram will graphically display 256 integer numbers showing the counting of occurrences of those grayscale values. It is also possible to compute histograms of color images. In this particular case, the channels of the color space in turn are split individually from where a separate histogram is calculated (Fisher *et al.*, 2003).

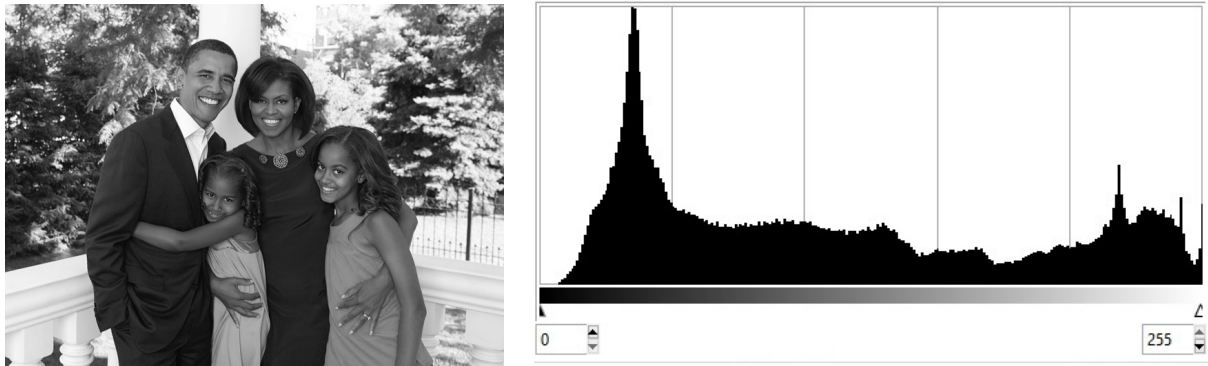


Figure 3.5: Grayscale image with its respective histogram. Left image is a sample from Pratheepan dataset, transformed to grayscale. On the right we have its histogram of pixel intensity values in the range [0, 255]. Source: Tan *et al.* (2012) and the author.

A histogram can be seen as a probability distribution, once the number of pixels for a given intensity level gives an estimate of the probability of occurrence of this intensity level (Gonzalez and Woods, 2002). Several statistical measures can be obtained from a histogram such that minimum and maximum values, mean, median, standard deviation, and percentiles (Pedrini and Schwartz, 2008). Those measures as well as the histogram itself are fundamental for the methods described in chapter 4 of the proposed solution.

3.4 Image segmentation

Image segmentation is the task of partitioning the image domain so each part is semantically different from each of its neighbors. These regions who, in general, are the representation of specific objects, are the fundamental parts of an image. This partitioning process is also used by humans, through their visual perception, into surrounding environment to help themselves to recognize them, guide their movements, and for almost every other day by day tasks in their lives (Plataniotis and Venetsanopoulos, 2000).

Segmentation of complex images is one of the most difficult tasks in the field of image processing, where the accuracy determines whether a successful operation or not (Gonzalez and Woods, 2002). It is a heavy process that consists of many steps such as the analysis of color, shape, motion, geometry, and texture of objects in images. It is worth mentioning that all of these steps are taken effortlessly by our visual system. However, it is definitely not easy to create algorithms whose performance is comparable to that of the human visual system (Plataniotis and Venetsanopoulos, 2000).

Usually, the first task of any image analysis process is image segmentation. All subsequent tasks, such as feature extraction and object recognition rely heavily on the quality of the segmentation (Plataniotis and Venetsanopoulos, 2000). The algorithms created for image segmentation generally are based on one of two basic properties of intensity values: *discontinuity*, where abrupt changes in intensity, such as points, lines, and edges are detected, and *similarity*, whose approaches are based on regions partitioning, according to a set of predefined criteria (Gonzalez and Woods, 2002).

One of the *similarity* methods it is the thresholding: a popular and simple method used to segment regions of an image, especially in applications where speed is an important factor – that is the case for skin detection, once it is used, in general, for face detection, gesture analysis, face tracking, video surveillance systems, medical image analysis, and other human-related image processing applications. Due to the simplicity of implementation, several authors apply this technique for skin detection task (Basilio *et al.*, 2011; Chai and Ngan, 1999; Kaur and Kranthi, 2012; Kovac *et al.*, 2003; Kumar and Malhotra, 2015; Shaik *et al.*, 2015). Others extend this application by using adaptive thresholding (Tan *et al.*, 2012; Yogarajah *et al.*, 2011).

3.4.1 Thresholding

Histogram thresholding is one of the simplest pixel-based techniques for image segmentation due to its intuitive properties and uncomplicated implementation (Gonzalez and Woods, 2002). Roughly speaking, if an image is composed of distinct regions – that means, each region in the histogram are represented by a peak, similar to a Gaussian distribution –, adjacent regions could be split into separated groups, once adjacent peaks are likely separated by a valley (Plataniotis and Venetsanopoulos, 2000). Those valleys can be determined by means of one or more threshold values. However, to find out the threshold value that is the lower bound of a valley is definitely not a trivial task (Plataniotis and Venetsanopoulos, 2000).

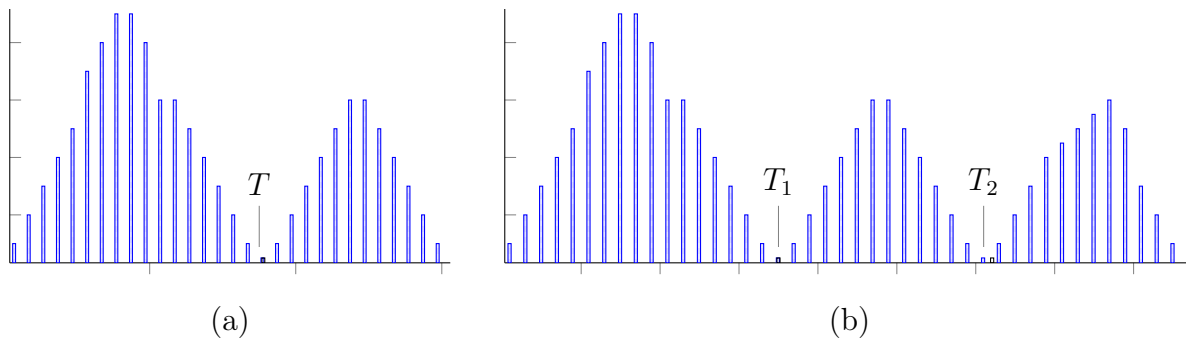


Figure 3.6: Gray level histograms that can be partitioned by (a) a single threshold, and (b) multiple thresholds. Source: adapted from (Gonzalez and Woods, 2002).

Let Figure 3.6(a) the gray levels histogram of an image $f(x, y)$. We can clearly see two dominant groups of pixels. One obvious way to separate the objects in this image is to select a threshold T that splits these groups. In other words, for every single point (x, y) , if $f(x, y) \leq T$, then (x, y) belongs to the first object (or group), otherwise it belongs to the second object. In general, one of these objects is seen as the background of the image and the other, the portion of interest in the image (Gonzalez and Woods, 2002).

The resulting image $g(x, y)$ after applying the thresholding is given by (Gonzalez and Woods, 2002):

$$g(x, y) = \begin{cases} 0, & \text{if } f(x, y) \leq T \\ 1, & \text{otherwise} \end{cases} \quad (3.1)$$

Therefore, pixels labeled 0 corresponds to the object left of T in the histogram, and pixels labeled 1 corresponds to the object right of T in histogram – or background as commonly used in literature. The *single-level thresholding* procedure that produces $g(x, y)$ image is known as *binarization* (Gonzalez and Woods, 2002).

Figure 3.6(b) shows a slightly more general case of thresholding, where three distinct groups of the histogram are split by T_1 and T_2 threshold values. Here, *multi-level thresholding* classifies a point (x, y) as belonging to a specific object class as follows (Gonzalez and Woods, 2002):

$$g(x, y) = \begin{cases} l_1, & \text{if } f(x, y) \leq T_1 \\ l_2, & \text{if } T_1 < f(x, y) \leq T_2 \\ l_3, & \text{if } f(x, y) > T_2 \end{cases} \quad (3.2)$$

where l_1, l_2, l_3 are different gray levels used to represent each interval given by the thresholding values.

When T depends only on $f(x, y)$, that is, only on gray level values, the threshold is called *global*. When another property – e.g. the average gray level of a neighborhood centered on (x, y) – is used to define T , the threshold is called *local*. If, in addition, T depends on spatial coordinates x and y , the threshold is called *dynamic* or *adaptive* (Gonzalez and Woods, 2002).

3.5 Color models

The use of color images in computer vision or image processing can be motivated by two main factors. The first refers to the powerful characteristic of color to function as a descriptor that often simplifies the identification and extraction of an object in a scene. The second is related to the ability of humans to discern thousands of tonalities and intensities compared to only a few dozen levels of gray (Gonzalez and Woods, 2002).

The visual perception of color by the human eye should not vary according to the spectral distribution of the natural light incident upon an object. In other words, the color appearance of objects remains stable under different lighting conditions. This phenomenon is known as color constancy (Gevers *et al.*, 2012).

As an example, the grass of a soccer stadium remains green throughout the day, even at dusk when, from a physical point of view, sunlight has a more reddish appearance.

The human perception of colors occurs by the activation of nerve cells that send signals to the brain about brightness, hue, and saturation, which are usually the features used to distinguish one color from another (Gonzalez and Woods, 2002).

The brightness gives the notion of chromatic intensity. Hue represents the dominant color perceived by an observer. Saturation refers to the relative purity or amount of white light applied to the hue. Combined, hue and saturation are known as chromaticity and, therefore, a color must be characterized by its brightness and chromaticity (Gonzalez and Woods, 2002).

Colors can be specified by mathematical models in tuples of numbers in a coordinate system and a subspace within that system where each color is represented by a single point. Such models are known as the color models (Gonzalez and Woods, 2002).

These models can be classified as of two types: the additive models in which the primary color intensities are added to produce other colors and subtractive, where colors are generated by subtracting the length of the dominant wave from the white light.

The following sections briefly describe some of the major color models, as well as their variants and main areas of application.

3.5.1 Munsell color model

Pioneer in an attempt to organize the perception of color in a color space, Albert H. Munsell was able to combine the art and science of colors in a single theory (Plataniotis and Venetsanopoulos, 2000).

The principle of equality of visual spacing between the components of the model is the essential idea of the Munsell color model. These components are hue, value, corresponding to luminance, and chroma, corresponding to saturation (Plataniotis and Venetsanopoulos, 2000).

The model is represented by a cylindrical shape and it can be seen in the Figure 3.7. The hue is arranged in the circular axis consisting of five bases as well as five secondary colors, the saturation in the radial axis and the luminance in the vertical axis in a range varying from 0 to 10.

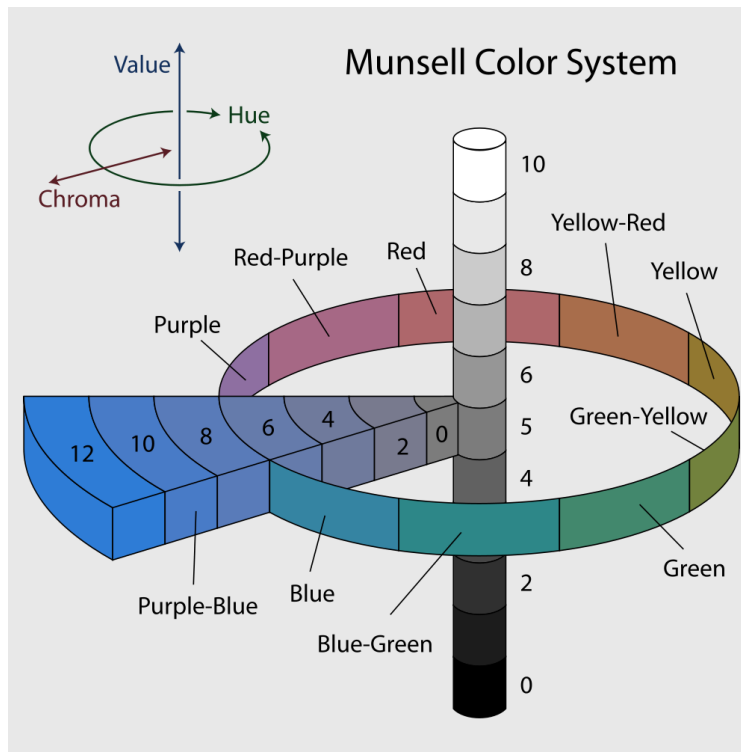


Figure 3.7: Munsell color model represented by a cylindrical shape. The hue is arranged on the circular axis consisting of five bases and five secondary colors, the saturation on the radial axis and the luminance on the vertical axis in a range varying from 0 to 10. Source: Rus (2007).

3.5.2 CIE color model

In 1931, the CIE established the first mathematical model of a color numerical specification, whose objective was to analyze the relationship between the physical aspects of colors in the electromagnetic spectrum and their perception by the human visual system to determine how an ordinary person perceives the color. A review of this specification was published in 1964 (Gonzalez and Woods, 2002).

The experiment that originated the standard consisted of detecting the colors perceived by an observer from a mixture of three primary colors X, Y and Z, called tristimulus values. These coordinates gave rise to the CIE XYZ color space which encompasses all the colors

that can be perceived by an ordinary human being. For this reason, it is considered a device independent representation (Plataniotis and Venetsanopoulos, 2000).

The system proposed by the CIE XYZ to describe a color is based on a luminance component Y, and two additional components X and Z, that bring the chromaticity information. This system is formed by imaginary colors that can be expressed as combinations of the normalized measures shown in Equations 3.3, 3.4 and 3.5 (Plataniotis and Venetsanopoulos, 2000).

$$x = \frac{X}{X + Y + Z} \quad (3.3)$$

$$y = \frac{Y}{X + Y + Z} \quad (3.4)$$

$$z = \frac{Z}{X + Y + Z} \quad (3.5)$$

where $x + y + z = 1$.

Combinations of negative values and other problems related to selecting a set of real primaries are eliminated. The chromaticity coordinates x and y allow to represent all colors in a two-dimensional plane, also known as a chromaticity diagram, which can be seen in the Figure 3.8.

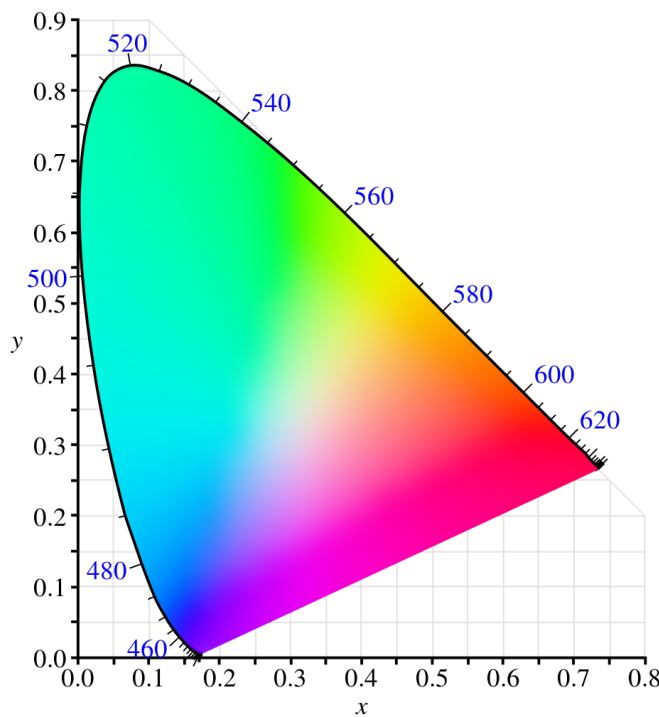


Figure 3.8: CIE 1931 chromaticity diagram. The points representing pure colors in the electromagnetic spectrum are labeled according to their wavelengths and are located along the curve from the right end of the x -axis, corresponding to the red color, to the left end of the same axis, corresponding to the violet color, forming a polygon similar to a horseshoe. The internal points correspond to all possible combinations of visible colors. Source: Ben (2009).

The coordinates ($x = 1/3, y = 1/3$) correspond to the location of the white light, also known as white point, and serve as a reference in the process of image capture, coding, or reproduction.

CIE also derived and standardized two other color models based on CIE XYZ specification and, likewise, are device independent. Both are perceptually uniform, which means that equal perceptual distances separate all colors in the system (Vezhnevets *et al.*, 2003). As an example, the gray scale of the space should allow for a smooth transition between black and white.

The first one was designed to reduce the problem of perceptual non-uniformity. Some Uniform Chromaticity Scale (UCS) diagrams were proposed based on mathematical equa-

tions to transform the values XYZ or the coordinates x, y into a new set of values (u, v) , which gave rise to the 1960 CIE uv chromaticity diagram (Gevers *et al.*, 2012).

With unsatisfactory results yet, the CIE made a new change by multiplying the v component by a factor of 1.5. In addition, the brightness scale given by the Y component has been replaced by $L^* = [0, 100]$ to better represent the differences in luminosity that are equivalent. This revision originated the CIE 1976 $L^*u^*v^*$ color model, commonly known by the acronym CIELuv (Gevers *et al.*, 2012).

In 1976 the CIE adopted a new color model, based on the L, a, b model, proposed by Richard Hunter in 1948, which best represented the uniform spacing of colors. Named CIE $L^*a^*b^*$ and known by the acronym CIELab, it is a space based on opponent colors² in which the color stimuli of retina is converted to distinctions between light and dark, red and green, and blue and yellow, represented by the axes L^* , a^* , and b^* , respectively (Gevers *et al.*, 2012).

3.5.3 RGB color model

The RGB model, an acronym for Red, Green, and Blue, is an additive color model in which the three primary colors red, green and blue are added to produce the others (Gonzalez and Woods, 2002).

This system was based on the trichromatic theory of Thomas Young and Hermann Helmholtz in the mid-19th century and can be represented graphically through the unit cube defined on the axes R, G, and B, as illustrated in the Figure 3.9 (Plataniotis and Venetsanopoulos, 2000).

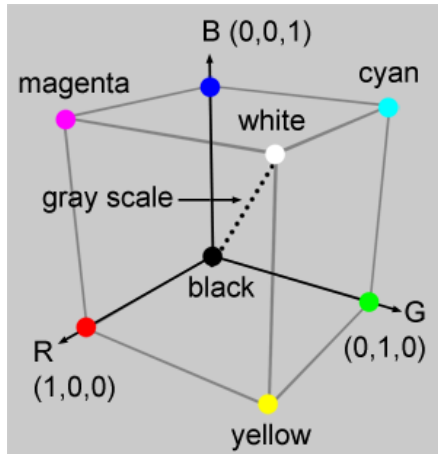


Figure 3.9: Unit cube representing the colors of the RGB model. The origin, given by the vertex $(0, 0, 0)$, represents the black color. The vertex $(1, 1, 1)$, opposite to the origin, represents the white color. The highlighted vertices on the axes represent the primary colors and the others are the complement of each. Each point inside the cube corresponds to a color that can be represented by the triple (r, g, b) , where $r, g, b \in [0, 1]$. The shades of gray are represented along the main diagonal of the cube, with each point along this diagonal being formed by equal contributions of each primary color. Source: adapted from Gonzalez and Woods (2002).

It is noteworthy that there are two ways of representing the RGB space: linear and non-linear. The aforementioned system shows the non-linear model, whose abbreviation is

²Theory started around 1500 when Leonardo da Vinci concluded that colors are produced by mixing yellow and blue, green and red, and white and black. In 1950, this theory was confirmed when optically-colored signals were detected at the optical connection between the retina and the brain (Gevers *et al.*, 2012).

$R'G'B'$ and is most used by devices and applications because of their similarity to the human visual system. In the literature, this system is frequently cited with the acronym RGB, which makes the nomenclature dubious, since the linear model is also called RGB and, therefore, the conversion between color spaces must be done with some caution. It is also important to note that linear RGB values are rarely used to represent an image since they are perceptually highly non-uniform (Plataniotis and Venetsanopoulos, 2000).

3.5.4 CMY color model

The CMY model is based on the complementary primary colors of the R, G, and B coordinates, which are given by Cyan, Magenta, and Yellow. Unlike RGB, is a subtractive color model, therefore, non-additive, in which colors are generated by subtracting the length of the dominant wave from the white light and, therefore, the resulting color corresponds to the light that is reflected (Gonzalez and Woods, 2002).

One way to get the CMY coordinates from the RGB system is:

$$\begin{bmatrix} C \\ M \\ Y \end{bmatrix} = \begin{bmatrix} B \\ R \\ R \end{bmatrix} + \begin{bmatrix} G \\ B \\ G \end{bmatrix} \quad (3.6)$$

or by making a change of coordinates by subtracting the primary colors R, G and B of the white color $W = (1, 1, 1)$ (Gonzalez and Woods, 2002):

$$\begin{bmatrix} C \\ M \\ Y \end{bmatrix} = \begin{bmatrix} 1 \\ 1 \\ 1 \end{bmatrix} - \begin{bmatrix} R \\ G \\ B \end{bmatrix} \quad (3.7)$$

Similarly to RGB, CMY is device dependent. The model is widely used in equipment that deposits colored pigments on paper, such as color printers or photocopiers. The Figure 3.10 shows how the model components are combined to generate the other colors.

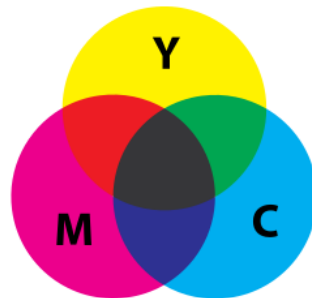


Figure 3.10: CMY subtractive color model. It is noteworthy that the intersection of yellow with magenta generates the red color, magenta with cyan generates the blue color and cyan with yellow generates the green color. Source: Rus (2008).

Overlapping the CMY primary colors in equal amounts to generate the black color typically creates a tint that is close to the brown or dark green. To avoid this undesired effect, the black component is usually added to the system, represented by the letter K. This operation gives rise to a new model known as CMYK (Gonzalez and Woods, 2002).

3.5.5 Color models of the YUV family

Color models of this family are also known as orthogonal color spaces. They are able to represent the color with statistically independent components – as independent as possible. In addition, to reduce the redundancy present in RGB color channels is also one of its key features (Kakumanu *et al.*, 2007).

The acronym YUV stands to a set of color spaces of which the luminance information, represented by the Y component, is coded separately from the chrominance, given by the components U and V. The components U and V are representations of signals of the difference of the blue subtracted from luminance ($B - Y$) and red subtracted from luminance ($R - Y$). It is used to represent colors in analog television transmission systems in the Phase Alternating Line (PAL) and Sequential Color with Memory (SECAM) (Pedrini and Schwartz, 2008).

The transformation of the RGB space to YUV is given by (Pedrini and Schwartz, 2008):

$$\begin{bmatrix} Y \\ U \\ V \end{bmatrix} = \begin{bmatrix} 0.299 & 0.587 & 0.114 \\ -0.147 & -0.289 & 0.436 \\ 0.615 & -0.515 & -0.100 \end{bmatrix} \begin{bmatrix} R \\ G \\ B \end{bmatrix} \quad (3.8)$$

where $0 \leq R, G, B \leq 1$.

Analogous to the YUV, the YIQ model was adopted in 1950 by the National Television System Committee (NTSC), an American standard for color television signal transmission. In this model, the Y component corresponds to luminance and the components I (hue) and Q (saturation) encode the chrominance information (Pedrini and Schwartz, 2008).

The transformation of the RGB space to YIQ is given by (Pedrini and Schwartz, 2008):

$$\begin{bmatrix} Y \\ I \\ Q \end{bmatrix} = \begin{bmatrix} 0.299 & 0.587 & 0.114 \\ 0.596 & -0.275 & -0.321 \\ 0.212 & -0.523 & -0.311 \end{bmatrix} \begin{bmatrix} R \\ G \\ B \end{bmatrix} \quad (3.9)$$

where $0 \leq R, G, B \leq 1$.

Another color model of the YUV family is the YCbCr, mathematically defined by a coordinate transformation with respect to some RGB space (Pedrini and Schwartz, 2008).

The YCbCr model is widely used in digital videos. In this system, the Y component represents luminance, computed as a weighted sum of RGB values. Cb component gives the measurement of the difference between the blue color and a reference value, similar to the Cr component which is the measurement of the difference between the red color and a reference value (Pedrini and Schwartz, 2008).

The transformation of the RGB space to YCbCr is given by (Pedrini and Schwartz, 2008):

$$\begin{bmatrix} Y \\ Cb \\ Cr \end{bmatrix} = \begin{bmatrix} 0.299 & 0.587 & 0.114 \\ -0.169 & -0.331 & 0.5 \\ 0.5 & -0.419 & -0.081 \end{bmatrix} \begin{bmatrix} R \\ G \\ B \end{bmatrix} \quad (3.10)$$

3.5.6 Color models of the HSI family

Hue, Saturation, and Intensity (HSI) models are best suited for image processing applications from the user point of view, due to the correlation with human perception of the color (Plataniotis and Venetsanopoulos, 2000).

In this model, as in YIQ, the intensity given by I component is decomposed from the chrominance information, represented by the hue (H) and saturation (S) (Plataniotis and Venetsanopoulos, 2000).

2000). The combination of these components results in a pyramidal structure which can be seen in Figure 3.11.

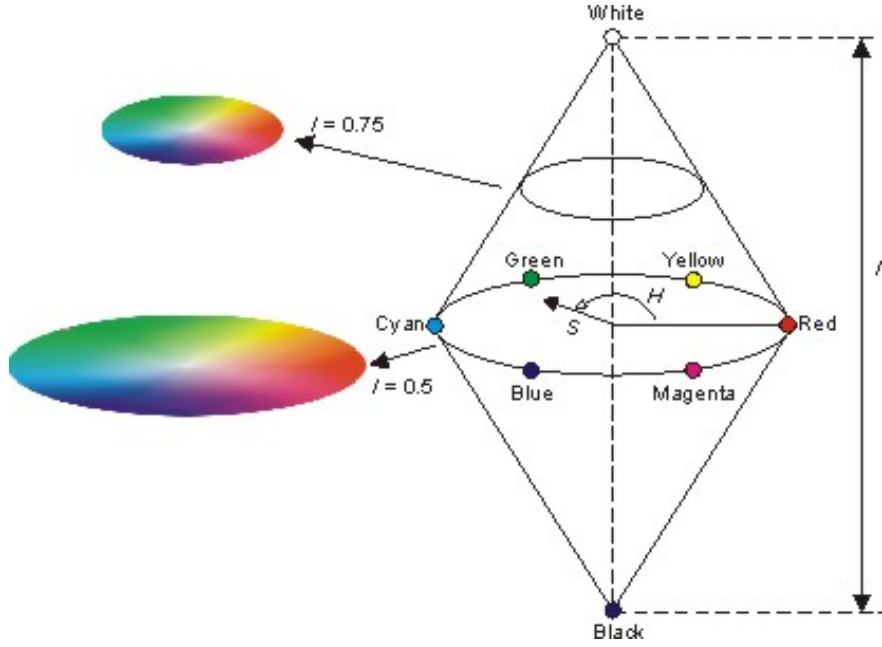


Figure 3.11: Graphical representation of the HSI model. The hue describes the color itself, in the form of an angle θ , where $\theta \in [0, 360]$. Red is at 0 degrees, yellow at 60, green at 120, and so on. The saturation component, which varies between 0 and 1, indicates how much color is polluted with white color. The intensity scale is between [0, 1], where 0 means black and 1, white. Source: [Ice \(2016\)](#).

The transformation of the components of the RGB space to HSI is given by the equations (Pedrini and Schwartz, 2008):

$$\begin{aligned} \theta &= \cos^{-1} \left(\frac{(R - G) + (R - B)}{2\sqrt{(R - G)^2 + (R - B)(G - B)}} \right) \\ H &= \begin{cases} \theta, & \text{if } B \leq G \\ 360 - \theta, & \text{otherwise} \end{cases} \\ S &= 1 - \frac{3\min(R, G, B)}{R + G + B} \\ I &= \frac{R + G + B}{3} \end{aligned} \quad (3.11)$$

It is important to note that the values R, G, and B must be normalized in the interval between 0 and 1. The intensity I and the saturation S are also normalized between 0 and 1.

Another model of this family is formed by the components Hue, Saturation and Value (HSV) and its three-dimensional graphical representation is a hexagonal pyramid derived from the RGB cube (Pedrini and Schwartz, 2008). Value, in this context, is the luminance component.

The various hue shades are represented at the top of the pyramid, the saturation is measured along the horizontal axis and value is measured along the vertical axis, which passes through the center of the pyramid. The hue, which corresponds to the edges around the vertical axis, varies from 0 (red) to 360 degrees and the angle between the vertices is 60

degrees. The saturation varies from 0 to 1 and is represented as the ratio of the purity of a given hue to its maximum purity, that is when $S = 1$. Value varies from 0, at the peak of the pyramid representing the black color, to 1 at the base, where the intensities of the colors are maximum (Pedrini and Schwartz, 2008).

The transformation of the components of the RGB space to HSV is given by the equations (Pedrini and Schwartz, 2008):

$$H = \begin{cases} 60 \frac{(G - B)}{M - m}, & \text{if } M = R \\ 60 \frac{(B - R)}{M - m} + 120, & \text{if } M = G \\ 60 \frac{(R - G)}{M - m} + 240, & \text{if } M = B \end{cases} \quad (3.12)$$

$$S = \begin{cases} \frac{(M - m)}{M}, & \text{if } M \neq 0 \\ 0, & \text{otherwise} \end{cases}$$

$$V = M$$

where $m = \min(R, G, B)$ and $M = \max(R, G, B)$. The luminance V and saturation S are normalized between 0 and 1. The H hue ranges from 0 to 360 degrees.

Similarly to HSV, the Hue, Saturation, and Lightness (HSL) model is a three-dimensional representation and is formed by two cones of height 1, whose bases are coincident (Pedrini and Schwartz, 2008).

The hue is determined by the points in the circle of the common bases to the cones. The saturation varies from 0 to 1, depending on the distance to the axis of the cone. The lightness is along the vertical axis common to the two cones and varies in the scale $[0, 1]$, where 0 means black and 1, white (Pedrini and Schwartz, 2008).

The conversion of the RGB space to HSL is given by the equations (Pedrini and Schwartz, 2008):

$$H = \begin{cases} 60 \frac{(G - B)}{M - m}, & \text{if } M = R \\ 60 \frac{(B - R)}{M - m} + 120, & \text{if } M = G \\ 60 \frac{(R - G)}{M - m} + 240, & \text{if } M = B \end{cases} \quad (3.13)$$

$$S = \begin{cases} \frac{(M - m)}{M + m}, & \text{if } 0 < L \leq 0,5 \\ \frac{(M - m)}{2 - (M + m)}, & \text{if } L > 0,5 \\ 0, & \text{if } M = m \end{cases}$$

$$L = \frac{M + m}{2}$$

where $m = \min(R, G, B)$ and $M = \max(R, G, B)$. The lightness L and saturation S are normalized between 0 and 1. Note that the transformation of the H component is the same as that used in the conversion of the RGB to HSV space in Eq. 3.12 and varies between 0 and 360 degrees.

All the color models of this family have the property of thinking of lighter colors, obtained by increasing the brightness or lightness, and darker colors, by the diminution of the same values. The intermediate colors are produced by decreasing the saturation (Pedrini and Schwartz, 2008).

Chapter 4

Correlation rules and proposed extension

A state of the art skin detection method has been recently developed by Brancati *et al.* (2017). In this chapter, we review the method and extend it adding more rules to enforce the constraints and seeking for a better accuracy in terms of false positive rate without hurting the performance of the original method.

4.1 Correlation rules on YCrYCb colormap

In order to describe the proposed extensions, we will first present the original method that is based on the definition of image-specific trapezoids, named T_{YCb} and T_{YCr} , in the YCb and YCr subspaces, respectively. The trapezoids are essential to verify a relationship between the chrominance components Cb and Cr in these subspaces (Brancati *et al.*, 2017).

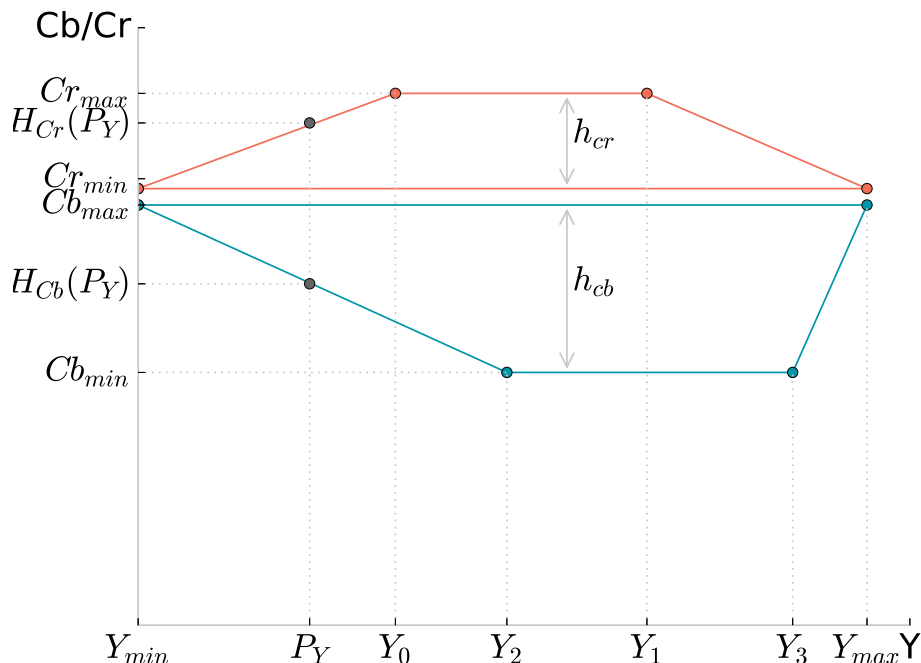


Figure 4.1: Graphical representation of the trapezoids as well as the parameters $Y_{min} = 0$, $Y_{max} = 255$, Y_0 , Y_1 , Y_2 , Y_3 , Cr_{min} , Cr_{max} , Cb_{min} , Cb_{max} , h_{Cr} , h_{Cb} , $H_{Cr}(P_Y)$, $H_{Cb}(P_Y)$. Source: adapted from (Brancati *et al.*, 2017).

To show the correlations, Brancati et. al. present the YCbCr space as a 2D graph where the Y is presented in the abscissa and the Cb in a different axis. The base of the trapezoids T_{YCr} and T_{YCb} (Fig. 4.1) are given by the coordinates (Y_{min}, Cr_{min}) and (Y_{min}, Cb_{max}) in the YCr and YCb , respectively (Brancati et al., 2017). The values $Cr_{min} = 133$, $Cb_{max} = 128$ were selected according to Chai and Ngan (1999) where a skin color map was designed using a histogram approach based on a given set of training images. Chai and Ngan observed that the Cr and Cb distributions of skin color falls in the ranges [133, 173] and [77, 127], respectively, regardless the skin color variation in different races.

The Cr_{max} parameter is calculated dynamically, taking into account the histogram of the pixels with Cr values in the range $[Cr_{min}, 183]$, looking for the maximum value of Cr associated with at least 0.1%¹ of pixels in the image. The same applies to Cb_{min} , taking the histogram with Cb values in the range $[77, Cb_{max}]$. Y_0 and Y_1 (shorter base of the upper trapezoid) are, respectively, the 5th and 95th percentile of the luminance values associated with the pixels of the image with $Cr = Cr_{max}$ (Brancati et al., 2017). A similar procedure is used to find the values of the shorter base of the other trapezoid, Y_2 and Y_3 (see Fig. 4.2 for an example).

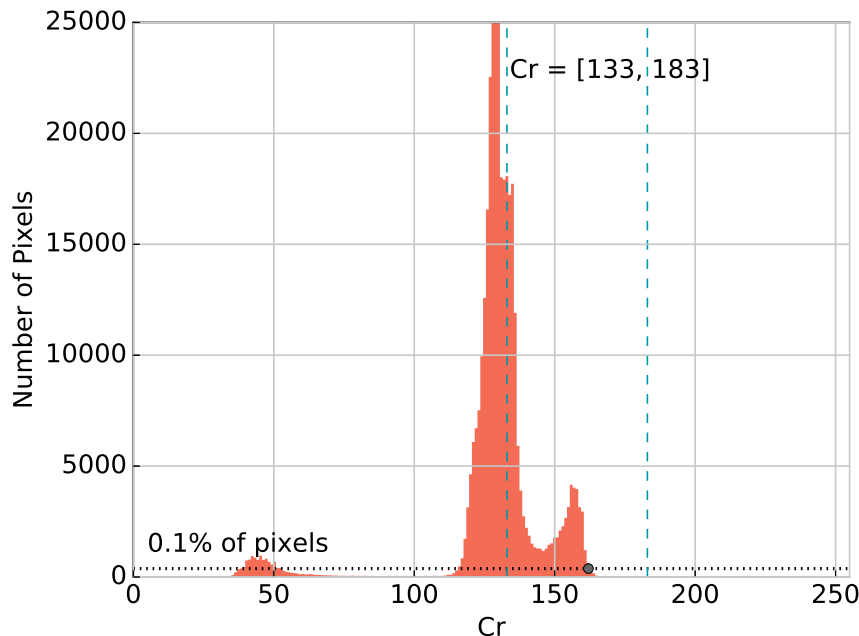


Figure 4.2: Computation of $Cr_{max} = 162$ based on Cr values histogram of a 724 x 526 image. Source: adapted from (Brancati et al., 2017).

The correlation rules between the chrominance components P_{Cr} and P_{Cb} of a pixel P are defined as (Brancati et al., 2017):

- the minimum difference between the values P_{Cr} and P_{Cb} , denoted I_P ;
- an estimated value of P_{Cb} , namely P_{Cb_s} ;
- the maximum distance between the points (P_Y, P_{Cb}) and (P_Y, P_{Cb_s}) , denoted J_P .

Therefore, to determine if P is skin, the following equations must hold (Brancati et al., 2017):

$$P_{Cr} - P_{Cb} \geq I_P \quad (4.1)$$

¹In Brancati et al. (2017) this rate is reported to be equal to 10%. However, in the distributed source code we found the value 0.1%, that we are using in the experiments.

$$|P_{Cb} - P_{Cb_s}| \leq J_P \quad (4.2)$$

The estimated value P_{Cb_s} is given by ²:

$$P_{Cb_s} = Cb_{max} - dP_{Cb_s} \quad (4.3)$$

where ³:

$$dP_{Cb_s} = \alpha \cdot dP_{Cr} \quad (4.4)$$

$$dP_{Cr} = P_{Cr} - Cr_{min} \quad (4.5)$$

² dP_{Cb_s} is the distance between the points (P_Y, P_{Cb_s}) and (P_Y, Cb_{max}) in the YCb subspace, calculated on the basis of dP_{Cr} , observing the inversely proportional behavior of the components. α is the rate between the normalized heights of the trapezoids in relation to the P_Y value (Brancati *et al.*, 2017).

³ dP_{Cr} is the distance between (P_Y, P_{Cr}) and (P_Y, Cr_{min}) points in the YCr subspace (Brancati *et al.*, 2017).

The coordinates of the other sides of the trapezoids are given by $[P_Y, H_{Cr}(P_Y)]$ and $[P_Y, H_{Cb}(P_Y)]$, such that (Brancati *et al.*, 2017):

$$H_{Cr}(Y) = \begin{cases} Cr_{min} + h_{Cr}\left(\frac{Y - Y_{min}}{Y_0 - Y_{min}}\right) & Y \in [Y_{min}, Y_0] \\ Cr_{max} & Y \in [Y_0, Y_1] \\ Cr_{min} + h_{Cr}\left(\frac{Y - Y_{max}}{Y_1 - Y_{max}}\right) & Y \in [Y_1, Y_{max}] \end{cases} \quad (4.6)$$

$$H_{Cb}(Y) = \begin{cases} Cb_{min} + h_{Cb}\left(\frac{Y - Y_2}{Y_{min} - Y_2}\right) & Y \in [Y_{min}, Y_2] \\ Cb_{min} & Y \in [Y_2, Y_3] \\ Cb_{min} + h_{Cb}\left(\frac{Y - Y_3}{Y_{max} - Y_3}\right) & Y \in [Y_3, Y_{max}] \end{cases} \quad (4.7)$$

where $h_{Cr} = Cr_{max} - Cr_{min}$ and $h_{Cb} = Cb_{max} - Cb_{min}$, which are the heights of T_{YCr} and T_{YCb} , respectively.

The computation of those points are useful for the calculation of α . We first compute the distances $\Delta_{Cr}(P_Y)$ and $\Delta_{Cb}(P_Y)$ between the points $(P_Y, H_{Cr}(P_Y))$, $(P_Y, H_{Cb}(P_Y))$ and the base of the trapezoids (Brancati *et al.*, 2017):

$$\Delta_{Cr}(P_Y) = H_{Cr}(P_Y) - Cr_{min} \quad (4.8)$$

$$\Delta_{Cb}(P_Y) = Cb_{max} - H_{Cb}(P_Y) \quad (4.9)$$

Next, the distances are normalized with respect to the difference in size of the trapezoids (Brancati *et al.*, 2017):

$$\Delta'_{Cr}(P_Y) = \begin{cases} \Delta_{Cr}(P_Y) \cdot \frac{A_{T_{YCb}}}{A_{T_{YCr}}} & \text{if } A_{T_{YCr}} \geq A_{T_{YCb}} \\ \Delta_{Cr}(P_Y) & \text{otherwise} \end{cases} \quad (4.10)$$

$$\Delta'_{Cb}(P_Y) = \begin{cases} \Delta_{Cb}(P_Y) & \text{if } A_{T_{YCr}} \geq A_{T_{YCb}} \\ \Delta_{Cb}(P_Y) \cdot \frac{A_{T_{YCr}}}{A_{T_{YCb}}} & \text{otherwise} \end{cases} \quad (4.11)$$

where $A_{T_{YCr}}$ and $A_{T_{YCb}}$ are the areas of trapezoid T_{YCr} and T_{YCb} , respectively.

Then, the value of α is given by (Brancati *et al.*, 2017):

$$\alpha = \frac{\Delta'_{Cb}(P_Y)}{\Delta'_{Cr}(P_Y)} \quad (4.12)$$

Finally, I_P and J_P are given by (Brancati *et al.*, 2017):

$$I_P = sf \cdot [(\Delta'_{Cr}(P_Y) - dP_{Cr}) + (\Delta'_{Cb}(P_Y) - dP_{Cb_s})] \quad (4.13)$$

$$J_P = dP_{Cb_s} \cdot \frac{dP_{Cb_s} + dP_{Cr}}{\Delta'_{Cb}(P_Y) + \Delta'_{Cr}(P_Y)} \quad (4.14)$$

where:

$$sf = \frac{\min((Y_1 - Y_0), (Y_3 - Y_2))}{\max((Y_1 - Y_0), (Y_3 - Y_2))} \quad (4.15)$$

4.2 Extended method

The hypothesis defined in the original method is based on rules that an estimated value of the point P_{Cb} , namely P_{Cb_s} , must hold in order for the correlation to be valid. On the

basis of the inversely proportional behavior of the chrominance components, we will rewrite the correlation rules with respect to the P_{Cr} point.

Thus, we have to refactor the correlation rules to put them in terms of the estimated value of P_{Cr} , that we denote as P_{Cr_s} ⁴:

$$P_{Cr_s} = dP_{Cr_s} + Cr_{min} \quad (4.16)$$

where⁵:

$$dP_{Cr_s} = \alpha \cdot dP_{Cb} \quad (4.17)$$

$$dP_{Cb} = Cb_{max} - P_{Cb} \quad (4.18)$$

Next, the constraints given by I_P and J_P in the Eq. 4.13 and 4.14 respectively, can be redefined as:

$$I'_P = sf \cdot [(\Delta'_{Cr}(P_Y) - dP_{Cr_s}) + (\Delta'_{Cb}(P_Y) - dP_{Cb})] \quad (4.19)$$

$$J'_P = dP_{Cr_s} \cdot \frac{dP_{Cb} + dP_{Cr_s}}{\Delta'_{Cb}(P_Y) + \Delta'_{Cr}(P_Y)} \quad (4.20)$$

Therefore, to determine if the pixel P is skin, we have to modify the conditions given by Eq. 4.1 and 4.2:

$$P_{Cr} - P_{Cb} \geq I'_P \quad (4.21)$$

$$|P_{Cr} - P_{Cr_s}| \leq J'_P \quad (4.22)$$

Doing this simple extension, we are now able to apply the method to the same sets of images to evaluate, in fact, the inversely proportional behavior of the chrominance components. More than that, we can combine all these constraints, given by the pair equations 4.1 and 4.2, 4.21 and 4.22, to reinforce the firstly defined hypothesis.

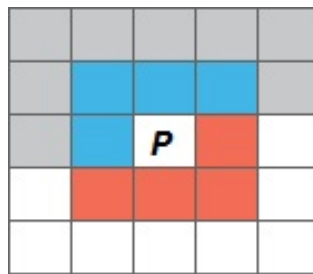


Figure 4.3: Neighbors evaluation with respect to P . If the image is scanned in raster order, $N_8^-(P)$ is the set of points that can be reached before P in an 8-neighbors window. Source: proposed by the author.

4.3 Neighborhood extended method

Both methods presented in sections 4.1 and 4.2 can be applied to detect skin pixels, either separated or in a conjunction rule. However, skin pixels do not usually appear isolated and

⁴ dP_{Cr_s} is the distance between the points (P_Y, P_{Cr_s}) and (P_Y, Cr_{min}) in the YCr subspace, calculated on the basis of dP_{Cb} , observing the inversely proportional behavior of the components. α is the rate between the normalized heights of the trapezoids in relation to the P_Y value.

⁵ dP_{Cb} is the distance between (P_Y, P_{Cb}) and (P_Y, Cb_{max}) points in the YCb subspace.

we could improve the method using some of the already processed neighbors of a pixel P , in order to decide if P represents human skin, or not.

To do that, let $N_8^-(P)$ be the *8-neighbors* of P that can be reached before P when scanning the image in raster order, that means the blue points in Figure 4.3 () .

Thus, we classify P as skin in the following manner: if the constraints given by the pair of equations 4.1 and 4.2, as well as 4.21 and 4.22 hold, then P is classified as skin. When only one of the conditions is satisfied, then we check the decision in $N_8^-(P)$. If three or more pixels are skin, then P will also be classified as a skin pixel. Figure 4.4 shows a flowchart of the aforementioned procedure described.

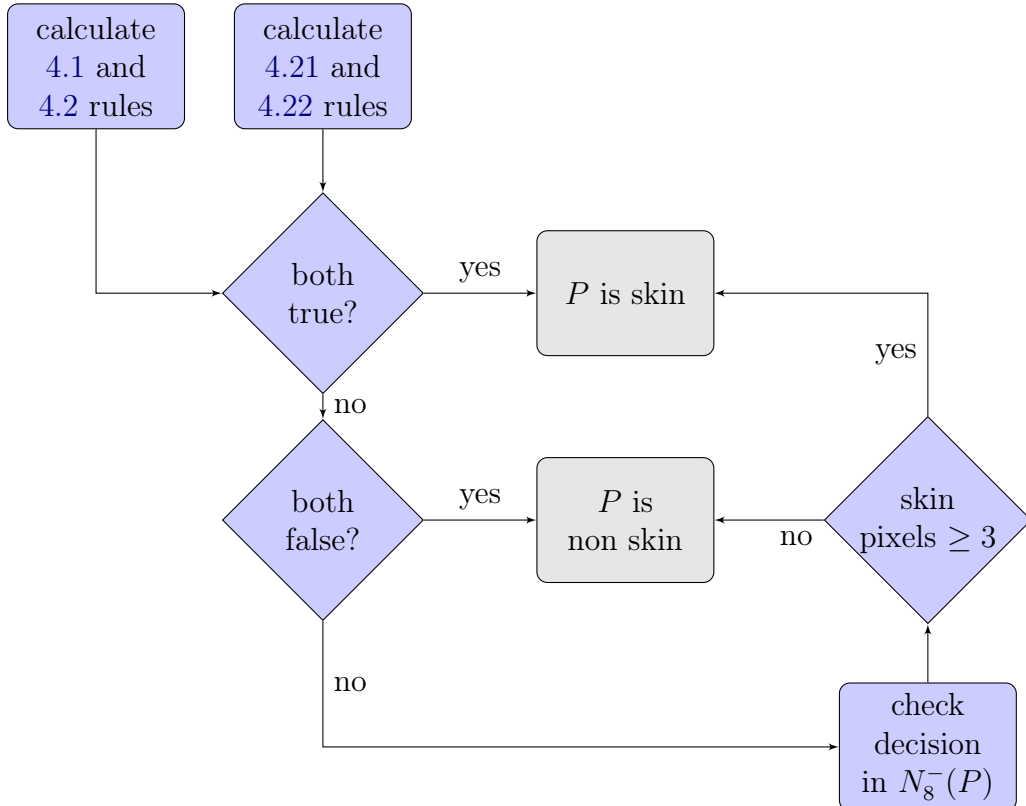


Figure 4.4: Flowchart of our proposed neighbors method. In **both false** decision, the **no** path means that one of the rules is true and we are in doubt if P is skin or not – here is where the neighbors are used to find out the label of P . Source: proposed by the author.

4.4 Supplementary neighborhood operations

The given neighborhood method presented in Section 4.3 will end up with an undesired behavior on the output images that we called *diagonal effect* (see Fig. 4.5). In addition, besides being visually undesirable, the *diagonal effect* phenomenon causes us to have an increase in the false positive rate. This is caused due to the shape of the window being used. Once we look only for the four already seen pixels of the *8-neighbors* window, the operation is so based in a non-symmetry mask. Ideally, we could use another neighborhood strategy and look for all the eight neighbors of the pixel P being evaluated. However, this particular implementation can add extra computational time and hurt the performance of the method.

Therefore, we created an adaptation of the neighborhood method shown in Section 4.3. In this version, we basically scan the image, with a size of $W \times H$, in the raster order, and

apply the original and the extended reverse rules for every single pixel. We keep the both results in a matrix of the same size ($W \times H$) of the input image. For each coordinate of this output matrix, we will have a two positions vector with the result of the original and reverse rules answer for this pixel. Next, we read each position of this output matrix and we apply a 8-neighbors operations in four different ways:

- (1) we look in the rules answer performing an AND. In other words, if both original and reverse rules are saying this pixel is skin, then we classify it as skin;
- (2) we look in the rules answer performing an OR. In other words, if one of the rules (original or reverse) is saying this pixel is skin, then we classify it as skin;
- (3) we look in the neighbors only querying the original (P_{Cb_s}) rules;
- (4) we look in the neighbors only querying the reversed (P_{Cr_s}) rules.

Of course, this variation will add some additional computational cost once we will scan the image one more time. This implementation can be enhanced, but the idea here is to only explore better the connectivity of the 8-neighbors window and check, on the basis of a symmetric mask window, if the *diagonal effect* is gone as well as the measures are improved. Some experiments can be seen further in Section 5.4.

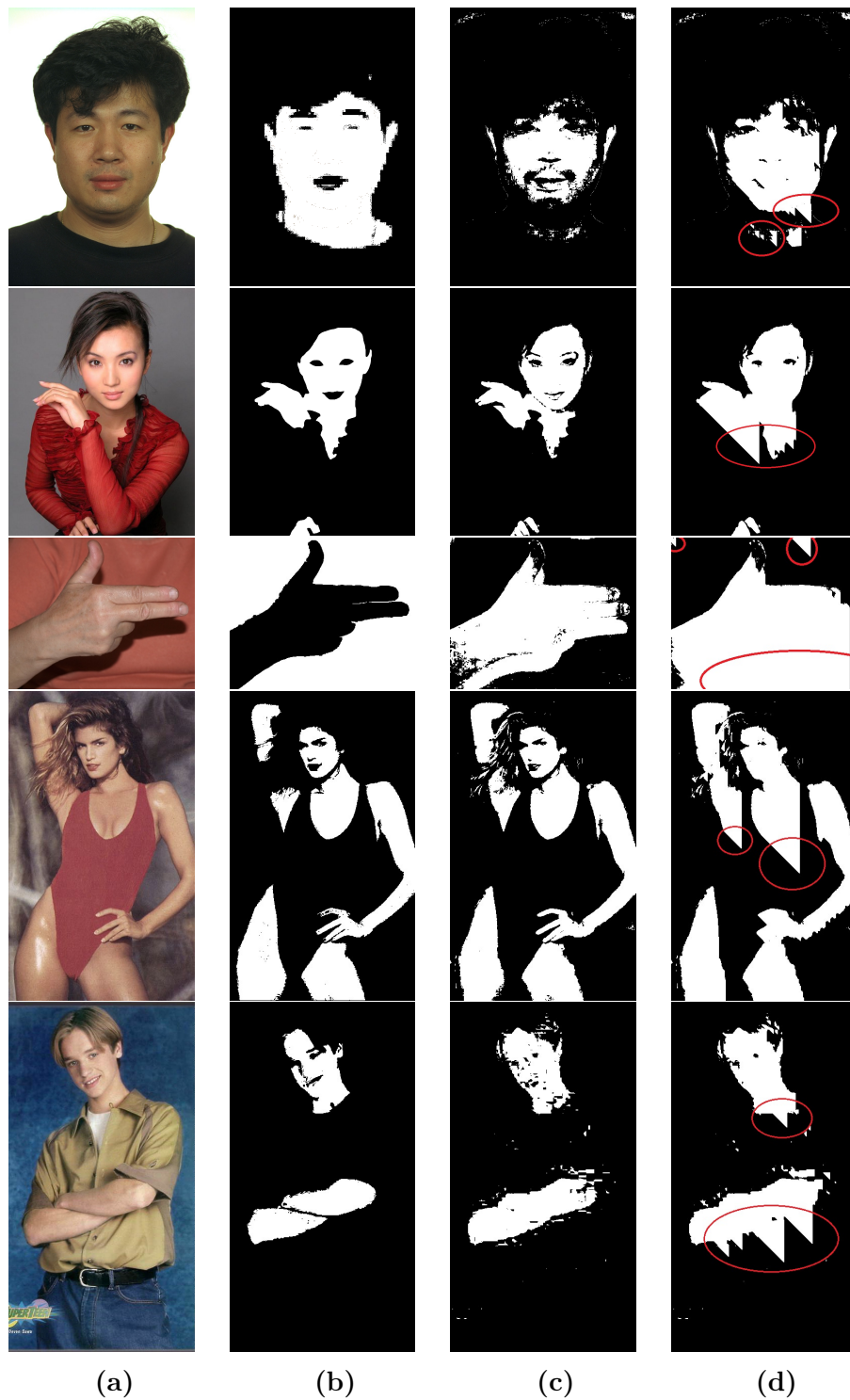


Figure 4.5: Image samples with the diagonal effect after the neighbors method segmentation. Each image is from (top-down) SFA, Pratheepan, HGR, and Compaq datasets, respectively, where: (a) original image (b) ground truth (c) combined method (f) neighbors method. Independently of the classification accuracy, we can clearly see the diagonal effect present in the output of the neighbors method segmentation in comparison with combined. Besides being a visually undesirable effect, this phenomenon causes us to have an increase in the false positive rate.

4.5 Parameters tuning via a grid search strategy

As we could see in previous sections, this model is based on the definition of trapezoids to fit the skin color pixels distribution from a given image. According to Brancati *et al.* (2017), the coordinates of each trapezoid within the YCr and YCb sub-spaces are calculated based on the Y luminance component values. Just to remember what was seen before, Y_0 and Y_1 are those values used to define the shorter side of the upper trapezoid, and Y_2 and Y_3 are the points used to define the shorter side of the lower trapezoid.

Y_0 and Y_1 are, respectively, the 5th and 95th percentile of the luminance values associated with the pixels of the image with $Cr = Cr_{max}$ (see Fig. 4.2 for an example). Similarly, Y_2 and Y_3 are, respectively, the 5th and 95th percentile of the luminance values associated with the pixels of the image with $Cb = Cb_{min}$.

To the best of our knowledge, there is no justification to choose the 5th and 95th percentile to be the right parameters to define the trapezoids coordinates. For this reason, we decided to trigger different combinations of these parameters to figure out which pair better works for the model fitting. In addition, we would like to answer the question: why 5th and 95th percentile have been used?

Thus, we used a well-known technique called grid search to find the best range combination from a hyper-parameter space. By constructing the model in this manner, we can leverage the classification results by finding the optimized parameters' combination, if other different from the ones defined earlier by Brancati *et al.* (2017). Despite we do not exhaustively consider all parameter combinations, we used an efficient search strategy by sampling a given number of candidates. For each chosen parameters candidate, we dynamically used them in the combined method⁶ to test every single image of each dataset described in section 5.1. Lastly, we sort the results table using respectively, *F-measure*, *Precision*, and *Recall* metrics, as detailed in section 5.2, and established a comparison to get optimized parameters. The algorithm TRAPEZOIDS-PARAMETERS-GRID-SEARCH(*dataset*) shows how the grid search have been performed.

```

TRAPEZOIDS-PARAMETERS-GRID-SEARCH(dataset)
1    $P_{min} = 5$ 
2    $Results = []$ 
3
4   while  $P_{min} \leq 95$ 
5      $P_{max} = P_{min}$ 
6     while  $P_{max} \leq 95$ 
7       SET-COMBINED-METHOD-Y-PARAMETERS( $P_{min}, P_{max}$ )
8       SEGMENT-DATASET-IMAGES(dataset)
9       Precision, Recall, Fmeasure = COMPUTE-METRICS(dataset)
10      PUSH(Results,  $P_{min}, P_{max}, Precision, Recall, Fmeasure$ )
11
12       $P_{max} = P_{max} + 5$ 
13       $P_{min} = P_{min} + 5$ 
14
15  SORT-BY(Results, Fmeasure, Precision, Recall)
16  return Results
```

⁶In fact, we could apply this approach in any of the described methods, but once the trapezoids definition do not change among them, we think that employing it only in combined method is sufficient for the parameters optimization.

In short, TRAPEZODS-PARAMETERS-GRID-SEARCH(*dataset*) will trigger combinations of P_{min} and P_{max} ⁷ percentiles in the range [5, 95] with a step of 5. In line 7, the parameters are changed in the combined method and applied further in 8 to classify each image within the dataset. Next, the metrics are computed on every single image in line 9 by comparing the output with the ground truth. The resulting metrics are pushed into *Results* matrix in line 10. We keep an average of overall images classified in each dataset. Finally, we sort the results matrix according to the criteria aforementioned at the end of the procedure.

Detailed output of this experiments and analysis can be seen in chapter 5, specifically in section 5.5, where an examination of the behavior of the most performing parameters is given as well as others which did not succeed.

⁷ P_{min} is the minimum percentile index of the *Y* luminance values. P_{max} is the maximum percentile index of the *Y* luminance values.

Chapter 5

Evaluation

In this chapter, we present some experimental evaluations of the proposed extensions along with the original method in four widely known datasets: SFA, Pratheepan, HGR, and Compaq. In addition, a brief definition of the evaluation metrics used is shown for the sake of clarity. We also provide some results of the supplementary neighborhood adaptation that we built to remove the *diagonal effect* as well as to explore different neighbors techniques. Finally, we show the grid search parameters experiments results with aim of trapezoids parameters tuning. All the experiments are analyzed and discussed in each section separately.

5.1 Datasets

Datasets are an integral part of the field of computer vision. In the particular case of computer vision, datasets consist, primarily, of images or videos for tasks such as object detection, motion tracking, segmentation, and classification. In general, they are constructed with tens, hundreds, or even thousands of images in different environments, distinct illumination conditions, various quality and resolution, and many other aspects.

We gathered four widely known datasets, SFA, Pratheepan, HGR, and Compaq, which will be briefly introduced in next sections, to be used in our experiments. Together, they sum up 7,423 images of different size and resolution, and more than 1.5 billion pixels tested in all the experiments, counting only the original images.

5.1.1 UCI

Named UCI in this work, this dataset was proposed by [Bhatt and Dhall \(2012\)](#) and obtained from the machine learning repository of the University of California in Irvine ([Lichman, 2013](#)). The dataset consists of pixel samples of images of various skin and non-skin textures obtained from thousands of arbitrary faces images of different ages, gender, and races ([Minear and Park, 2004; Phillips et al., 1996](#)).

The UCI contains 245,057 samples, composed of 3 attributes that constitute the input vector $x = [x_1, x_2, x_3]$, $x \in \mathbb{R}^d$, where d is the space dimension which represents, respectively, blue (B), green (G) and red (R) channels of the RGB color model. In addition, a fourth column determines the class to which the sample x belongs, denoted by y , where $y \in Y$ and $Y = \{+1, -1\}$. In other words, each sample is an RGB pixel with a given label.

The Table 5.1 exemplifies a short excerpt from the UCI database. It is worth mentioning that 194,198 out of the 245,057 are non-skin pixels and 50,859 pixels with different skin tones. In addition, the images that were used to extract the dataset were not made available by the authors.

B	G	R	Label
74	85	123	1
207	215	255	1
74	82	122	1
202	211	255	1
54	72	125	1
...
166	164	116	-1
148	150	91	-1
29	26	5	-1
167	166	115	-1
180	177	133	-1

Table 5.1: Excerpt with samples from the UCI dataset. Each of the first three columns represents a pixel channel of the RGB color space ranging from 0 to 255. The fourth column is the label assigned to the sample, which can assume +1 if it is skin and -1, otherwise. Originally, the class representing a non-skin pixel had value 2, replaced by -1 for compliance with the experiments.

Since the data are points in the RGB space, it is possible to plot it for a better interpretation of them, as shown in the Figure 5.1.

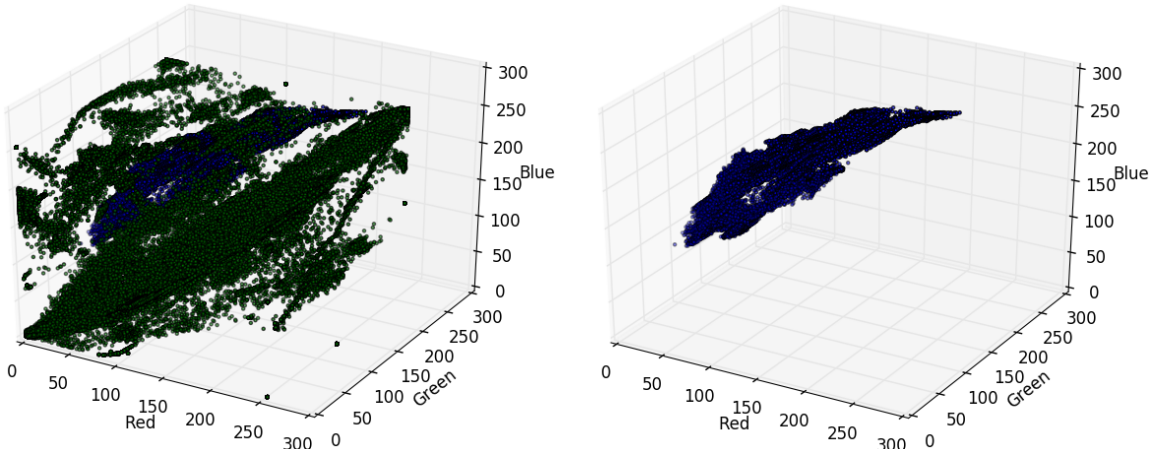


Figure 5.1: 3-dimensional view of the RGB channels of the UCI dataset. The blue points are skin samples and the green ones are non-skin. On the left are all samples of the dataset; to the right only the skin samples. Source: proposed by the author.

5.1.2 SFA

SFA, the name of the dataset proposed by Casati *et al.* (2013), stands for Skin of FERET and AR Database. The SFA is a set of images of frontal faces obtained from two other color image databases: the FERET, created by Phillips *et al.* (1996), and the AR proposed by Martínez and Benavente (1998), which provided 876 and 242 images each, respectively. It is important to notice that AR images have a white background and small variations of skin color. In other words, the environment is more controlled than the images in FERET (Casati *et al.*, 2013). Figure 5.3 shows some of the 1,118 samples available.

Casati *et al.* (2013) also extracted different window patches of each skin and non-skin samples to facilitate future research. The samples were randomly generated considering the

ground truth mask¹ of each image, being three samples of skin and five of non-skin. Each sample is a window of size $n \times n$, where n is odd, with a central pixel, from which other sample sizes have been created, ranging from 1×1 to 35×35 , as can be seen in Figure 5.2.

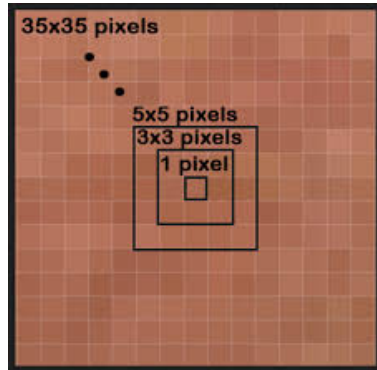


Figure 5.2: Structure of the windows that form the SFA patch samples. In total, there are 3,354 skin samples and 5,590 non-skin samples for each window size. Source: Casati et al. (2013).

¹Ground truth is the term used to denote an image whose point of interest is properly segmented and highlighted, discarding the remaining pixels giving them uniform colors.

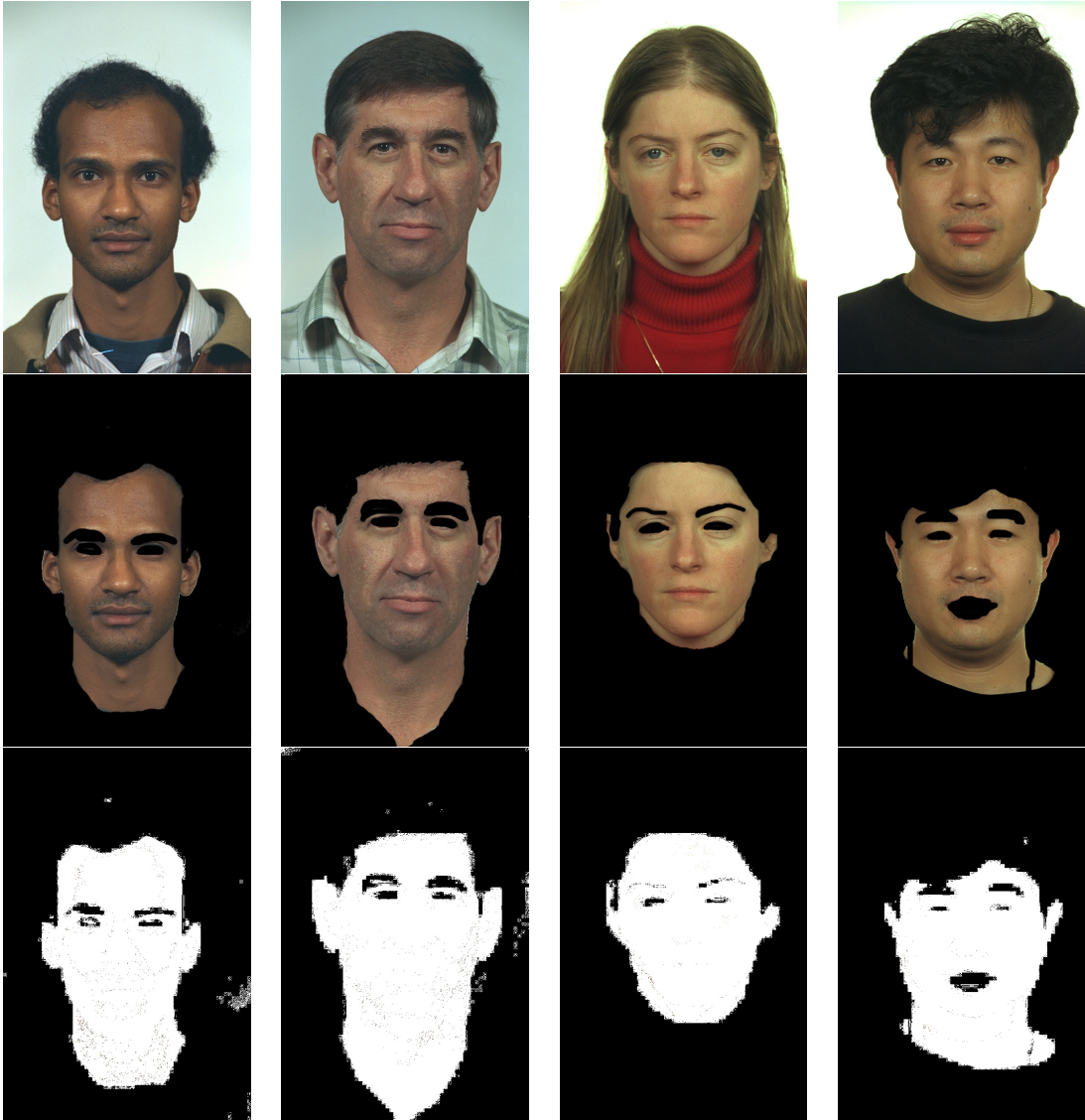


Figure 5.3: Examples of SFA face image database. The first row is the original images and the second contains the colored ground truth with the skin color pixels annotated manually. The black color $RGB = (0, 0, 0)$ was assigned to all pixels in the background. In the third row, we have the binary ground truth images. We generated these samples based on the colored ground truth, by creating a mask, assigning $(255, 255, 255)$ for the pixels which do not belong to the background $(0, 0, 0)$. One can see some noise in the results, but the samples were enough for further experiments. In addition, the original images were not perfectly annotated. Therefore, some salt noise can be seen in non-skin regions. Source: Casati et al. (2013).

It is worth mentioning that we do not use these patches in our experiments. Once the methods tested in this work only depends on the input image itself. Therefore, we can simply ignore these sampling patches during experiments. However, one could use them to evaluate the ability of the methods in terms of false detection rate, once the patches are made available for skin and non-skin labeled images separately.

5.1.3 Pratheepan

The images in the Pratheepan dataset were downloaded randomly from Google for human skin detection research. There are 78 images of family and face captured with a range

of distinct cameras using different color enhancement and under different illumination conditions Tan *et al.* (2012). Figure 5.4 shows some of the 78 samples available.



Figure 5.4: Examples of Pratheepan skin dataset. At the top row is the original image, and at the bottom row, the ground truth with the skin color pixels annotated. Here, the ground truth are binary images, where the black color $RGB = (0, 0, 0)$ was assigned to all pixels in the background. Source: Tan *et al.* (2012).

5.1.4 HGR

The database for Hand Gesture Recognition (HGR) contains the gestures from Polish and American Sign Language. There are 1,558 images acquired in different conditions of background, dimensions, and lightning. In addition to original and ground truth binary skin mask images, it includes hand feature points locations in separate files. Figure 5.5 shows some of the 1,558 samples available (Grzejszczak *et al.*, 2016; Kawulok *et al.*, 2014; Nalepa and Kawulok, 2014).

The images within it were acquired in three different series. A set of 899 was captured in uncontrolled background and lighting. A small set of 85 was obtained in gray (44) and uncontrolled (41) background; the lighting was uniform. The third group contains 574 images in controlled background (green tone), using uniform lighting conditions (Grzejszczak *et al.*, 2016; Kawulok *et al.*, 2014; Nalepa and Kawulok, 2014).



Figure 5.5: Examples of HGR skin dataset. At the top row is the original image and at the bottom row, the ground truth with the skin color pixels annotated. Different from Pratheepan and SFA, the ground truth is also binary images, but the black color $RGB = (0, 0, 0)$ was assigned to all pixels when they represent skin patches – and we take this in consideration during experiments. Source: Grzejszczak et al. (2016); Kawulok et al. (2014); Nalepa and Kawulok (2014).

5.1.5 Compaq

Compaq can be considered as the first large skin dataset and, probably is the most used for skin detection classifiers. It consists of 13,635 images crawled from the internet, which 4,670 contain skin regions and another subset of 8,965 images not containing any skin. The ground truth images are poorly annotated on the basis of an automatic software tool (Mahmoodi and Sayedi, 2016).

It is worth mentioning that this database is no longer available and we had obtained a copy of it by contacting the authors. We also had to fix some few images due to lack of ground truth or files corrupted. The final amount of images with skin used in the experiments is 4,669. Figure 5.6 shows some of the 4,669 images with skin samples available used in the experiments (Jones and Rehg, 2002).

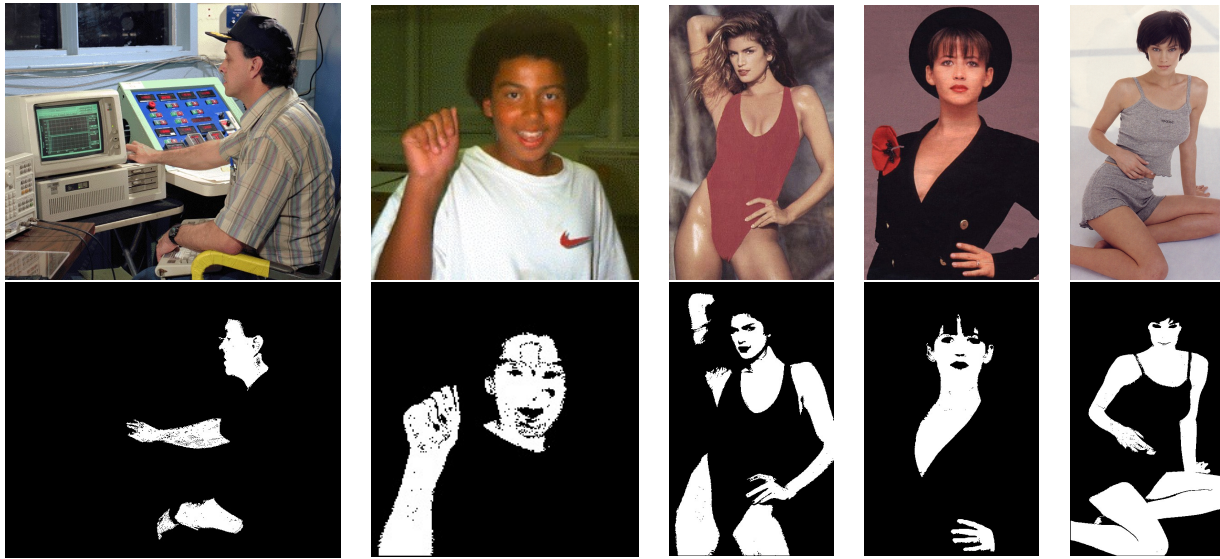


Figure 5.6: Examples of Compaq skin/non-skin dataset. At the top row is the original image, and at the bottom the ground truth with the skin color pixels annotated. Here, the ground truth are binary images, where the black color $RGB = (0, 0, 0)$ was assigned to all pixels in the background. Source: *Jones and Rehg (2002)*.

5.2 Evaluation measures

Precision, Recall, Specificity and *F-measure* have been used as evaluation metrics. They are the same used in [Brancati et al. \(2017\)](#) to compare the performance with state-of-the-art methods. They are also widely used by the scientific community. These metrics are given by the following formulas:

$$Precision = \frac{TP}{TP + FP}$$

$$Recall = \frac{TP}{TP + FN}$$

$$Specificity = \frac{TN}{TN + FP}$$

$$F - measure = 2 \times \frac{Precision \times Recall}{Precision + Recall}$$

where TP, TN, FP, FN are, respectively, the number of true positive, true negative, false positive, and false negative pixels counted in the image, which are obtained from the confusion matrix (see Table 5.2).

		prediction outcome	
		skin	non-skin
ground truth	skin	True Positive	False Negative
	non-skin	False Positive	True Negative

Table 5.2: Confusion matrix table used to count the number of true positive, true negative, false positive, and false negative pixels in the image during experiments. These numbers are fundamental input for evaluation measures.

5.3 Rule-based experiments

In this section, we present some experimental evaluations of the proposed extensions described in sections 4.2 and 4.3, as well as the original method in four widely known datasets: SFA, Pratheepan, HGR, and Compaq. The latest three of them have also been used in Brancati *et al.* (2017).

Table 5.3 shows quantitative result metrics of the experiments. Column 1 refers to the dataset used. Column 2 refers to the method being experimented: Original for the original hypothesis; Reverse refers to the reverse hypothesis with respect to P_{Cr_s} parameter; Combined refers to the combination of both of the former methods (see Sec. 4.2); Neighbors refers to the extension of the method using the neighborhood approach (see Sec. 4.3).

The original method was compared with six well known rule-based methods in the literature using four different datasets, three of them, HGR, Pratheepan and Compaq, we have also been used here. We applied the methods against a fourth dataset (SFA) to increase and strengthen the different number of samples tested.

Because the method had the best *F-measure* in the HGR and Pratheepan datasets in comparison with the other six methods and, in addition, because it performed the top first *Precision* in HGR and second in Pratheepan, we decided to compare the proposed extensions only to the original method.

As one can see in Table 5.3, the reverse hypothesis performed better than the original method and achieved the best *Recall* in HGR and SFA. It also achieved the best *F-measure* in SFA with a 0.8125 rate, which gave almost 0.25 in gain compared to the original.

It is important to note that, the significant improvement of the *Recall* in HGR and SFA datasets is, probably, due to the nature of the images that form each of them. HGR and SFA contain images where we have a great concentration of skin pixels – hands and arms in the case of HGR, and faces in the case of SFA occupying a considerable region of the image. Furthermore, a large part of them was collected in controlled environments, on the background and lighting conditions point of view. Thus, this behavior must be taken into consideration when selecting the method to apply within an application, since this can be decisive for a potential performance improvement.

In general, the reverse method increased the *Recall* but did not perform well in *Precision* and *Specificity* measures. When we combined both methods, the best *Precision* and *Specificity* were achieved for all datasets but it loses some performance in *Recall*. However, it still

Dataset	Hypothesis	Precision	Recall	Specificity	F-measure
Compaq	Original	0.4354	0.8046	0.8046	0.5650
	Reverse	0.3971	0.7232	0.7921	0.5127
	Combined	0.4906	0.6251	0.8856	0.5498
	Neighbors	0.4708	0.7421	0.8463	0.5761
Pratheepan	Original	0.5513	0.8199	0.8230	0.6592
	Reverse	0.5249	0.7326	0.8188	0.6116
	Combined	0.6681	0.6683	0.9164	0.6682
	Neighbors	0.6280	0.7515	0.8871	0.6843
HGR	Original	0.8938	0.7664	0.9274	0.8252
	Reverse	0.7929	0.8429	0.8337	0.8171
	Combined	0.8994	0.6952	0.9390	0.7843
	Neighbors	0.8818	0.7935	0.9211	0.8353
SFA	Original	0.8636	0.4214	0.9692	0.5664
	Reverse	0.8563	0.7730	0.9381	0.8125
	Combined	0.9288	0.3958	0.9894	0.5551
	Neighbors	0.9176	0.5111	0.9826	0.6565

Table 5.3: Quantitative result metrics of the proposed enhancements and Brancati *et al.* (2017). For each dataset, we have four different applications: the original hypothesis with respect to P_{Cb_s} , the reverse hypothesis with respect to P_{Cr_s} , the one which combines both, and the extension using the neighborhood approach.

has very good *F-measure* rates.

The neighborhood approach achieved the best *F-measure* in Compaq, HGR, and Pratheepan. Moreover, the other metrics still are at a very high rate for all datasets, being in the top second in almost all cases. If we compare the neighbors approach with the original, except for the *Recall* – where we only got the best result in SFA –, we can see that our implementation achieved the best measures practically for all other metrics, in the four datasets.

Therefore, the combined and neighbors approaches are very competitive compared to the original method. Furthermore, all the variations of the original method are still computed in quadratic time, maintaining the desired computational efficiency that is useful in different application domains, mainly near real-time systems (processing time of about 10ms for a typical image of dimensions 300x400).

We have also tested the subset of non-skin images from Compaq dataset in terms of *Specificity*. Basically, this measure tells us the ability of the method to correctly identify the non-skin pixels in the image, in other words, the true negative rate. It is important to remember that the original (Brancati *et al.*, 2017) method was compared with six well known rule-based methods in the literature, and it outperformed all of them in this experiment. We can see in table 5.4 that both combined and neighbors are in a better position, with a gain of about 5.7% and 2%, respectively, which shows us, once again, how robust are the results produced by these proposed enhancements.

Figures 5.7, 5.8, 5.9 and 5.10, present some qualitative results with image samples in column (a) along with the results for each method tested. Column (b) presents the respective ground truth for each image in column (a), column (c) presents the original method Brancati *et al.* (2017) results, column (d) presents the respective reverse method results, column (e), the combined method results and column (f) the extended neighborhood method.

Qualitatively, we can see that, in general, the reverse method removes a large part of the

Hypothesis	Specificity
Original (Brancati <i>et al.</i> , 2017)	0.8681
Reverse	0.7876
Combined	0.9177
Neighbors	0.8866

Table 5.4: Specificity of the proposed enhancements and original method for non-skin images of Compaq dataset. The combined method obtained the best result and neighbors is the second ranked method.

reddish pixels from the background of the image (e.g. see the third image in the Figure 5.7, first and fourth images in the Figure 5.8, second image in Figure 5.9, and third image in Figure 5.10), which the original method was not able to. On the other hand, the reverse method has not been successful in taking off yellowish-toned background regions (e.g. see the third image in Figure 5.9, and fifth image in Figure 5.10).

However, when we blend the original method along with the reverse in the method we call combined, both background regions of reddish and yellowish pixels are almost completely removed. In addition, salt-like noises are also dropped, since the rules together are more rigid (e.g. see column (e) combined method for the third image in Figure 5.9, and fifth image in Figure 5.10). Obviously, this causes an undesired effect of removing some of the skin pixels of which we are interested. This helps us understand why the recall decreases with the application of the combined rule.



Figure 5.7: Image samples with the results of each method in SFA dataset: (a) original image (b) ground truth (c) original Brancati et al. (2017) (d) reverse (e) combined (f) neighbors.

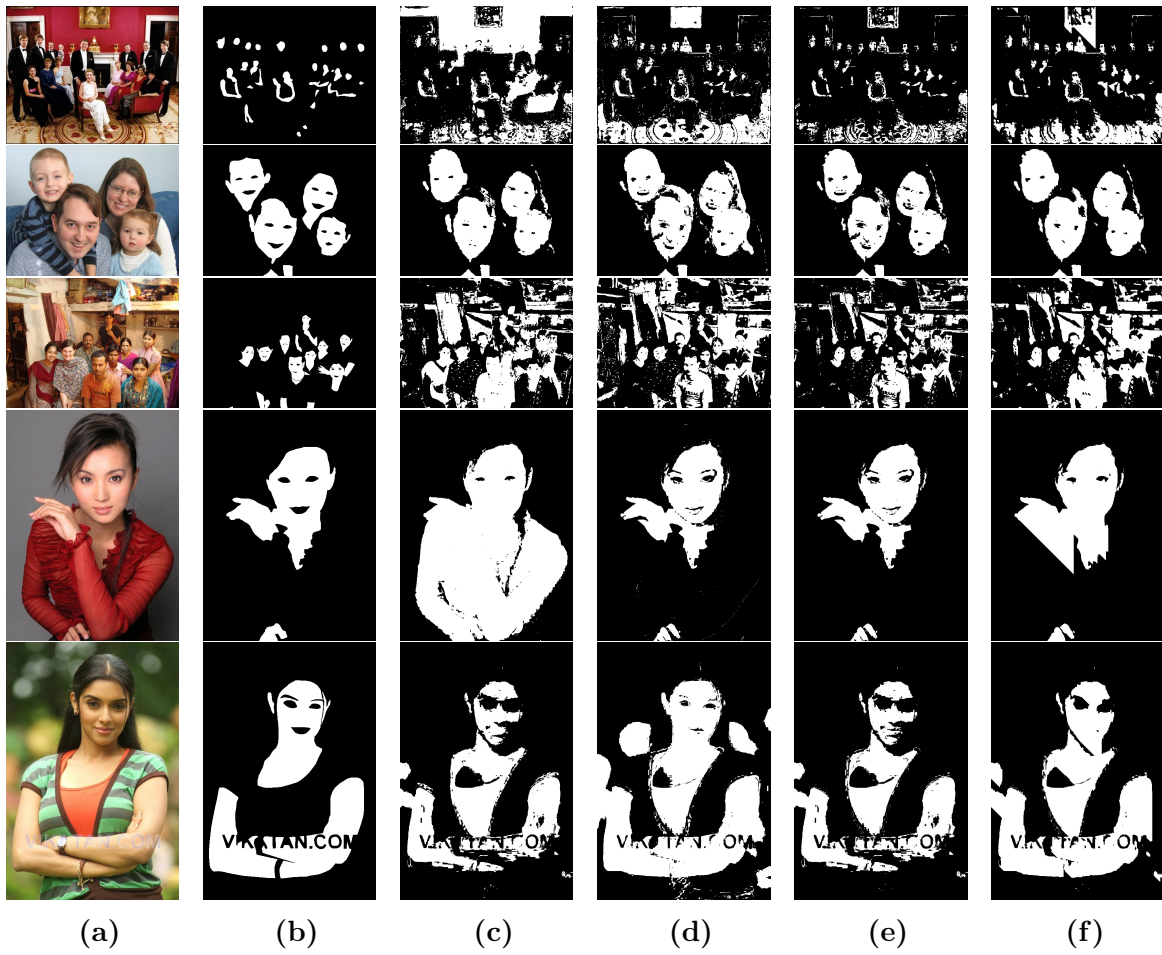


Figure 5.8: Image samples with the results of each method in Pratheepan dataset: (a) original image (b) ground truth (c) original Brancati et al. (2017) (d) reverse (e) combined (f) neighbors.

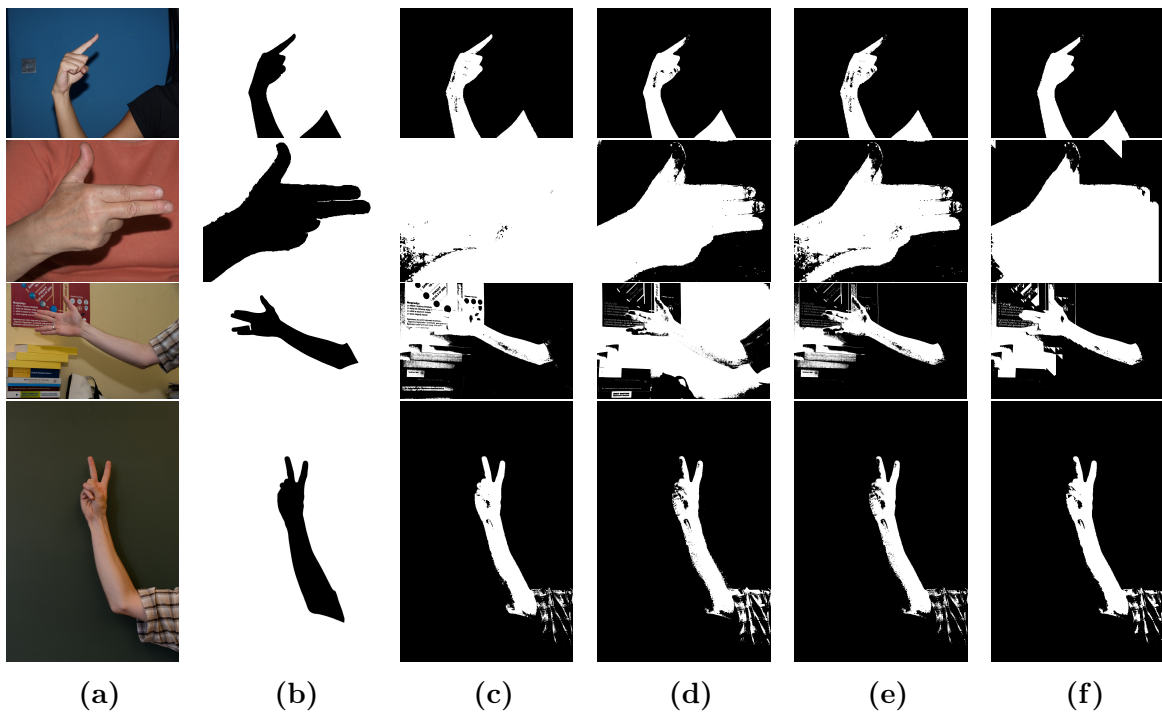


Figure 5.9: Image samples with the results of each method in HGR dataset: (a) original image (b) ground truth (c) original Brancati et al. (2017) (d) reverse (e) combined (f) neighbors.

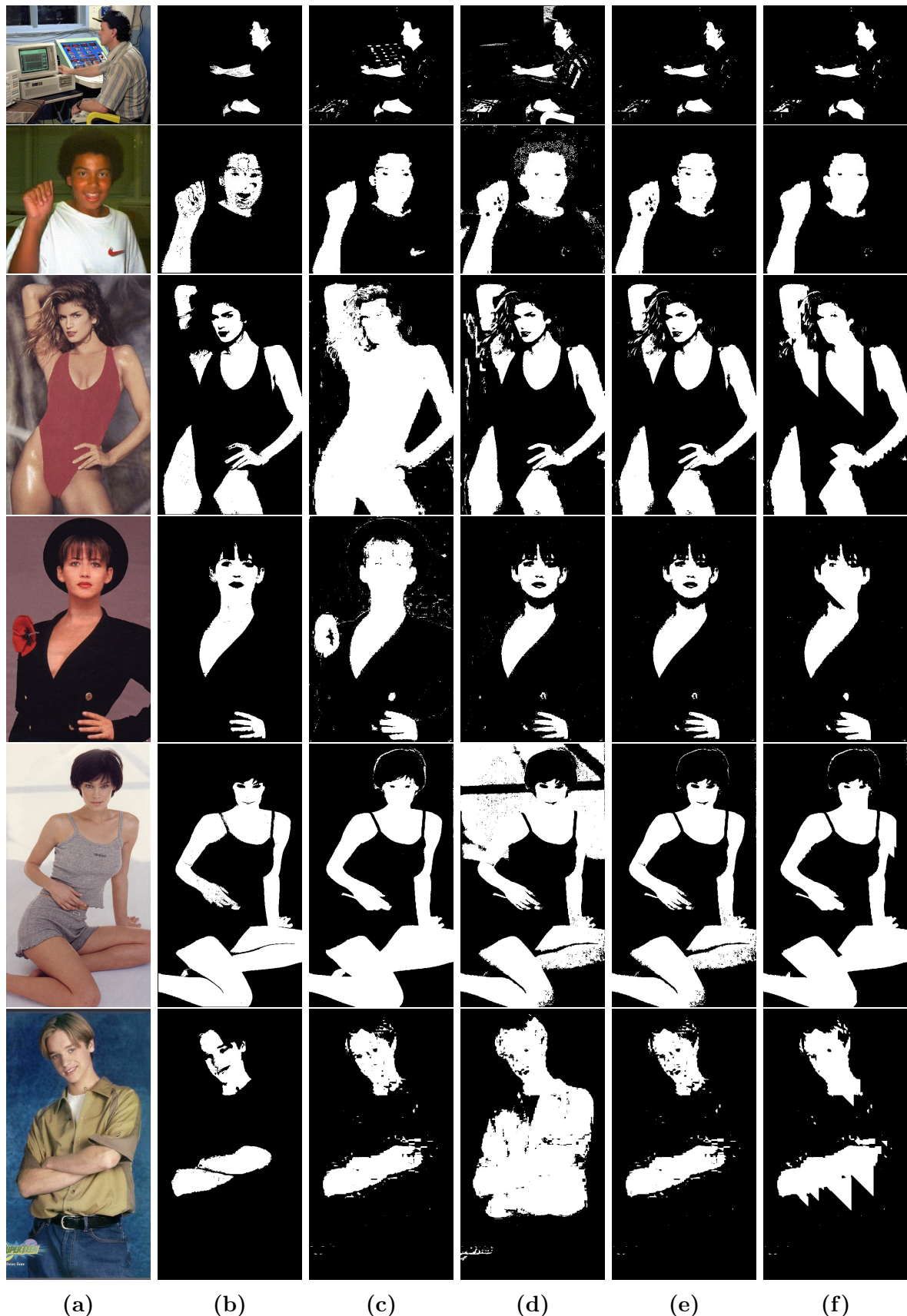


Figure 5.10: Image samples with the results of each method in Compaq dataset: (a) original image (b) ground truth (c) original Brancati et al. (2017) (d) reverse (e) combined (f) neighbors.

5.4 Supplementary neighborhood operations experiments

In this section, we will show some experimental results of the supplementary neighborhood adaptation described in section 4.4. In short, we basically scan the image, with a size of $W \times H$, in the raster order, and apply the original and reverse rules for every single pixel. We keep the result in a matrix of the same size ($W \times H$) of the input image. For each coordinate of this output matrix, we will have a two positions vector with the result of the original and reverse rules answer for this pixel. Finally, we count those answers into four different strategies. The results can be seen in table 5.5.

Dataset	Hypothesis (Neighbors)	Precision	Recall	Specificity	F-measure
Compaq	Proposed 4.3	0.4708	0.7421	0.8463	0.5761
	AND	0.5121	0.6252	0.8941	0.5630
	OR	0.3786	0.9037	0.7203	0.5336
	P_{Cr_s} only	0.4132	0.7254	0.8032	0.5265
	P_{Cb_s} only	0.4478	0.8053	0.8120	0.5755
Pratheepon	Proposed 4.3	0.6280	0.7515	0.8871	0.6843
	AND	0.6731	0.6789	0.9127	0.6760
	OR	0.4624	0.8837	0.7321	0.6072
	P_{Cr_s} only	0.5285	0.7414	0.8163	0.6171
	P_{Cb_s} only	0.5630	0.8218	0.8292	0.6682
HGR	Proposed 4.3	0.8818	0.7935	0.9211	0.8353
	AND	0.9007	0.7203	0.9378	0.8005
	OR	0.7978	0.9084	0.8238	0.8495
	P_{Cr_s} only	0.7937	0.8600	0.8331	0.8256
	P_{Cb_s} only	0.8941	0.7715	0.9288	0.8283
SFA	Proposed 4.3	0.9176	0.5111	0.9826	0.6565
	AND	0.9345	0.3947	0.9899	0.5549
	OR	0.8345	0.8181	0.9176	0.8262
	P_{Cr_s} only	0.8612	0.7922	0.9375	0.8252
	P_{Cb_s} only	0.8953	0.7690	0.9286	0.8273

Table 5.5: Quantitative result metrics of the proposed supplementary neighborhood adaptation. For each dataset, we have five different applications of the neighbors operations. The first line is the result of the proposed method detailed in section 4.3 for comparison. The following four lines are the supplementary neighborhood adaptation shown in section 4.4 which are considering, respectively, an AND between the original and reverse rules, an OR between the original and reverse rules, the P_{Cr_s} (reverse) only, and the P_{Cb_s} (original) only.

It is worth mentioning that the goal here is to explore better the connectivity of the 8-neighbors window and check, on the basis of a symmetric mask window, if the *diagonal effect* is gone as well as the measures are improved. Therefore, we are not worried about the additional computational cost is taken to scan the image one more time. Even though this implementation can be enhanced by, for instance, keeping the latest three lines of the image scanned in memory to be verified by the 8-neighbors window backward to have a final decision when evaluating a pixel.

From the table 5.5 we can see that the application of the neighborhood approach using AND gives us the best *Precision* and *Specificity* in all datasets. On the other hand, we lost performance in the *Recall* in relation to the other approaches. Speaking of *Recall*, the

loss is in the order of 20% up to 30% in the Compaq, Pratheepan and HGR datasets, and approximately 50% in the SFA.

Clearly, there is a trade-off between increasing *Precision* and decreasing *Recall* and vice versa, just as in the experiments done in section 5.3 with all methods. When we use a more relaxed rule, as in the case of the OR (or the isolated rules), we get a better *Recall*, but there is also an abrupt drop in *Precision* and *Specificity*. Another side effect of this phenomenon is to increase the false positive rate.

The AND conjunction approach is most similar to that implemented in neighborhood extended method, as we can see in the results of the first line (named Proposed 4.3) of each dataset. The results obtained by that approach (Proposed 4.3) show low variability in relation to the adaptations shown in the experiments in this section. In fact, we can see the best *F-measure* obtained by this method both in Compaq and Pratheepan, and the second in HGR. In addition, it performed the second best *Precision* and *Specificity* in Compaq, Pratheepan, and SFA while keeping solid results with respect to *Recall*.

Therefore, for the sake of implementation, the approach given by the neighborhood implementation (Proposed 4.3) may be a good starting point. Nevertheless, we can apply some other complementary technique, such as weighting the distance among the pixels, to measure those more or less relevant to the decision making in the neighborhood. This can potentially diminish the effect of this trade-off and obtain more harmonic measures. For the *diagonal effect*, we can use a more symmetric window, similar to the one used in the adaptations experimented here, to produce better results and increase this undesired anomaly.

5.5 Grid search parameters experiments

In one part of this work, we are concerned with understanding and, perhaps, improving the choice of parameters that define the trapezoids. They are a fundamental part of the model that segments the skin pixels in an image, the main role of the methods developed here. In short, as described in section 4.5, 5th and 95th percentiles of the histogram of the Y luminance component have been used by Brancati *et al.* (2017) to be the right parameters to define the trapezoids coordinates. For this reason, we decided to trigger different combinations of these parameters to figure out which pair better works for the model fitting. In addition, we would like to answer the question: why 5th and 95th percentiles have been used?

Thus, we created a simple grid search algorithm (see details in section 4.5) to find the best range combination of those parameters. Despite we do not exhaustively consider all parameter combinations, we used an efficient search strategy by sampling a given number of candidates. For each chosen parameters candidate, we dynamically used them in the combined method to test every single image of each dataset described in section 5.1. Lastly, we sort the results table using respectively, *F-measure*, *Precision*, and *Recall* metrics. The results with these metrics, in that given order, for each dataset, can be seen in Appendix A.

It is worth mentioning that the grid search algorithm starts with P_{min} percentile index in 5 and P_{max} percentile lower bound is set to P_{min} in the inner loop. Thus, we will no longer have a combination of parameters such as [15, 10], that means, we always have combinations such that $P_{max} \geq P_{min}$. This will produce a table with results according to the template given in Figure 5.11.

We performed this experiment in all four datasets: Compaq, Pratheepan, HGR, and SFA. For each dataset, respectively, we have a scatter plot of *F-measure*, *Precision*, and *Recall*, with their respective variance, which can be seen in Figures 5.12, 5.13, 5.14, and 5.15. Each

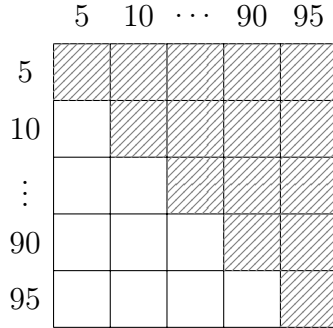


Figure 5.11: The output template table with result metrics of the grid search algorithm. P_{min} percentile index is in vertical axis and P_{max} percentile index is in horizontal axis. The highlighted cells – from the main diagonal and above – are the ones which will have values of the metrics after running the method for the given combination of parameters. Source: proposed by the author.

chart is showing the resulting metrics, in y (vertical) axis², by using a fixed P_{min} and varying P_{max} along x (horizontal) axis. The shaded path of the measures are the variance and tell us how far we are from the mean when looking for each image within the dataset individually.

We can see predominantly that larger intervals – e.g. [5, 85], [5, 90], [5, 95] – resulted in the best *Precision* in all datasets. On the other hand, smaller intervals, with both P_{min} and P_{max} near the upper bound (95) – e.g. [80, 90], [85, 95], [90, 95] –, performed better in *Recall*. Thus, if we set up a specific pair of parameters for the percentile to compute the trapezoid coordinates, it can produce a good *Precision* but it may hurt the *Recall* and vice versa.

Therefore, evaluate *F-measure* in this situation seems to be the correct path, since it gives us a harmonic measure between *Precision* and *Recall*. That's why we sorted the results (see Tables A.1, A.2, A.3, and A.4 for details) using the order *F-measure*, *Precision*, and *Recall* as a criteria. Another important observation is the behavior of variance in each result, that means, even good measures with huge variance could be a problem for real world applications.

In Compaq, we can see that top *F-measure* results were obtained with pair of parameters such as [5, 25], ..., [5, 95], while keeping good measures in both *Precision* and *Recall*. A similar behavior can be seen in Pratheepan, but among the highest *F-measure* scores are those where $P_{min} = 10$. Next are those starting with $P_{min} = 5$. So, we could state that the values [5, 95] chosen by Brancati *et al.* (2017) are fair enough since the results were quite good. Even so, the results are insignificantly worse than the highest ranked ones (see Table 5.6).

However, in HGR as well as in SFA top *F-measure* results were obtained with pair of parameters such that $P_{min} = P_{max}$. For instance, we can see in HGR results that *Recall* = 0.8641 and *F-measure* = 0.8667 when $P_{min} = 5$ and $P_{max} = 5$, while [5, 95] interval resulted in *Recall* = 0.6952 and *F-measure* = 0.7843 – a gain in the order of 24% and 10% for each metric, respectively. A similar behavior can be seen in the results of SFA, where the gain in *Recall* and *F-measure* are in the order of 67% and 39% for each metric, respectively, which is a very huge difference. It is worth mentioning that, despite *Precision* and *Specificity* have a slightly decreasing, they are still around the Brancati *et al.* (2017) results.

On the basis of this scenario, we observed that when we have $P_{min} = P_{max}$, the resulting metric is absolute the same for any combination of equal percentile parameters. For instance, in Compaq dataset, when we tried $P_{min} = 5$ and $P_{max} = 5$, we got *Precision* = 0.4172, *Recall* = 0.7333, *Specificity* = 0.8096, and *F-measure* = 0.5318. The result is the same for $P_{min} = 10$ and $P_{max} = 10$ onward up to $P_{min} = 95$ and $P_{max} = 95$. This behavior will repeat for every

²We set the range in the charts to start at 0.25 for better visualization of the series.

Dataset	P_{min}	P_{max}	Precision	Recall	Specificity	F-measure
Compaq	5	95	0.4906	0.6251	0.8856	0.5498
	5	25	0.4819	0.6459	0.8762	0.5520
	5	35	0.4866	0.6374	0.8808	0.5519
	5	40	0.4877	0.6356	0.8818	0.5519
	5	30	0.4844	0.6408	0.8789	0.5517
	5	45	0.4884	0.6335	0.8827	0.5516
Pratheepan	5	95	0.6681	0.6683	0.9164	0.6682
	10	55	0.6560	0.6955	0.9055	0.6752
	10	80	0.6558	0.6950	0.9056	0.6748
	10	85	0.6557	0.6949	0.9056	0.6748
	10	95	0.6557	0.6950	0.9057	0.6747
	10	90	0.6556	0.6950	0.9056	0.6747
HGR	5	95	0.8994	0.6952	0.9390	0.7843
	5	5	0.8693	0.8641	0.9064	0.8667
	10	10	0.8693	0.8641	0.9064	0.8667
	15	15	0.8693	0.8641	0.9064	0.8667
	20	20	0.8693	0.8641	0.9064	0.8667
	25	25	0.8693	0.8641	0.9064	0.8667
SFA	5	95	0.9288	0.3958	0.9894	0.5551
	5	5	0.9313	0.6617	0.9785	0.7737
	10	10	0.9313	0.6617	0.9785	0.7737
	15	15	0.9313	0.6617	0.9785	0.7737
	20	20	0.9313	0.6617	0.9785	0.7737
	25	25	0.9313	0.6617	0.9785	0.7737

Table 5.6: Quantitative result metrics of the proposed grid search parameters tuning. For each dataset, we have different applications of the combined method with different pairs of P_{min} and P_{max} percentiles. The first line is the default one [5, 95], as reported in the experiments given in Table 5.3. Next five lines are the top five results ordered by F-measure, Precision, and Recall, respectively.

single dataset tested.

Based on this result, we started to investigate the source code given in the original method by Brancati *et al.* (2017). We found out that, when the percentiles are the same, the computation of the parameters who define the trapezoids is impacted. In other words, $Y_0, Y_1, Y_2, Y_3, Y_{min}, Y_{max}, Cr_{min}, Cb_{max}$ are always the same, i.e. assume default values. Even Cb_{min}, Cr_{max} , that are still computed dynamically by the internal method functions, do not change when P_{min}, P_{max} percentiles are changed since they are dependent on the previous parameters and the histogram of the image itself that never change. The same behavior will be observed when $P_{min} > P_{max}$.

It is important to note that, in the case of Compaq and Pratheepan, where $P_{min} = P_{max}$, the results worsen significantly in terms of *Precision*. On the other hand, they have a significant gain in the HGR and SFA datasets.

This particular phenomenon occurs due to the nature of the images that form each of these images databases. Both Compaq and Pratheepan contain images with more complex scenes, uncontrolled environment, distinct lighting conditions and, in general, images randomly collected from the internet. On the other hand, HGR and SFA contain images where we have a great concentration of skin pixels – hands and arms in the case of HGR, and faces in the case of SFA occupying a considerable region of the image. Furthermore, a large part

of them was collected in controlled environments, on the background and lighting conditions point of view.

Therefore, this behavior must be taken into consideration when selecting a pair of P_{min} and P_{max} to apply in the method in turn, since this can be decisive for a potential performance improvement.

With respect to the variance for all the metrics, we can observe that, regardless of the combination of P_{min} and P_{max} parameters, there is no great deviation in the results in relation to the mean. For all datasets, the combinations where P_{min} and P_{max} are closer to the upper bound (95) – e.g. [80, 90], [85, 90], [85, 95], [90, 95] – are the ones with the highest variance. On the other hand, the variance had little fluctuation where $P_{min} = P_{max}$.

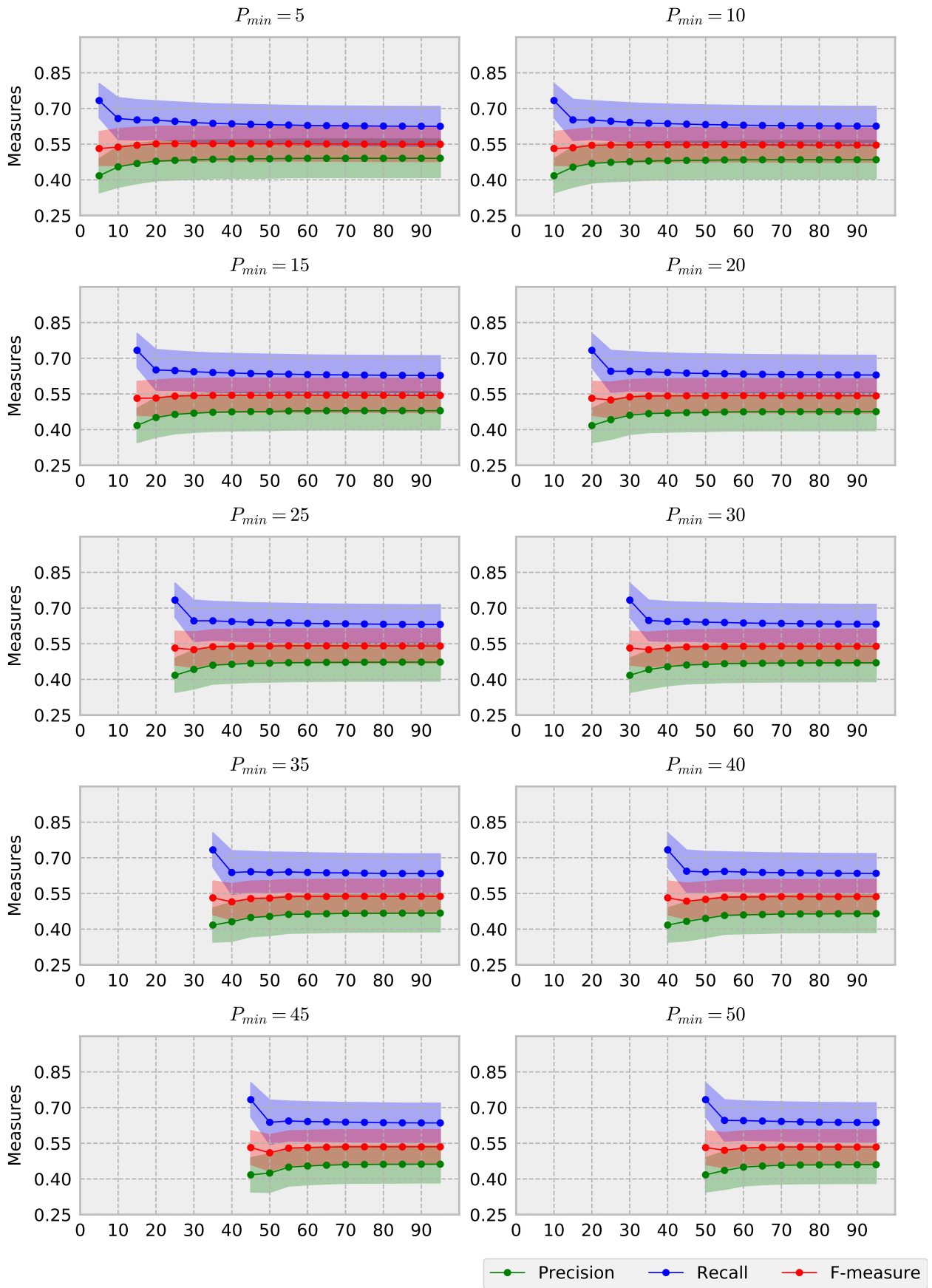


Figure 5.12: Scatter plot with the quality measures for grid search parameters in Compaq dataset.

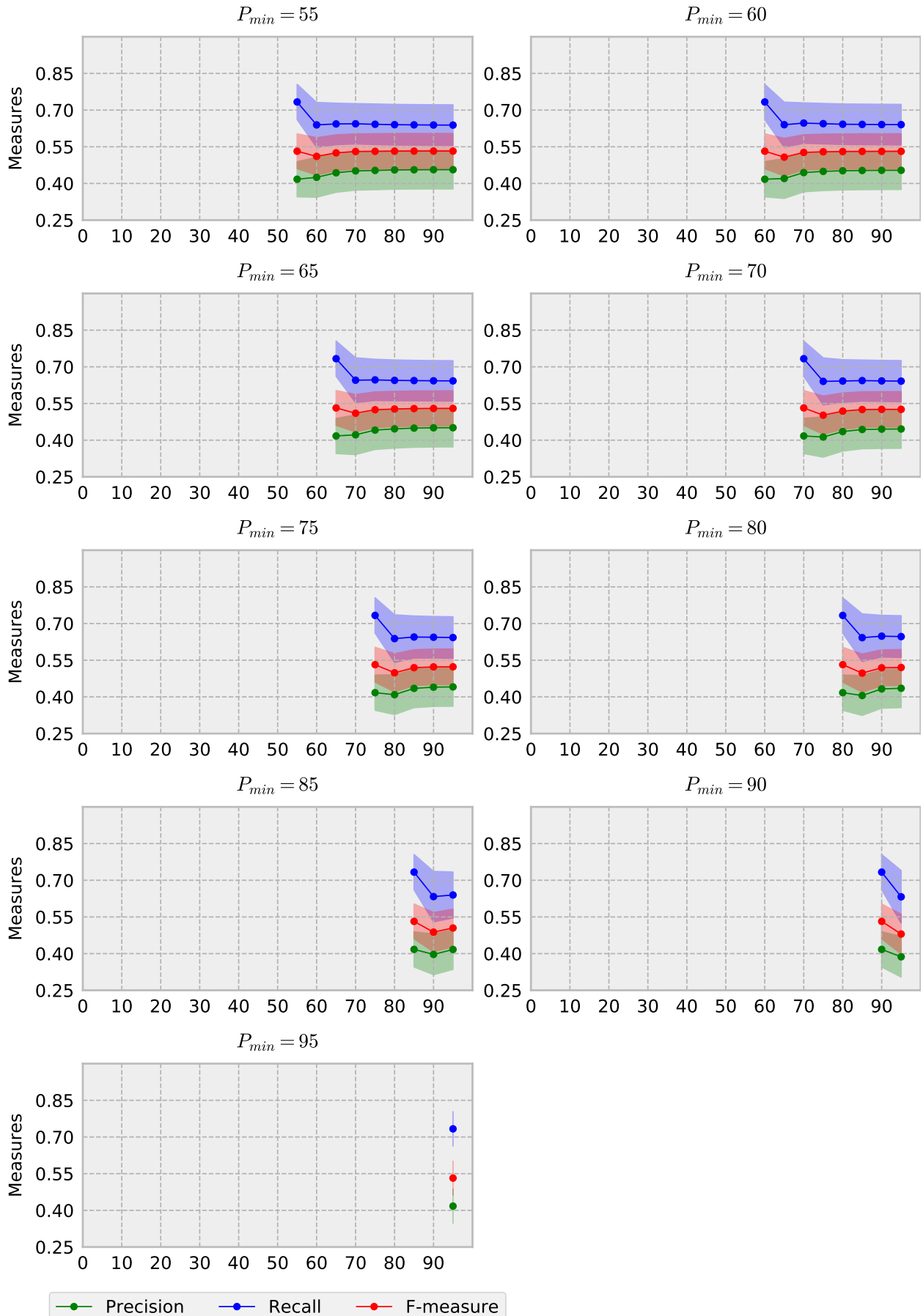


Figure 5.12: Scatter plot with the quality measures for grid search parameters in Compaq dataset (cont.).

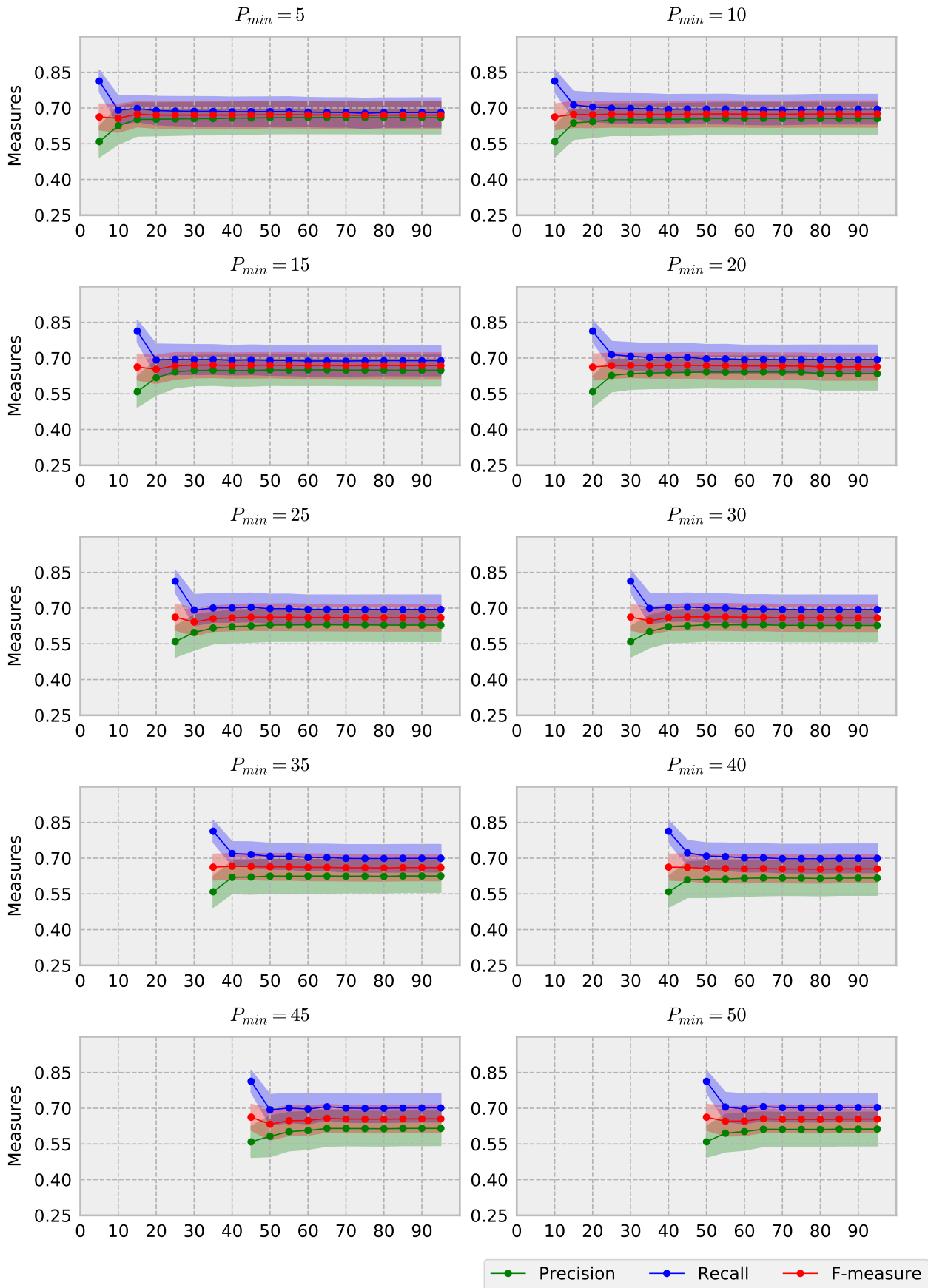


Figure 5.13: Scatter plot with the quality measures for grid search parameters in Pratheepan dataset.

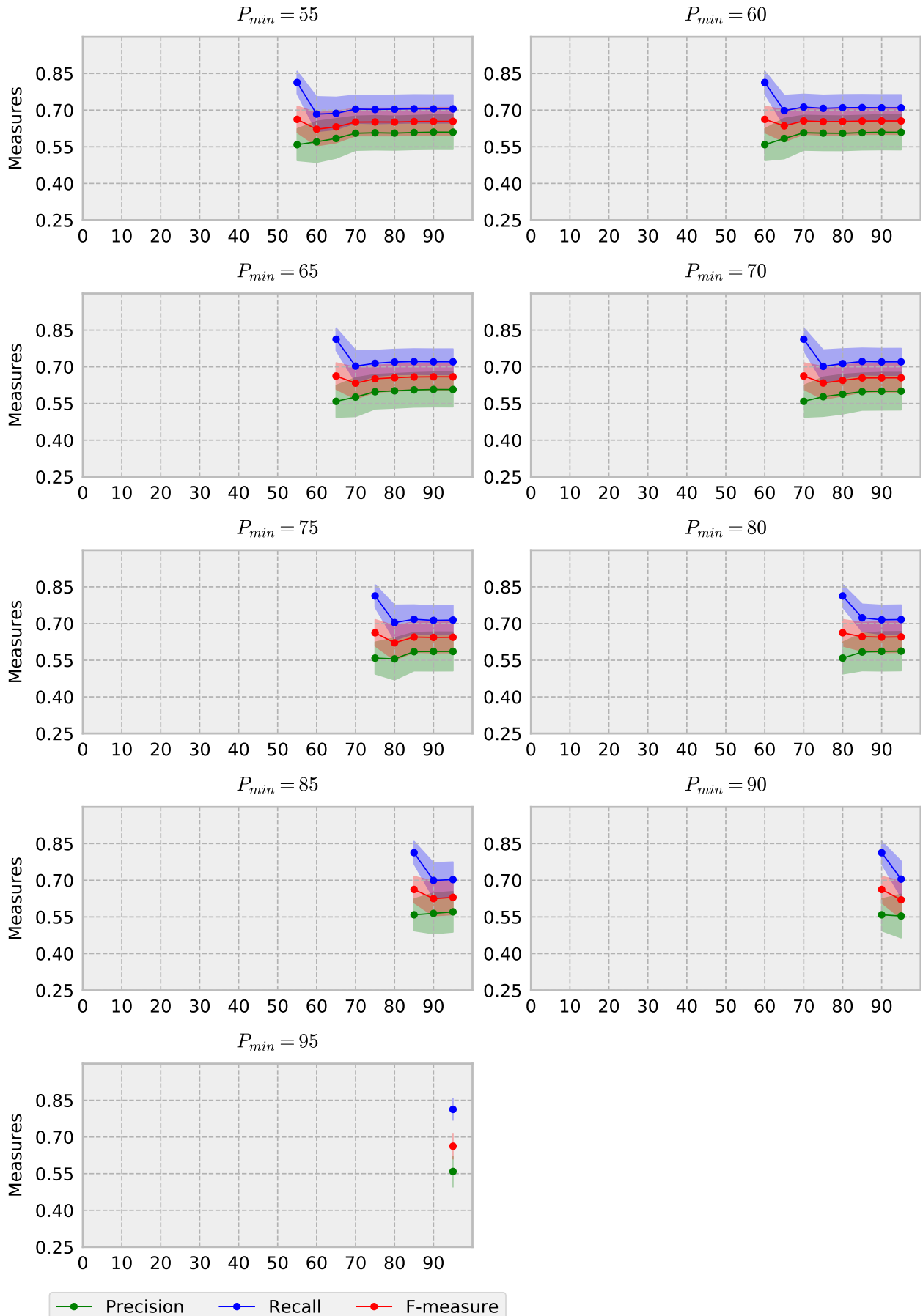


Figure 5.13: Scatter plot with the quality measures for grid search parameters in Pratheepan dataset (cont.).

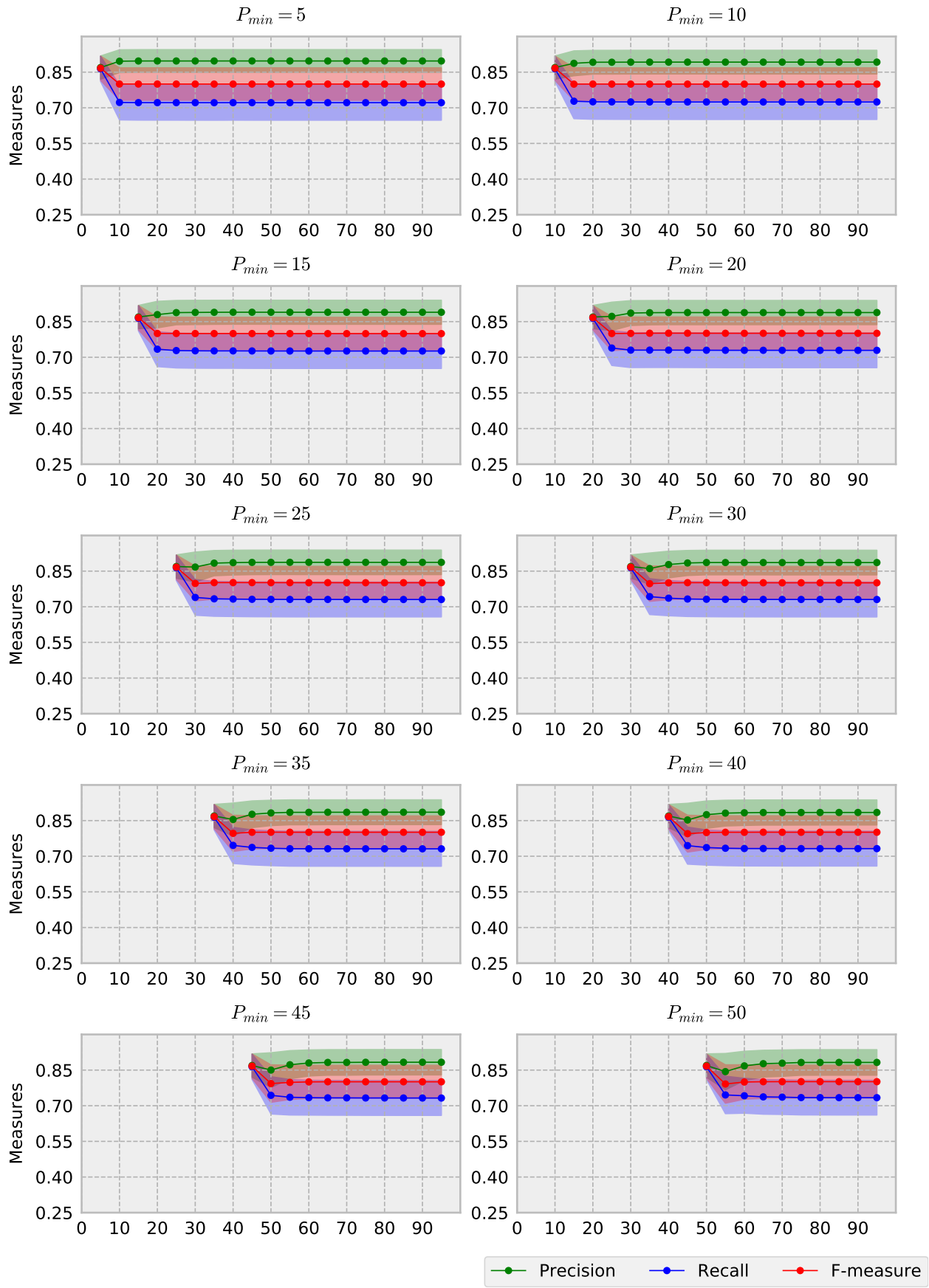


Figure 5.14: Scatter plot with the quality measures for grid search parameters in HGR dataset.

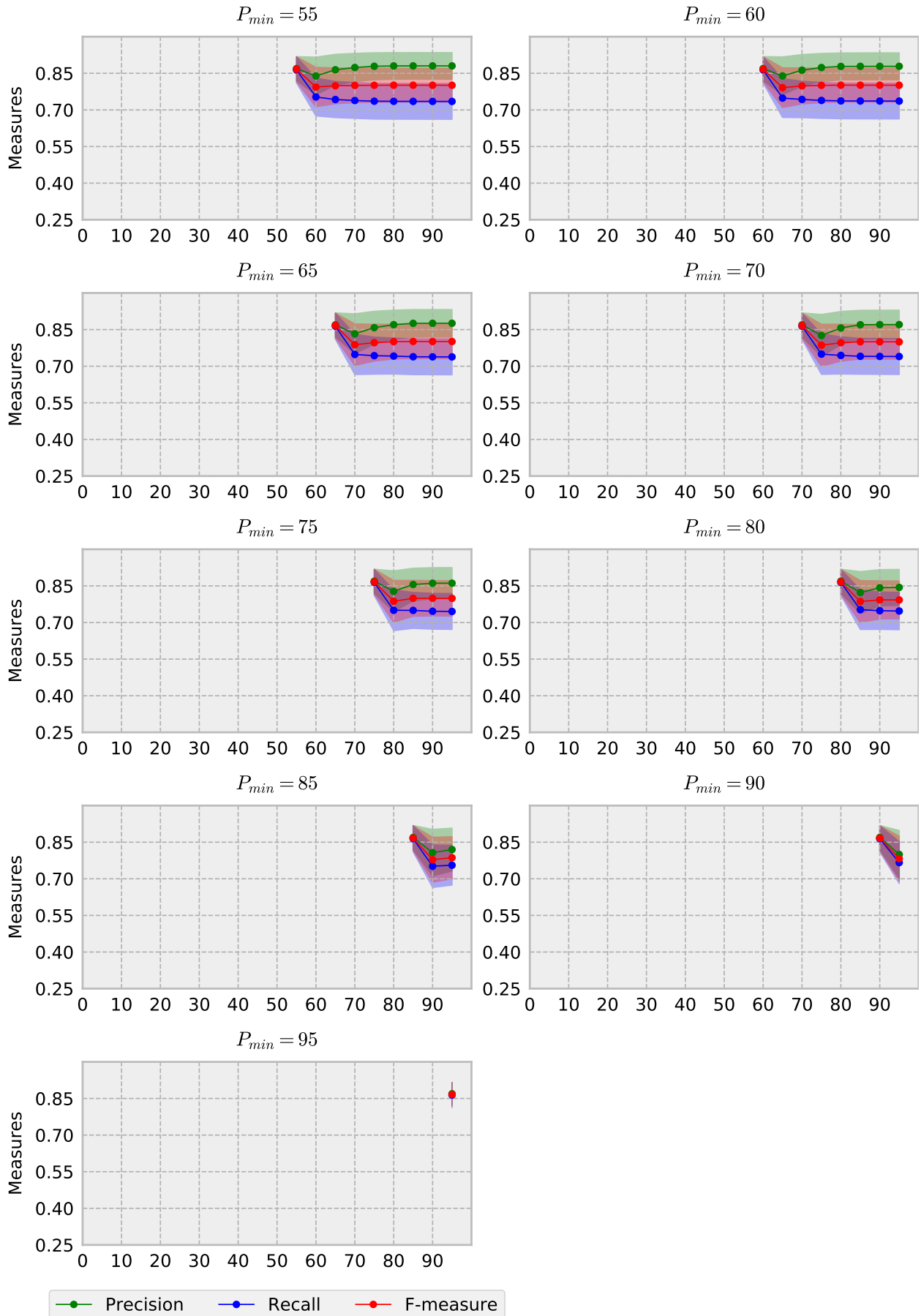


Figure 5.14: Scatter plot with the quality measures for grid search parameters in HGR dataset (cont.).

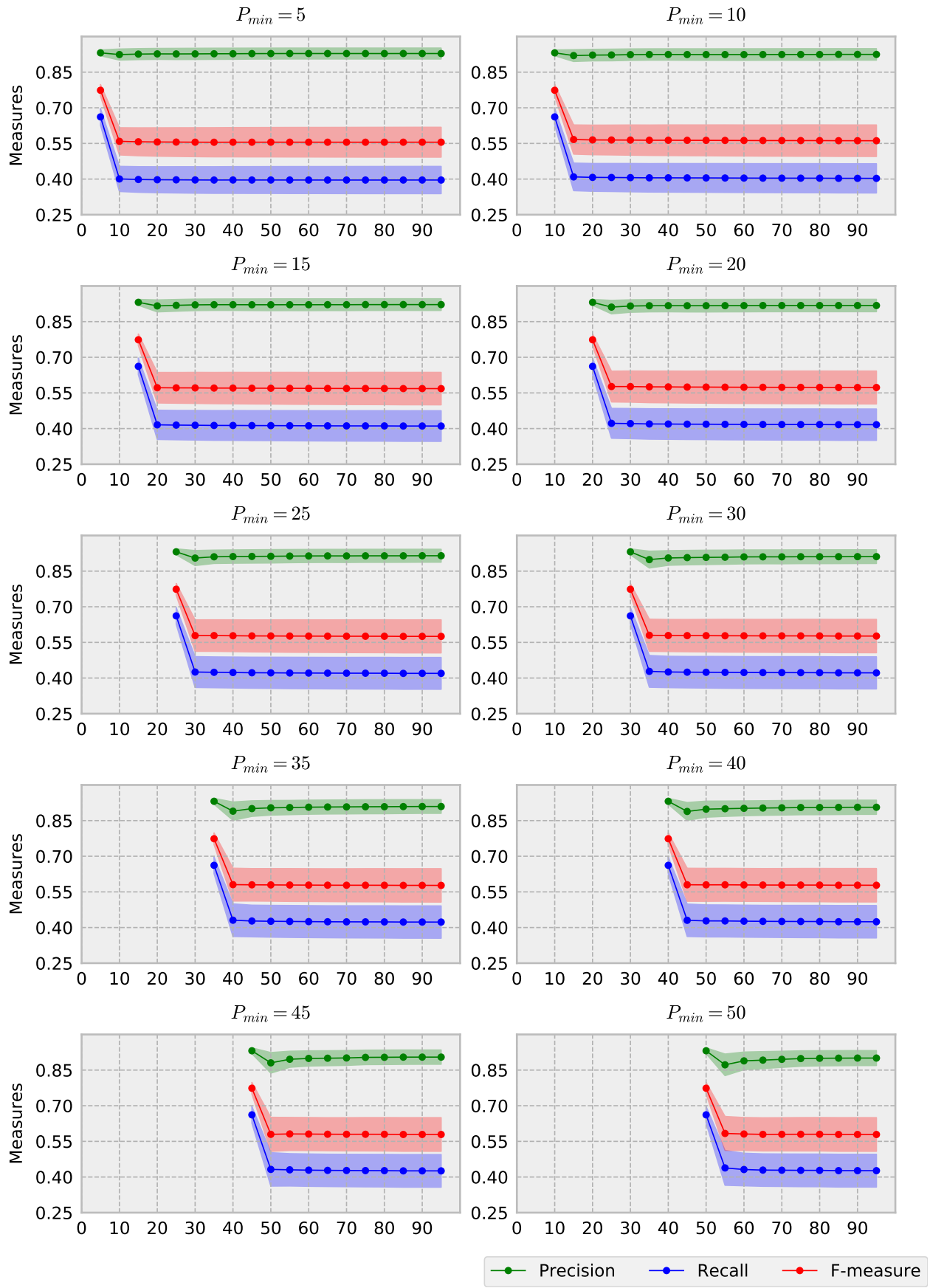


Figure 5.15: Scatter plot with the quality measures for grid search parameters in SFA dataset.

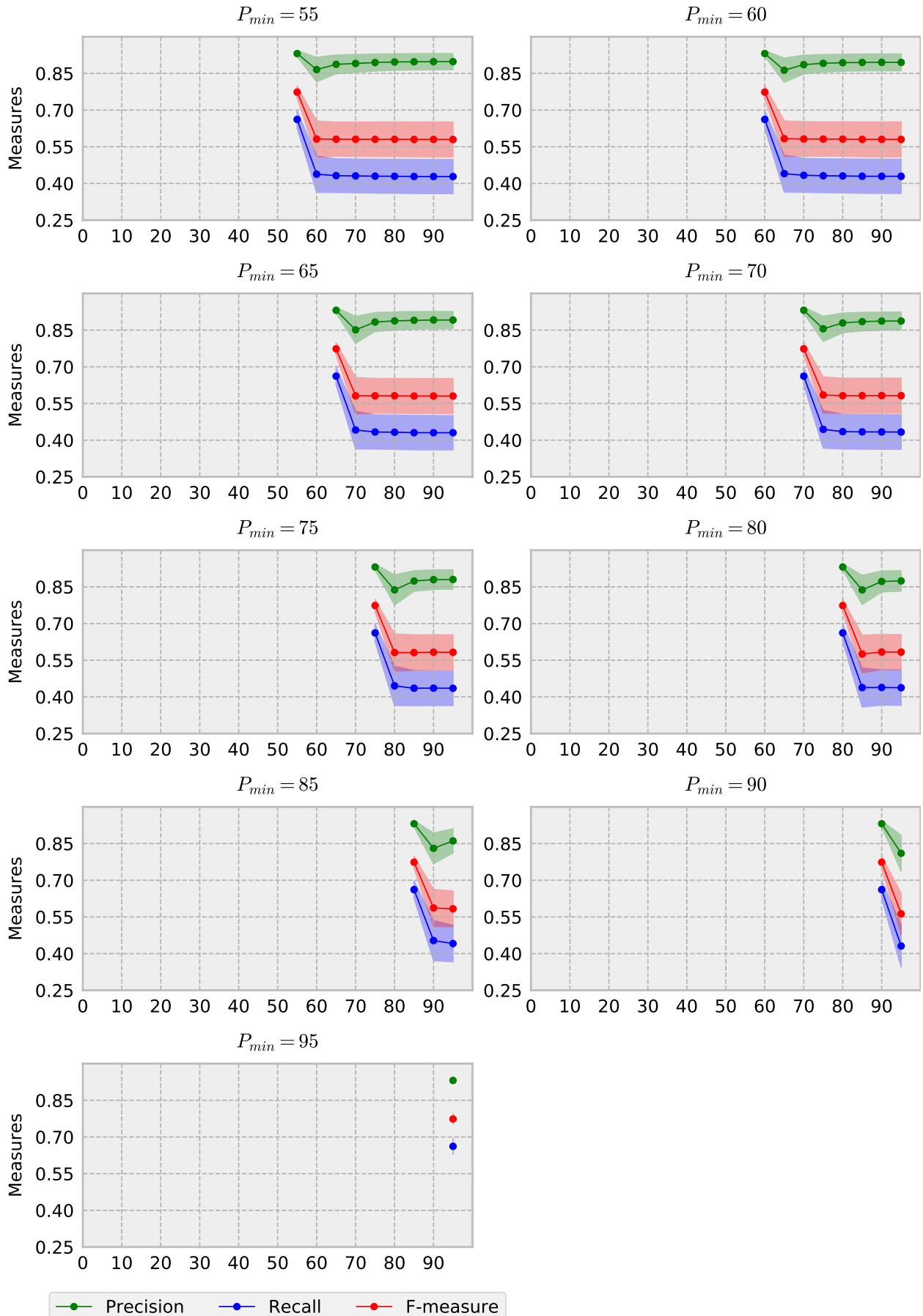


Figure 5.15: Scatter plot with the quality measures for grid search parameters in SFA dataset (cont.).

Chapter 6

Conclusions

We started this thesis by describing the problem of skin detection, explaining our motivation and determining our main objectives. Further, we reviewed the literature on skin detection, comparing techniques and classifiers, mainly from the point of view of performance, color models, skin color modeling, and datasets. Next, we stated the theoretical concepts that apply to this research where we briefly showed some techniques from image processing and computer vision fields used during the project, such as color space transformation, human skin segmentation, and understanding, etc. Then, we reviewed the method proposed by [Brancati et al. \(2017\)](#) and we extended it adding new variations. Also, we implemented a grid search strategy to find the best combination of parameters to the method. Finally, we presented some experimental evaluations of the proposed extensions along with the original method in four widely known datasets: SFA, Pratheepan, HGR, and Compaq.

This chapter address some conclusions regarding our research, objectives, and contributions. Finally, in Section [6.2](#), we present some possible future work.

6.1 Final considerations

The method proposed by [Brancati et al. \(2017\)](#) is a novel rule-based skin detection method that works in the YCbCr color space based on correlation rules that evaluate the combinations of chrominance Cb, Cr values to identify human skin pixels depending on the shape and size of dynamically generated skin color clusters (trapezoids). The method is surprisingly simple and clever and it established a new tier.

Because the authors left the code available, we reproduced the original experiments and also checked if the same color patterns were presented in RGB, HSV, and Lab color spaces, or other applications as finding tree leaves, but the results were not consistent as the original approach for human skin using YCbCr space.

As a contribution of this work we introduced two extensions based on a hypothesis that the original rule could be reversed and also taking into consideration that a human skin pixel does not appear isolated. We also made a third extension that combines the original rule with the reversed one in a more strengthen method in terms of precision. All these extensions are simple and do not hurt the efficiency of the original method.

We tested the extensions in four standard public datasets and the experiments showed that our extensions improve the accuracy of skin detection, even when there exists a huge variation in ethnicity and illumination. Moreover, our approach proved to be very competitive, outperforming alternative state-of-the-art work. In addition, we implemented a grid search for the parameters tuning and the supplementary neighborhood operations as well as new tools to process the datasets, binarize images, and a visualization web application for

the problem of skin detection¹.

Our results confirm that skin color is an extremely powerful cue for detecting human skin in unconstrained imagery. Other local properties can be experimented to be used in a future work, along with the methods presented here, such as texture, shape, geometry, and other neighborhood operations.

Finally, part of the work has been published in an international conference (VISAPP) in earlier 2018.

6.2 Future work

In the future, extended works could explore further the connectivity of the skin pixels and, because there is so far no explanation why the original method works so well, it would be valuable to statistically analyze the shape of the trapezoids on the YCbCr space and try to correlate with the classification accuracy.

Our intuition, based on the experimental results, says that trapezoids features such as size, area, symmetry, and others, could be used to establish a relationship with the classification accuracy. Moreover, the shape of the trapezoids could be previously processed, for instance by filtering image illumination, to obtain better classification results.

The neighborhood operations add some additional computational cost but the implementation can be enhanced as well as other techniques applied, such as applying weights when counting neighboring pixels.

The implemented grid search algorithm to understand the parameters selection in Section 5.5 can be improved and we could try to learn the best parameters of the trapezoids by means of Machine Learning techniques.

A recent test paper comparing different color spaces Chaves-González *et al.* (2010) suggests that YCgCr is also a good candidate for this problem. In fact, YCbCr and YCgCr color spaces are very similar. Therefore, the same color relations can be presented in this space.

¹ Available at <https://bitbucket.org/rodrigoadfaria/skin-detector-ws>.

Appendix A

Trapezoids Parameters Tuning Results

In this appendix we present the results of the grid search algorithm applied on each of the four datasets described in section 5.1. We only applied the combined rules method, once the trapezoids parameters definition do not change among the different methods, as described in chapter 4. Every table is sorted by *F-measure*, *Precision* and *Recall*, respectively. The results are presented in Tables A.1, A.2 A.3, and A.4 for Compaq, Pratheepan, HGR, and SFA, respectively.

Table A.1: Trapezoids parameters tuning results for Compaq dataset and combined rules.

Pmin	Pmax	Precision	Recall	Specificity	F-measure
5	25	0.4819	0.6459	0.8762	0.5520
5	35	0.4866	0.6374	0.8808	0.5519
5	40	0.4877	0.6356	0.8818	0.5519
5	30	0.4844	0.6408	0.8789	0.5517
5	45	0.4884	0.6335	0.8827	0.5516
5	20	0.4784	0.6508	0.8729	0.5514
5	55	0.4901	0.6303	0.8843	0.5514
5	50	0.4887	0.6318	0.8832	0.5511
5	60	0.4904	0.6288	0.8848	0.5511
5	65	0.4906	0.6279	0.8852	0.5509
5	70	0.4908	0.6272	0.8854	0.5507
5	75	0.4907	0.6266	0.8855	0.5504
5	80	0.4907	0.6261	0.8856	0.5502
5	85	0.4907	0.6256	0.8857	0.5500
5	90	0.4908	0.6253	0.8858	0.5500
5	95	0.4908	0.6251	0.8858	0.5499
10	55	0.4838	0.6313	0.8808	0.5478
10	40	0.4806	0.6364	0.8777	0.5477
10	35	0.4794	0.6382	0.8768	0.5475
10	45	0.4817	0.6341	0.8788	0.5475
10	60	0.4842	0.6297	0.8813	0.5474
10	65	0.4844	0.6287	0.8816	0.5472
10	50	0.4822	0.6324	0.8794	0.5472
10	70	0.4846	0.6281	0.8818	0.5471
10	30	0.4767	0.6414	0.8746	0.5469
10	25	0.4738	0.6465	0.8715	0.5468
10	75	0.4845	0.6274	0.8819	0.5468
10	80	0.4845	0.6269	0.8820	0.5466
10	85	0.4845	0.6263	0.8821	0.5464

Continued on next page

Table A.1 – continued from previous page

Pmin	Pmax	Precision	Recall	Specificity	F-measure
10	90	0.4846	0.6260	0.8822	0.5463
10	95	0.4846	0.6258	0.8823	0.5462
5	15	0.4688	0.6520	0.8683	0.5455
10	20	0.4689	0.6515	0.8675	0.5453
15	55	0.4784	0.6331	0.8773	0.5450
15	60	0.4789	0.6315	0.8779	0.5447
15	65	0.4793	0.6305	0.8784	0.5446
15	70	0.4795	0.6300	0.8786	0.5446
15	45	0.4761	0.6358	0.8752	0.5445
15	40	0.4747	0.6382	0.8740	0.5444
15	75	0.4794	0.6293	0.8787	0.5442
15	50	0.4766	0.6339	0.8759	0.5441
15	80	0.4796	0.6287	0.8789	0.5441
15	35	0.4730	0.6401	0.8728	0.5440
15	85	0.4795	0.6281	0.8790	0.5439
15	90	0.4797	0.6279	0.8792	0.5438
15	95	0.4796	0.6277	0.8792	0.5437
20	55	0.4742	0.6352	0.8747	0.5430
20	60	0.4748	0.6336	0.8755	0.5429
20	65	0.4753	0.6326	0.8759	0.5428
15	30	0.4692	0.6434	0.8701	0.5427
20	70	0.4755	0.6320	0.8761	0.5427
20	75	0.4755	0.6312	0.8764	0.5424
20	80	0.4756	0.6306	0.8766	0.5423
20	45	0.4714	0.6375	0.8725	0.5420
20	90	0.4758	0.6297	0.8769	0.5420
20	85	0.4757	0.6299	0.8768	0.5420
20	50	0.4722	0.6360	0.8732	0.5420
20	95	0.4757	0.6296	0.8769	0.5419
20	40	0.4696	0.6401	0.8710	0.5418
20	35	0.4674	0.6428	0.8690	0.5412
25	55	0.4702	0.6374	0.8719	0.5412
25	70	0.4720	0.6337	0.8736	0.5410
25	65	0.4716	0.6343	0.8734	0.5410
25	60	0.4709	0.6355	0.8728	0.5410
25	75	0.4722	0.6328	0.8740	0.5408
15	25	0.4639	0.6482	0.8647	0.5408
25	80	0.4724	0.6319	0.8742	0.5407
25	85	0.4726	0.6312	0.8744	0.5405
25	90	0.4727	0.6310	0.8746	0.5405
25	95	0.4726	0.6309	0.8746	0.5404
25	45	0.4672	0.6403	0.8695	0.5402
25	50	0.4681	0.6385	0.8703	0.5402
30	70	0.4687	0.6353	0.8714	0.5395
30	75	0.4690	0.6343	0.8719	0.5393
30	80	0.4694	0.6333	0.8722	0.5391
30	90	0.4698	0.6325	0.8726	0.5391
30	65	0.4679	0.6359	0.8711	0.5391
30	95	0.4698	0.6323	0.8726	0.5391
30	85	0.4695	0.6327	0.8724	0.5390
30	60	0.4670	0.6373	0.8704	0.5390
30	55	0.4659	0.6390	0.8693	0.5389
25	40	0.4635	0.6431	0.8662	0.5387
35	70	0.4663	0.6365	0.8697	0.5383
35	75	0.4667	0.6355	0.8702	0.5382

Continued on next page

Table A.1 – continued from previous page

Pmin	Pmax	Precision	Recall	Specificity	F-measure
35	90	0.4675	0.6337	0.8709	0.5380
35	95	0.4675	0.6336	0.8709	0.5380
35	85	0.4672	0.6339	0.8707	0.5379
35	80	0.4669	0.6344	0.8705	0.5379
5	10	0.4547	0.6577	0.8579	0.5377
20	30	0.4605	0.6455	0.8644	0.5375
25	35	0.4598	0.6463	0.8630	0.5373
35	65	0.4646	0.6370	0.8689	0.5373
30	50	0.4627	0.6404	0.8668	0.5372
35	60	0.4635	0.6385	0.8680	0.5371
40	70	0.4637	0.6376	0.8681	0.5369
40	75	0.4641	0.6366	0.8686	0.5368
35	55	0.4620	0.6405	0.8665	0.5368
40	90	0.4650	0.6347	0.8695	0.5367
40	95	0.4650	0.6346	0.8695	0.5367
40	85	0.4647	0.6349	0.8693	0.5367
40	80	0.4644	0.6355	0.8691	0.5366
30	45	0.4605	0.6426	0.8653	0.5365
40	65	0.4616	0.6385	0.8671	0.5358
40	60	0.4600	0.6402	0.8659	0.5354
45	75	0.4609	0.6378	0.8663	0.5351
45	90	0.4620	0.6356	0.8675	0.5351
45	80	0.4615	0.6365	0.8670	0.5350
45	95	0.4620	0.6354	0.8676	0.5350
45	85	0.4617	0.6359	0.8673	0.5350
45	70	0.4602	0.6388	0.8656	0.5350
10	15	0.4534	0.6521	0.8575	0.5349
40	55	0.4576	0.6426	0.8639	0.5346
50	75	0.4585	0.6400	0.8646	0.5343
50	85	0.4596	0.6379	0.8657	0.5342
50	80	0.4592	0.6386	0.8653	0.5342
50	90	0.4598	0.6373	0.8660	0.5342
50	95	0.4599	0.6371	0.8661	0.5342
50	70	0.4574	0.6417	0.8634	0.5341
45	65	0.4576	0.6401	0.8641	0.5337
15	20	0.4509	0.6509	0.8541	0.5327
50	65	0.4543	0.6434	0.8614	0.5326
55	90	0.4562	0.6390	0.8635	0.5324
55	85	0.4559	0.6396	0.8631	0.5323
55	95	0.4563	0.6387	0.8636	0.5323
55	80	0.4552	0.6403	0.8627	0.5321
45	60	0.4544	0.6414	0.8622	0.5320
30	40	0.4533	0.6436	0.8604	0.5319
5	5	0.4172	0.7333	0.8096	0.5318
10	10	0.4172	0.7333	0.8096	0.5318
15	15	0.4172	0.7333	0.8096	0.5318
20	20	0.4172	0.7333	0.8096	0.5318
25	25	0.4172	0.7333	0.8096	0.5318
30	30	0.4172	0.7333	0.8096	0.5318
35	35	0.4172	0.7333	0.8096	0.5318
40	40	0.4172	0.7333	0.8096	0.5318
45	45	0.4172	0.7333	0.8096	0.5318
50	50	0.4172	0.7333	0.8096	0.5318
55	55	0.4172	0.7333	0.8096	0.5318
60	60	0.4172	0.7333	0.8096	0.5318

Continued on next page

Table A.1 – continued from previous page

Pmin	Pmax	Precision	Recall	Specificity	F-measure
65	65	0.4172	0.7333	0.8096	0.5318
70	70	0.4172	0.7333	0.8096	0.5318
75	75	0.4172	0.7333	0.8096	0.5318
80	80	0.4172	0.7333	0.8096	0.5318
85	85	0.4172	0.7333	0.8096	0.5318
90	90	0.4172	0.7333	0.8096	0.5318
95	95	0.4172	0.7333	0.8096	0.5318
55	75	0.4532	0.6420	0.8608	0.5313
60	90	0.4536	0.6409	0.8611	0.5312
60	95	0.4537	0.6406	0.8612	0.5312
60	85	0.4530	0.6415	0.8606	0.5310
55	70	0.4513	0.6440	0.8592	0.5307
60	80	0.4519	0.6422	0.8597	0.5305
35	50	0.4536	0.6385	0.8616	0.5304
50	60	0.4496	0.6453	0.8582	0.5299
65	95	0.4509	0.6424	0.8593	0.5299
65	90	0.4506	0.6428	0.8590	0.5298
60	75	0.4494	0.6445	0.8572	0.5295
65	85	0.4494	0.6437	0.8582	0.5293
45	55	0.4494	0.6436	0.8582	0.5293
35	45	0.4492	0.6414	0.8575	0.5284
65	80	0.4463	0.6446	0.8550	0.5274
60	70	0.4444	0.6469	0.8528	0.5269
70	95	0.4457	0.6415	0.8567	0.5260
70	90	0.4451	0.6423	0.8560	0.5258
70	85	0.4437	0.6437	0.8546	0.5253
55	65	0.4436	0.6435	0.8533	0.5252
40	50	0.4450	0.6403	0.8554	0.5251
30	35	0.4413	0.6477	0.8494	0.5249
25	30	0.4419	0.6462	0.8490	0.5248
20	25	0.4418	0.6453	0.8515	0.5245
65	75	0.4412	0.6465	0.8499	0.5245
75	95	0.4409	0.6427	0.8528	0.5230
75	90	0.4398	0.6440	0.8519	0.5226
50	55	0.4357	0.6461	0.8459	0.5205
80	95	0.4352	0.6467	0.8451	0.5203
75	85	0.4348	0.6449	0.8486	0.5194
80	90	0.4327	0.6483	0.8433	0.5190
70	80	0.4352	0.6418	0.8486	0.5187
40	45	0.4329	0.6437	0.8428	0.5176
35	40	0.4313	0.6381	0.8476	0.5147
55	60	0.4250	0.6395	0.8417	0.5107
65	70	0.4219	0.6453	0.8335	0.5102
45	50	0.4247	0.6381	0.8413	0.5100
60	65	0.4203	0.6402	0.8354	0.5075
85	95	0.4168	0.6397	0.8335	0.5048
70	75	0.4129	0.6405	0.8269	0.5021
75	80	0.4091	0.6383	0.8289	0.4986
80	85	0.4056	0.6423	0.8215	0.4972
85	90	0.3967	0.6332	0.8199	0.4878
90	95	0.3869	0.6323	0.8080	0.4801

Table A.2: Trapezoids parameters tuning results for Pratheepan dataset and combined rules.

Pmin	Pmax	Precision	Recall	Specificity	F-measure
10	55	0.6560	0.6955	0.9055	0.6752
10	80	0.6558	0.6950	0.9056	0.6748
10	85	0.6557	0.6949	0.9056	0.6748
10	95	0.6557	0.6950	0.9057	0.6747
10	90	0.6556	0.6950	0.9056	0.6747
10	50	0.6551	0.6953	0.9052	0.6746
10	75	0.6561	0.6935	0.9057	0.6743
5	15	0.6521	0.6978	0.9045	0.6741
10	25	0.6509	0.6991	0.9057	0.6741
10	60	0.6563	0.6928	0.9057	0.6740
10	30	0.6508	0.6983	0.9045	0.6737
10	65	0.6563	0.6920	0.9057	0.6737
10	70	0.6562	0.6920	0.9057	0.6736
10	45	0.6530	0.6955	0.9048	0.6736
10	35	0.6510	0.6972	0.9044	0.6733
10	15	0.6376	0.7133	0.8916	0.6733
10	40	0.6525	0.6945	0.9048	0.6728
5	55	0.6595	0.6852	0.9085	0.6721
10	20	0.6425	0.7039	0.8985	0.6718
5	50	0.6591	0.6850	0.9084	0.6718
5	60	0.6599	0.6827	0.9087	0.6711
5	45	0.6577	0.6848	0.9083	0.6710
15	35	0.6487	0.6939	0.9040	0.6706
5	65	0.6600	0.6813	0.9087	0.6705
5	40	0.6570	0.6842	0.9084	0.6704
5	70	0.6599	0.6811	0.9087	0.6703
5	30	0.6550	0.6861	0.9080	0.6702
5	35	0.6553	0.6858	0.9080	0.6702
5	20	0.6522	0.6891	0.9068	0.6701
5	95	0.6596	0.6809	0.9088	0.6701
5	90	0.6595	0.6810	0.9088	0.6701
5	80	0.6595	0.6806	0.9088	0.6699
5	25	0.6538	0.6868	0.9076	0.6699
5	85	0.6595	0.6805	0.9088	0.6698
15	50	0.6503	0.6904	0.9028	0.6698
15	30	0.6475	0.6935	0.9040	0.6697
20	45	0.6397	0.7024	0.8915	0.6696
15	45	0.6478	0.6924	0.9021	0.6694
20	30	0.6347	0.7077	0.8934	0.6692
15	55	0.6494	0.6900	0.9027	0.6691
15	65	0.6503	0.6879	0.9030	0.6686
20	40	0.6389	0.7012	0.8913	0.6686
15	80	0.6489	0.6893	0.9028	0.6685
5	75	0.6595	0.6776	0.9088	0.6685
15	40	0.6474	0.6909	0.9021	0.6684
15	85	0.6488	0.6891	0.9028	0.6683
20	50	0.6418	0.6971	0.8925	0.6683
15	75	0.6493	0.6884	0.9029	0.6683
15	95	0.6487	0.6891	0.9028	0.6683
15	90	0.6487	0.6891	0.9028	0.6683
15	60	0.6503	0.6873	0.9030	0.6683
20	35	0.6373	0.7022	0.8938	0.6682
20	25	0.6271	0.7144	0.8855	0.6679

Continued on next page

Table A.2 – continued from previous page

Pmin	Pmax	Precision	Recall	Specificity	F-measure
15	70	0.6494	0.6872	0.9029	0.6678
20	55	0.6409	0.6967	0.8923	0.6676
20	65	0.6420	0.6944	0.8927	0.6672
15	25	0.6420	0.6943	0.8992	0.6672
20	60	0.6419	0.6937	0.8926	0.6668
20	75	0.6411	0.6938	0.8927	0.6664
20	70	0.6412	0.6933	0.8927	0.6662
35	40	0.6196	0.7195	0.8793	0.6658
35	45	0.6208	0.7155	0.8746	0.6648
35	50	0.6246	0.7077	0.8776	0.6635
35	55	0.6242	0.7078	0.8774	0.6634
20	80	0.6349	0.6941	0.8874	0.6632
30	50	0.6295	0.7004	0.8832	0.6631
20	90	0.6348	0.6939	0.8875	0.6630
20	95	0.6348	0.6938	0.8875	0.6630
20	85	0.6348	0.6938	0.8875	0.6630
30	55	0.6293	0.7003	0.8828	0.6629
30	45	0.6256	0.7045	0.8815	0.6627
5	5	0.5587	0.8129	0.8327	0.6623
10	10	0.5587	0.8129	0.8327	0.6623
15	15	0.5587	0.8129	0.8327	0.6623
20	20	0.5587	0.8129	0.8327	0.6623
25	25	0.5587	0.8129	0.8327	0.6623
30	30	0.5587	0.8129	0.8327	0.6623
35	35	0.5587	0.8129	0.8327	0.6623
40	40	0.5587	0.8129	0.8327	0.6623
45	45	0.5587	0.8129	0.8327	0.6623
50	50	0.5587	0.8129	0.8327	0.6623
55	55	0.5587	0.8129	0.8327	0.6623
60	60	0.5587	0.8129	0.8327	0.6623
65	65	0.5587	0.8129	0.8327	0.6623
70	70	0.5587	0.8129	0.8327	0.6623
75	75	0.5587	0.8129	0.8327	0.6623
80	80	0.5587	0.8129	0.8327	0.6623
85	85	0.5587	0.8129	0.8327	0.6623
90	90	0.5587	0.8129	0.8327	0.6623
95	95	0.5587	0.8129	0.8327	0.6623
25	45	0.6254	0.7029	0.8815	0.6619
25	55	0.6290	0.6979	0.8833	0.6617
25	50	0.6286	0.6977	0.8831	0.6614
35	65	0.6247	0.7026	0.8780	0.6614
30	65	0.6295	0.6965	0.8832	0.6613
30	60	0.6295	0.6966	0.8836	0.6613
35	60	0.6244	0.7029	0.8780	0.6613
40	45	0.6094	0.7224	0.8662	0.6611
25	65	0.6298	0.6947	0.8840	0.6607
25	60	0.6296	0.6944	0.8840	0.6604
35	85	0.6252	0.6994	0.8808	0.6602
35	95	0.6251	0.6995	0.8807	0.6602
35	90	0.6251	0.6995	0.8808	0.6602
25	75	0.6291	0.6940	0.8842	0.6600
25	70	0.6291	0.6938	0.8841	0.6599
30	40	0.6219	0.7027	0.8804	0.6598
25	80	0.6284	0.6942	0.8837	0.6597
25	90	0.6284	0.6942	0.8836	0.6597

Continued on next page

Table A.2 – continued from previous page

Pmin	Pmax	Precision	Recall	Specificity	F-measure
25	95	0.6284	0.6942	0.8836	0.6597
35	70	0.6244	0.6991	0.8802	0.6596
25	85	0.6284	0.6941	0.8837	0.6596
35	75	0.6243	0.6987	0.8802	0.6594
30	70	0.6277	0.6939	0.8832	0.6592
30	75	0.6277	0.6939	0.8832	0.6592
25	40	0.6222	0.7006	0.8803	0.6591
65	90	0.6073	0.7206	0.8680	0.6591
65	95	0.6071	0.7206	0.8680	0.6590
35	80	0.6235	0.6987	0.8802	0.6590
30	80	0.6272	0.6938	0.8832	0.6589
30	95	0.6271	0.6937	0.8831	0.6587
30	85	0.6272	0.6936	0.8832	0.6587
30	90	0.6271	0.6937	0.8832	0.6587
65	85	0.6055	0.7215	0.8676	0.6584
45	65	0.6151	0.7061	0.8718	0.6575
5	10	0.6257	0.6907	0.8921	0.6566
40	50	0.6117	0.7087	0.8709	0.6566
40	65	0.6167	0.7011	0.8739	0.6562
40	55	0.6126	0.7063	0.8714	0.6561
60	90	0.6097	0.7095	0.8699	0.6558
60	70	0.6074	0.7125	0.8707	0.6558
25	35	0.6163	0.7004	0.8792	0.6557
50	65	0.6117	0.7064	0.8712	0.6556
60	95	0.6093	0.7094	0.8697	0.6556
45	95	0.6153	0.7012	0.8750	0.6554
65	80	0.6017	0.7197	0.8661	0.6554
45	90	0.6153	0.7012	0.8750	0.6554
40	60	0.6154	0.7009	0.8742	0.6554
60	85	0.6079	0.7104	0.8697	0.6552
45	85	0.6151	0.7007	0.8750	0.6551
40	95	0.6163	0.6991	0.8762	0.6551
40	90	0.6163	0.6991	0.8762	0.6551
40	85	0.6163	0.6989	0.8763	0.6550
70	95	0.6004	0.7204	0.8650	0.6549
45	70	0.6149	0.7005	0.8749	0.6549
70	90	0.6001	0.7202	0.8647	0.6547
40	70	0.6163	0.6981	0.8762	0.6546
50	95	0.6124	0.7031	0.8740	0.6546
50	90	0.6124	0.7030	0.8740	0.6546
40	75	0.6161	0.6979	0.8760	0.6545
70	85	0.5984	0.7218	0.8644	0.6544
45	75	0.6145	0.6996	0.8748	0.6543
50	85	0.6121	0.7025	0.8740	0.6542
45	80	0.6138	0.6998	0.8745	0.6540
55	90	0.6100	0.7049	0.8722	0.6540
55	95	0.6098	0.7051	0.8719	0.6540
40	80	0.6148	0.6978	0.8758	0.6537
60	80	0.6053	0.7099	0.8688	0.6534
50	70	0.6111	0.7020	0.8736	0.6534
50	75	0.6113	0.7015	0.8738	0.6533
55	85	0.6083	0.7053	0.8721	0.6532
50	80	0.6108	0.7016	0.8735	0.6530
15	20	0.6174	0.6924	0.8838	0.6528
60	75	0.6059	0.7072	0.8686	0.6526

Continued on next page

Table A.2 – continued from previous page

Pmin	Pmax	Precision	Recall	Specificity	F-measure
55	75	0.6073	0.7027	0.8723	0.6515
55	80	0.6060	0.7038	0.8716	0.6512
55	70	0.6055	0.7041	0.8713	0.6511
65	75	0.5980	0.7143	0.8654	0.6510
45	60	0.6065	0.6967	0.8723	0.6485
45	55	0.6016	0.7009	0.8689	0.6475
30	35	0.6015	0.6991	0.8741	0.6466
80	85	0.5835	0.7235	0.8555	0.6460
50	60	0.6020	0.6970	0.8703	0.6460
50	55	0.5952	0.7048	0.8663	0.6454
80	95	0.5871	0.7165	0.8638	0.6454
75	85	0.5851	0.7176	0.8640	0.6446
70	80	0.5880	0.7131	0.8648	0.6445
80	90	0.5862	0.7154	0.8632	0.6444
75	95	0.5859	0.7144	0.8638	0.6438
75	90	0.5859	0.7130	0.8635	0.6432
25	30	0.5978	0.6921	0.8787	0.6415
60	65	0.5838	0.6978	0.8689	0.6357
70	75	0.5776	0.7018	0.8708	0.6337
65	70	0.5761	0.7027	0.8670	0.6332
45	50	0.5821	0.6933	0.8669	0.6328
55	65	0.5842	0.6869	0.8692	0.6314
85	95	0.5708	0.7028	0.8732	0.6299
85	90	0.5645	0.6994	0.8702	0.6248
55	60	0.5703	0.6837	0.8660	0.6219
75	80	0.5554	0.7039	0.8527	0.6209
90	95	0.5536	0.7045	0.8603	0.6200

Table A.3: Trapezoids parameters tuning results for HGR dataset and combined rules.

Pmin	Pmax	Precision	Recall	Specificity	F-measure
5	5	0.8693	0.8641	0.9064	0.8667
10	10	0.8693	0.8641	0.9064	0.8667
15	15	0.8693	0.8641	0.9064	0.8667
20	20	0.8693	0.8641	0.9064	0.8667
25	25	0.8693	0.8641	0.9064	0.8667
30	30	0.8693	0.8641	0.9064	0.8667
35	35	0.8693	0.8641	0.9064	0.8667
40	40	0.8693	0.8641	0.9064	0.8667
45	45	0.8693	0.8641	0.9064	0.8667
50	50	0.8693	0.8641	0.9064	0.8667
55	55	0.8693	0.8641	0.9064	0.8667
60	60	0.8693	0.8641	0.9064	0.8667
65	65	0.8693	0.8641	0.9064	0.8667
70	70	0.8693	0.8641	0.9064	0.8667
75	75	0.8693	0.8641	0.9064	0.8667
80	80	0.8693	0.8641	0.9064	0.8667
85	85	0.8693	0.8641	0.9064	0.8667
90	90	0.8693	0.8641	0.9064	0.8667
95	95	0.8693	0.8641	0.9064	0.8667
25	40	0.8858	0.7323	0.9277	0.8018
25	45	0.8867	0.7314	0.9288	0.8016

Continued on next page

Table A.3 – continued from previous page

Pmin	Pmax	Precision	Recall	Specificity	F-measure
25	35	0.8836	0.7334	0.9253	0.8015
25	50	0.8869	0.7311	0.9291	0.8015
30	50	0.8862	0.7316	0.9284	0.8015
20	40	0.8881	0.7301	0.9298	0.8014
50	75	0.8821	0.7342	0.9246	0.8014
60	80	0.8782	0.7369	0.9211	0.8014
65	85	0.8757	0.7387	0.9185	0.8014
50	80	0.8821	0.7342	0.9246	0.8014
25	55	0.8870	0.7308	0.9294	0.8014
25	65	0.8870	0.7308	0.9293	0.8013
50	90	0.8823	0.7339	0.9248	0.8013
30	45	0.8842	0.7326	0.9263	0.8013
50	85	0.8823	0.7339	0.9248	0.8013
50	70	0.8791	0.7361	0.9208	0.8013
25	60	0.8870	0.7307	0.9293	0.8013
60	85	0.8785	0.7365	0.9213	0.8013
20	45	0.8881	0.7299	0.9298	0.8013
65	90	0.8759	0.7384	0.9186	0.8013
60	90	0.8786	0.7364	0.9214	0.8013
50	95	0.8823	0.7339	0.9248	0.8012
55	80	0.8802	0.7353	0.9230	0.8012
35	50	0.8824	0.7337	0.9243	0.8012
25	70	0.8868	0.7307	0.9292	0.8012
30	55	0.8862	0.7311	0.9287	0.8012
65	95	0.8759	0.7382	0.9187	0.8012
20	35	0.8877	0.7300	0.9296	0.8012
25	85	0.8869	0.7306	0.9293	0.8012
25	80	0.8869	0.7306	0.9293	0.8012
25	95	0.8869	0.7306	0.9293	0.8012
25	90	0.8869	0.7305	0.9293	0.8012
25	75	0.8868	0.7305	0.9292	0.8011
60	95	0.8786	0.7362	0.9215	0.8011
55	85	0.8804	0.7350	0.9232	0.8011
40	65	0.8840	0.7324	0.9269	0.8011
55	90	0.8804	0.7349	0.9232	0.8011
30	60	0.8861	0.7309	0.9286	0.8011
40	80	0.8842	0.7322	0.9271	0.8011
20	50	0.8881	0.7296	0.9298	0.8011
50	65	0.8770	0.7372	0.9185	0.8011
30	65	0.8861	0.7309	0.9285	0.8010
40	95	0.8843	0.7321	0.9271	0.8010
35	65	0.8851	0.7315	0.9279	0.8010
40	90	0.8843	0.7321	0.9271	0.8010
35	55	0.8848	0.7317	0.9276	0.8010
40	85	0.8842	0.7321	0.9271	0.8010
35	80	0.8853	0.7314	0.9281	0.8010
55	95	0.8803	0.7348	0.9232	0.8010
20	55	0.8882	0.7293	0.9303	0.8010
20	65	0.8882	0.7294	0.9302	0.8010
40	70	0.8840	0.7322	0.9267	0.8010
20	70	0.8882	0.7293	0.9302	0.8009
40	75	0.8841	0.7321	0.9270	0.8009
35	90	0.8853	0.7312	0.9282	0.8009
35	95	0.8853	0.7312	0.9282	0.8009
35	85	0.8853	0.7312	0.9281	0.8009

Continued on next page

Table A.3 – continued from previous page

Pmin	Pmax	Precision	Recall	Specificity	F-measure
20	60	0.8882	0.7293	0.9301	0.8009
35	75	0.8852	0.7313	0.9280	0.8009
35	70	0.8851	0.7314	0.9278	0.8009
55	75	0.8788	0.7357	0.9212	0.8009
20	80	0.8882	0.7292	0.9302	0.8009
35	45	0.8767	0.7372	0.9176	0.8009
35	60	0.8848	0.7315	0.9276	0.8009
20	75	0.8882	0.7292	0.9302	0.8009
30	80	0.8860	0.7307	0.9285	0.8009
30	70	0.8859	0.7308	0.9284	0.8009
20	95	0.8882	0.7292	0.9303	0.8009
20	85	0.8882	0.7292	0.9303	0.8009
20	90	0.8882	0.7292	0.9303	0.8009
30	75	0.8860	0.7307	0.9284	0.8009
40	55	0.8815	0.7337	0.9241	0.8008
30	85	0.8860	0.7306	0.9285	0.8008
30	90	0.8860	0.7306	0.9285	0.8008
45	65	0.8822	0.7332	0.9250	0.8008
30	95	0.8860	0.7306	0.9285	0.8008
45	80	0.8829	0.7327	0.9257	0.8008
40	60	0.8831	0.7325	0.9260	0.8008
45	75	0.8829	0.7327	0.9257	0.8008
45	85	0.8830	0.7325	0.9259	0.8008
45	70	0.8823	0.7331	0.9249	0.8008
45	90	0.8831	0.7325	0.9259	0.8007
30	40	0.8776	0.7362	0.9184	0.8007
45	95	0.8830	0.7324	0.9258	0.8007
65	80	0.8701	0.7415	0.9117	0.8007
60	75	0.8737	0.7388	0.9161	0.8006
20	30	0.8861	0.7301	0.9284	0.8005
55	70	0.8737	0.7385	0.9150	0.8005
45	60	0.8800	0.7339	0.9227	0.8003
15	25	0.8880	0.7282	0.9297	0.8002
15	20	0.8795	0.7340	0.9192	0.8002
70	85	0.8700	0.7406	0.9122	0.8001
15	40	0.8895	0.7269	0.9314	0.8000
5	10	0.8961	0.7225	0.9360	0.8000
20	25	0.8722	0.7389	0.9105	0.8000
70	90	0.8703	0.7401	0.9125	0.7999
15	30	0.8887	0.7273	0.9304	0.7999
15	35	0.8893	0.7269	0.9312	0.7999
5	15	0.8970	0.7218	0.9366	0.7999
5	20	0.8971	0.7217	0.9367	0.7999
10	20	0.8917	0.7252	0.9332	0.7999
5	40	0.8971	0.7217	0.9366	0.7999
50	60	0.8677	0.7419	0.9070	0.7999
15	45	0.8896	0.7266	0.9315	0.7999
5	25	0.8970	0.7217	0.9366	0.7999
5	45	0.8971	0.7216	0.9366	0.7999
5	55	0.8971	0.7216	0.9366	0.7998
5	50	0.8971	0.7216	0.9366	0.7998
5	60	0.8971	0.7216	0.9366	0.7998
5	30	0.8970	0.7216	0.9366	0.7998
40	50	0.8750	0.7366	0.9170	0.7998
5	90	0.8970	0.7216	0.9367	0.7998

Continued on next page

Table A.3 – continued from previous page

Pmin	Pmax	Precision	Recall	Specificity	F-measure
5	95	0.8970	0.7216	0.9367	0.7998
5	80	0.8970	0.7216	0.9366	0.7998
5	85	0.8970	0.7216	0.9367	0.7998
5	75	0.8970	0.7216	0.9366	0.7998
5	70	0.8970	0.7216	0.9366	0.7998
70	95	0.8706	0.7397	0.9126	0.7998
5	65	0.8970	0.7216	0.9366	0.7998
5	35	0.8970	0.7215	0.9366	0.7998
15	50	0.8895	0.7265	0.9315	0.7998
10	30	0.8921	0.7247	0.9334	0.7997
10	25	0.8918	0.7249	0.9333	0.7997
15	55	0.8894	0.7264	0.9315	0.7997
10	45	0.8922	0.7245	0.9334	0.7996
10	40	0.8922	0.7245	0.9334	0.7996
10	35	0.8922	0.7245	0.9335	0.7996
10	95	0.8922	0.7245	0.9335	0.7996
10	90	0.8922	0.7245	0.9335	0.7996
10	80	0.8922	0.7245	0.9335	0.7996
10	85	0.8922	0.7245	0.9335	0.7996
15	90	0.8894	0.7263	0.9315	0.7996
10	75	0.8922	0.7245	0.9335	0.7996
10	70	0.8922	0.7245	0.9335	0.7996
15	95	0.8894	0.7263	0.9315	0.7996
15	85	0.8894	0.7263	0.9315	0.7996
15	65	0.8894	0.7263	0.9314	0.7996
15	60	0.8894	0.7263	0.9314	0.7996
15	80	0.8894	0.7263	0.9315	0.7996
15	70	0.8894	0.7263	0.9315	0.7996
10	65	0.8921	0.7245	0.9334	0.7996
15	75	0.8894	0.7263	0.9315	0.7996
10	60	0.8921	0.7245	0.9334	0.7996
10	55	0.8921	0.7245	0.9334	0.7996
10	50	0.8922	0.7244	0.9334	0.7996
10	15	0.8872	0.7276	0.9275	0.7995
75	90	0.8609	0.7460	0.9016	0.7993
75	85	0.8557	0.7496	0.8946	0.7992
75	95	0.8610	0.7452	0.9017	0.7989
55	65	0.8644	0.7426	0.9039	0.7989
60	70	0.8627	0.7429	0.9039	0.7983
45	55	0.8725	0.7356	0.9156	0.7982
25	30	0.8671	0.7393	0.9055	0.7981
30	35	0.8607	0.7426	0.8998	0.7973
65	75	0.8579	0.7432	0.9004	0.7965
35	40	0.8547	0.7456	0.8918	0.7964
70	80	0.8566	0.7441	0.8980	0.7964
40	45	0.8526	0.7448	0.8922	0.7950
55	60	0.8392	0.7530	0.8756	0.7938
45	50	0.8501	0.7437	0.8892	0.7934
80	90	0.8423	0.7483	0.8849	0.7925
80	95	0.8437	0.7471	0.8864	0.7925
50	55	0.8435	0.7454	0.8838	0.7914
60	65	0.8393	0.7484	0.8793	0.7913
65	70	0.8328	0.7482	0.8739	0.7882
75	80	0.8278	0.7501	0.8688	0.7870
85	95	0.8198	0.7556	0.8570	0.7864

Continued on next page

Table A.3 – continued from previous page

Pmin	Pmax	Precision	Recall	Specificity	F-measure
80	85	0.8228	0.7524	0.8639	0.7861
70	75	0.8259	0.7495	0.8660	0.7859
90	95	0.7998	0.7664	0.8337	0.7827
85	90	0.8071	0.7515	0.8493	0.7783

Table A.4: Trapezoids parameters tuning results for SFA dataset and combined rules.

Pmin	Pmax	Precision	Recall	Specificity	F-measure
5	5	0.9313	0.6617	0.9785	0.7737
10	10	0.9313	0.6617	0.9785	0.7737
15	15	0.9313	0.6617	0.9785	0.7737
20	20	0.9313	0.6617	0.9785	0.7737
25	25	0.9313	0.6617	0.9785	0.7737
30	30	0.9313	0.6617	0.9785	0.7737
35	35	0.9313	0.6617	0.9785	0.7737
40	40	0.9313	0.6617	0.9785	0.7737
45	45	0.9313	0.6617	0.9785	0.7737
50	50	0.9313	0.6617	0.9785	0.7737
55	55	0.9313	0.6617	0.9785	0.7737
60	60	0.9313	0.6617	0.9785	0.7737
65	65	0.9313	0.6617	0.9785	0.7737
70	70	0.9313	0.6617	0.9785	0.7737
75	75	0.9313	0.6617	0.9785	0.7737
80	80	0.9313	0.6617	0.9785	0.7737
85	85	0.9313	0.6617	0.9785	0.7737
90	90	0.9313	0.6617	0.9785	0.7737
95	95	0.9313	0.6617	0.9785	0.7737
85	90	0.8307	0.4534	0.9519	0.5866
70	75	0.8554	0.4442	0.9651	0.5848
80	90	0.8721	0.4385	0.9733	0.5835
50	55	0.8721	0.4383	0.9718	0.5834
85	95	0.8610	0.4411	0.9685	0.5833
80	95	0.8743	0.4376	0.9742	0.5833
60	65	0.8631	0.4403	0.9682	0.5831
75	90	0.8795	0.4358	0.9779	0.5828
70	90	0.8870	0.4337	0.9801	0.5825
75	95	0.8803	0.4352	0.9780	0.5825
70	85	0.8849	0.4340	0.9797	0.5823
70	95	0.8874	0.4332	0.9801	0.5822
70	80	0.8796	0.4349	0.9784	0.5820
60	70	0.8860	0.4333	0.9809	0.5819
65	80	0.8877	0.4326	0.9805	0.5817
55	60	0.8657	0.4380	0.9725	0.5816
65	70	0.8512	0.4416	0.9664	0.5815
60	75	0.8914	0.4315	0.9823	0.5815
65	75	0.8832	0.4334	0.9796	0.5814
60	80	0.8938	0.4308	0.9826	0.5814
75	80	0.8375	0.4452	0.9599	0.5814
75	85	0.8739	0.4355	0.9768	0.5813
45	55	0.8956	0.4302	0.9824	0.5812
55	65	0.8872	0.4320	0.9811	0.5810
50	60	0.8888	0.4315	0.9806	0.5810

Continued on next page

Table A.4 – continued from previous page

Pmin	Pmax	Precision	Recall	Specificity	F-measure
55	70	0.8907	0.4308	0.9817	0.5808
45	60	0.8991	0.4289	0.9834	0.5807
55	80	0.8968	0.4294	0.9830	0.5807
65	90	0.8913	0.4306	0.9817	0.5807
55	75	0.8945	0.4298	0.9828	0.5806
65	85	0.8902	0.4307	0.9816	0.5806
65	95	0.8913	0.4304	0.9818	0.5805
35	40	0.8897	0.4308	0.9797	0.5805
60	90	0.8952	0.4293	0.9828	0.5803
60	85	0.8949	0.4294	0.9827	0.5803
60	95	0.8951	0.4292	0.9828	0.5802
55	90	0.8982	0.4284	0.9833	0.5801
45	65	0.9000	0.4279	0.9836	0.5800
55	85	0.8977	0.4284	0.9832	0.5800
50	80	0.8997	0.4279	0.9837	0.5799
40	45	0.8885	0.4304	0.9802	0.5799
55	95	0.8982	0.4282	0.9833	0.5799
30	35	0.8984	0.4281	0.9821	0.5799
45	75	0.9035	0.4270	0.9844	0.5799
50	75	0.8985	0.4280	0.9836	0.5799
40	55	0.9000	0.4277	0.9837	0.5798
45	70	0.9011	0.4274	0.9838	0.5798
45	80	0.9039	0.4268	0.9845	0.5798
35	45	0.9005	0.4275	0.9836	0.5798
50	70	0.8953	0.4286	0.9827	0.5797
45	50	0.8804	0.4321	0.9784	0.5797
40	50	0.8982	0.4279	0.9835	0.5796
50	65	0.8919	0.4291	0.9822	0.5795
35	50	0.9039	0.4263	0.9844	0.5794
40	60	0.9017	0.4267	0.9841	0.5793
45	90	0.9046	0.4259	0.9846	0.5792
50	90	0.9006	0.4268	0.9839	0.5791
45	85	0.9045	0.4259	0.9846	0.5791
50	85	0.9002	0.4268	0.9838	0.5791
45	95	0.9046	0.4258	0.9846	0.5790
50	95	0.9006	0.4267	0.9839	0.5790
30	40	0.9054	0.4255	0.9842	0.5790
40	65	0.9029	0.4260	0.9843	0.5789
35	55	0.9050	0.4255	0.9846	0.5789
40	70	0.9038	0.4256	0.9845	0.5787
40	75	0.9051	0.4254	0.9848	0.5787
25	35	0.9103	0.4242	0.9855	0.5787
25	30	0.9049	0.4253	0.9844	0.5786
40	80	0.9053	0.4252	0.9849	0.5786
35	60	0.9065	0.4249	0.9849	0.5786
30	45	0.9069	0.4247	0.9848	0.5785
30	50	0.9078	0.4243	0.9852	0.5783
35	65	0.9072	0.4243	0.9850	0.5781
40	90	0.9061	0.4244	0.9851	0.5781
25	40	0.9113	0.4233	0.9857	0.5781
40	85	0.9057	0.4244	0.9850	0.5780
30	55	0.9086	0.4238	0.9855	0.5780
35	75	0.9083	0.4238	0.9853	0.5780
35	70	0.9077	0.4239	0.9851	0.5779
40	95	0.9061	0.4243	0.9851	0.5779

Continued on next page

Table A.4 – continued from previous page

Pmin	Pmax	Precision	Recall	Specificity	F-measure
35	80	0.9084	0.4237	0.9853	0.5779
30	60	0.9098	0.4234	0.9857	0.5778
30	65	0.9101	0.4230	0.9858	0.5776
35	90	0.9093	0.4231	0.9855	0.5775
30	70	0.9101	0.4229	0.9859	0.5774
30	75	0.9106	0.4227	0.9860	0.5774
35	85	0.9089	0.4231	0.9854	0.5774
35	95	0.9093	0.4229	0.9855	0.5773
25	45	0.9119	0.4223	0.9860	0.5773
30	80	0.9106	0.4226	0.9860	0.5773
25	50	0.9124	0.4220	0.9861	0.5771
20	25	0.9111	0.4220	0.9854	0.5768
30	90	0.9109	0.4219	0.9861	0.5767
20	30	0.9156	0.4209	0.9865	0.5767
25	55	0.9132	0.4214	0.9865	0.5767
30	85	0.9107	0.4219	0.9860	0.5767
30	95	0.9109	0.4218	0.9861	0.5766
25	60	0.9138	0.4211	0.9866	0.5765
25	65	0.9140	0.4207	0.9866	0.5762
25	70	0.9139	0.4205	0.9867	0.5760
25	75	0.9144	0.4204	0.9867	0.5760
25	80	0.9144	0.4203	0.9867	0.5759
20	35	0.9169	0.4194	0.9869	0.5755
25	90	0.9147	0.4198	0.9868	0.5754
25	95	0.9147	0.4197	0.9868	0.5754
80	85	0.8375	0.4382	0.9608	0.5753
25	85	0.9144	0.4197	0.9868	0.5753
20	40	0.9172	0.4190	0.9870	0.5752
20	45	0.9170	0.4184	0.9870	0.5746
20	50	0.9170	0.4182	0.9871	0.5745
20	55	0.9173	0.4178	0.9872	0.5741
20	60	0.9175	0.4175	0.9872	0.5739
20	65	0.9178	0.4172	0.9873	0.5737
20	70	0.9178	0.4170	0.9874	0.5735
20	75	0.9179	0.4169	0.9874	0.5734
20	80	0.9179	0.4168	0.9874	0.5733
20	90	0.9179	0.4164	0.9874	0.5729
20	85	0.9179	0.4163	0.9874	0.5728
20	95	0.9179	0.4163	0.9874	0.5728
15	20	0.9162	0.4157	0.9859	0.5719
15	25	0.9186	0.4146	0.9867	0.5713
15	30	0.9206	0.4140	0.9872	0.5711
15	35	0.9213	0.4131	0.9876	0.5704
15	40	0.9213	0.4130	0.9876	0.5703
15	45	0.9211	0.4125	0.9876	0.5698
15	50	0.9211	0.4124	0.9877	0.5697
15	55	0.9212	0.4120	0.9878	0.5693
15	60	0.9211	0.4117	0.9878	0.5690
15	65	0.9214	0.4114	0.9879	0.5688
15	75	0.9217	0.4111	0.9880	0.5686
15	70	0.9213	0.4112	0.9879	0.5686
15	80	0.9217	0.4111	0.9880	0.5686
15	90	0.9217	0.4107	0.9880	0.5682
15	85	0.9218	0.4106	0.9880	0.5682
15	95	0.9217	0.4106	0.9880	0.5681

Continued on next page

Table A.4 – continued from previous page

Pmin	Pmax	Precision	Recall	Specificity	F-measure
10	15	0.9197	0.4092	0.9870	0.5664
10	20	0.9218	0.4071	0.9873	0.5648
10	25	0.9223	0.4066	0.9875	0.5644
10	30	0.9236	0.4060	0.9879	0.5641
10	35	0.9242	0.4052	0.9882	0.5634
10	40	0.9243	0.4052	0.9883	0.5634
10	45	0.9241	0.4049	0.9883	0.5631
10	50	0.9240	0.4048	0.9883	0.5630
90	95	0.8103	0.4311	0.9542	0.5628
10	55	0.9240	0.4045	0.9884	0.5627
10	60	0.9239	0.4042	0.9884	0.5624
10	65	0.9242	0.4039	0.9885	0.5621
10	70	0.9243	0.4038	0.9885	0.5621
10	75	0.9243	0.4037	0.9885	0.5620
10	80	0.9243	0.4037	0.9886	0.5619
10	85	0.9248	0.4032	0.9886	0.5615
10	90	0.9247	0.4031	0.9886	0.5615
10	95	0.9246	0.4030	0.9886	0.5614
5	10	0.9241	0.4006	0.9873	0.5589
5	15	0.9260	0.3982	0.9878	0.5569
5	20	0.9269	0.3972	0.9881	0.5561
5	25	0.9267	0.3968	0.9882	0.5557
5	50	0.9282	0.3961	0.9889	0.5553
5	30	0.9269	0.3963	0.9884	0.5553
5	60	0.9284	0.3960	0.9890	0.5552
5	90	0.9284	0.3960	0.9890	0.5552
5	55	0.9284	0.3960	0.9890	0.5552
5	40	0.9275	0.3962	0.9887	0.5552
5	85	0.9284	0.3960	0.9890	0.5552
5	45	0.9280	0.3961	0.9889	0.5552
5	95	0.9284	0.3960	0.9890	0.5552
5	65	0.9283	0.3960	0.9890	0.5551
5	70	0.9284	0.3959	0.9890	0.5551
5	80	0.9283	0.3959	0.9890	0.5551
5	75	0.9284	0.3959	0.9890	0.5551
5	35	0.9274	0.3960	0.9887	0.5550

Bibliography

- Albiol *et al.*(2001)** Alberto Albiol, Luis Torres and Edward J. Delp. Optimum color spaces for skin detection. In *International Conference on Image Processing*, pages 122–124. 10
- Anderson and Parrish(1981)** R. Rox Anderson and John A. Parrish. The optics of human skin. *Journal of investigative dermatology*, 77(1):13–19. 1
- Basilio *et al.*(2011)** Jorge Alberto Marcial Basilio, Gualberto Aguilar Torres, Gabriel Sánchez Pérez, L. Karina Toscano Medina and Hector M. Perez Meana. Explicit image detection using YCbCr space color model as skin detection. *Applications of Mathematics and Computer Engineering*, pages 123–128. 9, 19
- Ben(2009)** R. G. Ben. CIE 1931 xy color space diagram. https://en.wikipedia.org/wiki/File:CIE1931xy_blank.svg, 2009. Last access 12/10/2016. 23
- Bergasa *et al.*(2000)** Luis Miguel Bergasa, Manuel Mazo, Alfredo Gardel, Miguel A. Sotelo and Luciano Boquete. Unsupervised and adaptive gaussian skin-color model. *Image and Vision Computing*, 18(12):987–1003. 10
- Bhatt and Dhall(2012)** Rajen B. Bhatt and Abhinav Dhall. Skin segmentation dataset. <https://archive.ics.uci.edu/ml/datasets/Skin+Segmentation>, 2012. Last access 05/06/2016. 41
- Brancati *et al.*(2017)** Nadia Brancati, Giuseppe De Pietro, Maria Frucci and Luigi Gallo. Human skin detection through correlation rules between the YCb and YCr subspaces based on dynamic color clustering. *Computer Vision and Image Understanding*, 155: 33–42. 4, 5, 11, 31, 32, 33, 34, 39, 47, 48, 49, 50, 51, 52, 53, 55, 56, 57, 67
- Casati *et al.*(2013)** João Paulo Brognoni Casati, Diego Rafael Moraes and Evandro Luis Linhari Rodrigues. SFA: A human skin image database based on FERET and AR facial images. In *IX workshop de Visão Computacional*. 42, 43, 44
- Chai and Ngan(1999)** Douglas Chai and King N. Ngan. Face segmentation using skin-color map in videophone applications. *IEEE Transactions on Circuits and Systems for Video Technology*, 9(4):551–564. 9, 19, 32
- Chaplin(2004)** George Chaplin. Geographic distribution of environmental factors influencing human skin coloration. *American Journal of Physical Anthropology*, 125(3):292–302. 2
- Chaves-González *et al.*(2010)** Jose M. Chaves-González, Miguel A. Vega-Rodríguez, Juan A. Gómez-Pulido and Juan M. Sánchez-Pérez. Detecting skin in face recognition systems: A colour spaces study. *Digital Signal Processing*, 20(3):806–823. 10, 11, 68

- Edwards and Duntley(1939)** Edward A. Edwards and S. Quimby Duntley. The pigments and color of living human skin. *Developmental Dynamics*, 65(1):1–33. [1](#)
- Faria and Jr.(2018)** Rodrigo Augusto Dias Faria and Roberto Hirata Jr. Combined correlation rules to detect skin based on dynamic color clustering. In *Proceedings of the 13th International Joint Conference on Computer Vision, Imaging and Computer Graphics Theory and Applications - VISAPP*, volume 5, pages 309–316. INSTICC, SciTePress. ISBN 978-989-758-290-5. doi: 10.5220/0006618003090316. [5](#)
- Fisher et al.(2003)** Robert Fisher, Simon Perkins, Ashley Walker and Erik Wolfart. Intensity histogram. <http://homepages.inf.ed.ac.uk/rbf/HIPR2/histgram.htm>, 2003. Last access 13/03/2018. [17](#), [18](#)
- Fleck et al.(1996)** Margaret M. Fleck, David A. Forsyth and Chris Bregler. Finding naked people. In *European Conference on Computer Vision*, pages 593–602. Springer. [3](#)
- Gevers et al.(2012)** Theo Gevers, Arjan Gijsenij, Joost van de Weijer and Jan-Mark Geusebroek. *Color in Computer Vision: Fundamentals and Applications*. Wiley. [20](#), [24](#)
- Gonzalez and Woods(2002)** Rafael C. Gonzalez and Richard E. Woods. *Digital Image Processing*. Prentice Hall, 2nd edition. [3](#), [13](#), [14](#), [15](#), [17](#), [18](#), [19](#), [20](#), [21](#), [24](#), [25](#)
- Grzejszczak et al.(2016)** Tomasz Grzejszczak, Michal Kawulok and Adam Galuszka. Hand landmarks detection and localization in color images. *Multimedia Tools and Applications*, 75(23):16363–16387. ISSN 1573-7721. doi: 10.1007/s11042-015-2934-5. [45](#), [46](#)
- Hsu et al.(2002)** Rein-Lien Hsu, M. Abdel-Mottaleb and A. K. Jain. Face detection in color images. *IEEE Transactions on Pattern Analysis and Machine Intelligence*, 24(5):696–706. ISSN 0162-8828. doi: 10.1109/34.1000242. [8](#), [9](#)
- Ice(2016)** Black Ice. The HSI color space. <http://www.blackice.com/images/HSIColorModel.jpg>, 2016. Last access 15/10/2016. [27](#)
- Jablonski(2004)** Nina G. Jablonski. The evolution of human skin and skin color. *Annual Review of Anthropology*, 33:585–623. [2](#)
- Jablonski and Chaplin(2000)** Nina G. Jablonski and George Chaplin. The evolution of human skin coloration. *Journal of Human Evolution*, 39(1):57–106. [2](#)
- Jablonski and Chaplin(2010)** Nina G. Jablonski and George Chaplin. Human skin pigmentation as an adaptation to UV radiation. *Proceedings of the National Academy of Sciences*, 107(Supplement 2):8962–8968. [2](#)
- Jayaram et al.(2004)** Sriram Jayaram, Stephen Schmugge, Min C. Shin and Leonid V. Tsap. Effect of colorspace transformation, the illuminance component, and color modeling on skin detection. In *Proceedings of the 2004 IEEE Computer Society Conference on Computer Vision and Pattern Recognition*, volume 2, pages 813–818. IEEE. [10](#)
- Jones and Rehg(2002)** Michael J. Jones and James M. Rehg. Statistical color models with application to skin detection. *International Journal of Computer Vision*, 46(1):81–96. [7](#), [8](#), [46](#), [47](#)
- Kakumanu et al.(2007)** Praveen Kakumanu, Sokratis Makrogiannis and Nikolaos Bourbakis. A survey of skin-color modeling and detection methods. *Pattern Recognition*, 40(3):1106–1122. [2](#), [4](#), [7](#), [10](#), [26](#)

- Kaur and Kranthi(2012)** Amanpreet Kaur and B. V. Kranthi. Comparison between YCbCr color space and CIELab color space for skin color segmentation. *International Journal of Applied Information Systems*, 3(4):30–33. [11](#), [19](#)
- Kawulok et al.(2013)** Michal Kawulok, Jolanta Kawulok, Jakub Nalepa and Maciej Papiez. Skin detection using spatial analysis with adaptive seed. In *2013 IEEE International Conference on Image Processing*, pages 3720–3724. IEEE. [10](#)
- Kawulok et al.(2014)** Michal Kawulok, Jolanta Kawulok, Jakub Nalepa and Bogdan Smolka. Self-adaptive algorithm for segmenting skin regions. *EURASIP Journal on Advances in Signal Processing*, 2014(170):1–22. ISSN 1687-6180. doi: 10.1186/1687-6180-2014-170. [45](#), [46](#)
- Khan et al.(2012)** Rehanullah Khan, Allan Hanbury, Julian Stöttinger and Abdul Bais. Color based skin classification. *Pattern Recognition Letters*, 33(2):157–163. [11](#)
- Kovac et al.(2003)** Jure Kovac, Peter Peer and Franc Solina. *Human skin color clustering for face detection*, volume 2. IEEE. [8](#), [9](#), [11](#), [19](#)
- Kumar and Malhotra(2015)** Amit Kumar and Shivani Malhotra. Performance analysis of color space for optimum skin color detection. In *2015 Fifth International Conference on Communication Systems and Network Technologies*, pages 554–558. IEEE. [11](#), [19](#)
- Lichman(2013)** M. Lichman. UCI machine learning repository. <http://archive.ics.uci.edu/ml>, 2013. Last access 07/06/2016. [41](#)
- Mahmoodi and Sayedi(2016)** Mohammad Reza Mahmoodi and Sayed Masoud Sayedi. A comprehensive survey on human skin detection. *International Journal of Image, Graphics and Signal Processing*, 8(5):1–35. [7](#), [10](#), [46](#)
- Martínez and Benavente(1998)** Aleix Martínez and Robert Benavente. The AR face database. Technical report, Purdue University. Last access 22/03/2017. [10](#), [42](#)
- Minear and Park(2004)** Meredith Minear and Denise Park. Productive aging lab face database. <https://pal.utdallas.edu/facedb/>, 2004. Last access 22/03/2017. [41](#)
- Naji et al.(2012)** Sinan A. Naji, Roziati Zainuddin and Hamid A. Jalab. Skin segmentation based on multi pixel color clustering models. *Digital Signal Processing*, 22(6):933–940. [10](#)
- Nalepa and Kawulok(2014)** Jakub Nalepa and Michal Kawulok. Fast and accurate hand shape classification. In Stanislaw Koziełski, Dariusz Mrozek, Paweł Kasprowski, Bozena Malysiak-Mrozek and Daniel Kostrzewska, editors, *Beyond Databases, Architectures, and Structures*, volume 424 of *Communications in Computer and Information Science*, pages 364–373. Springer. ISBN 978-3-319-06931-9. doi: 10.1007/978-3-319-06932-6_35. URL http://dx.doi.org/10.1007/978-3-319-06932-6_35. Last access 18/04/2017. [45](#), [46](#)
- Pedrini and Schwartz(2008)** Hélio Pedrini and William Robson Schwartz. *Análise de imagens digitais: princípios, algoritmos e aplicações*. Thomson Learning, São Paulo. [13](#), [14](#), [15](#), [16](#), [17](#), [18](#), [26](#), [27](#), [28](#), [29](#)
- Phillips et al.(1996)** P. Jonathon Phillips, Harry Wechsler, Jeffrey Huang and Patrick J. Rauss. The facial recognition technology (FERET) database. <https://www.nist.gov/programs-projects/face-recognition-technology-feret>, 1996. Last access 23/06/2016. [41](#), [42](#)

- Plataniotis and Venetsanopoulos(2000)** Konstantinos N. Plataniotis and Anastasios N. Venetsanopoulos. *Color Image Processing and Applications*. Springer, 1st edition. 18, 19, 21, 22, 24, 25, 26
- Rus(2007)** Jacob Rus. The Munsell color system. <https://commons.wikimedia.org/wiki/File:Munsell-system.svg>, 2007. Last access 12/10/2016. 21
- Rus(2008)** Jacob Rus. The "primary" and "secondary" colors in a four-color print process. <https://en.wikipedia.org/wiki/File:SubtractiveColor.svg>, 2008. Last access 12/10/2016. 25
- Shaik et al.(2015)** Khamar Basha Shaik, Ganesan P., V. Kalist, B. S. Sathish and J. Merlin Mary Jenitha. Comparative study of skin color detection and segmentation in HSV and YCbCr color space. *Procedia Computer Science*, 57:41–48. 11, 19
- Tan et al.(2012)** Wei Ren Tan, Chee Seng Chan, Pratheepan Yogarajah and Joan Condell. A fusion approach for efficient human skin detection. *IEEE Transactions on Industrial Informatics*, 8(1):138–147. 9, 10, 18, 19, 45
- Vezhnevets et al.(2003)** Vladimir Vezhnevets, Vassili Sazonov and Alla Andreeva. A survey on pixel-based skin color detection techniques. In *Proceedings of GRAPHICON-2003*, pages 85–92. 4, 7, 8, 9, 23
- Wajnberg(2018)** Nanette Wajnberg. Skin remedies for psoriasis, eczema, dry scalp and more. <http://www.skin-remedies.com/>, 2018. Last access 18/04/2018. 1
- Yogarajah et al.(2011)** Pratheepan Yogarajah, Joan Condell, Kevin Curran, Paul McKevitt and Abbas Cheddad. A dynamic threshold approach for skin tone detection in colour images. *International Journal of Biometrics*, 4(1):38–55. 9, 19